

Proprioceptive Qualities in Manual Control

MSc Thesis Report

M. Boogaard



Proprioceptive Qualities in Manual Control

MSc Thesis Report

by

M. Boogaard

to obtain the degree of Master of Science
at the Delft University of Technology,
to be defended publicly on Thursday June 10, 2021 at 14:00.

Student number: 4548558
Project duration: September 15, 2020 – June 10, 2021
Thesis committee: Dr. ir. M. M. van Paassen, TU Delft, supervisor
Prof. dr. ir. M. Mulder, TU Delft, supervisor
Dr. ir. A. C. Schouten, TU Delft, additional committee member

An electronic version of this thesis is available at <http://repository.tudelft.nl/>.

Preface

This report presents my master thesis work in Aerospace Engineering at Delft University of Technology on a topic in manual control. It includes a scientific paper in Part I discussing the most important outcomes of two experiments I conducted accompanied by appendices in Part II with the full results. My preliminary report which was graded separately is included in Part III followed by its own appendices given in Part IV. The preliminary report discusses the performed literature survey and preliminary numerical simulations before the experimental phase of this research.

This thesis was written during a phase of global pandemic and studying from home which made the help that I received from several people with the work I present in this report all the more important. My daily supervisor, Dr. ir. M. M. (René) van Paassen, provided excellent advice and guidance. With his expertise and knowledge, René helped me to better understand and have a more critical view towards the topic at hand. He inspired me to keep improving throughout this thesis. His extensive help with configuring the experiments for this research was of enormous value in overcoming the challenges I faced in this phase. My second supervisor, Prof. dr. ir. Max Mulder, has inspired me academically since the first of his lectures that I attended. As a great teacher, Max motivates and entertains students whilst perfectly explaining the toughest topics. During my thesis he gave outstanding advice and comments on my work which allowed me to make improvements and learn from them. He also provided helpful advice on implementing the principles he teaches in my work. During the configuration of my experiments, ir. Olaf Stroosma was incredibly forthcoming in helping me to get started with programming. This, and his instant willingness to help whenever I encountered problems, was invaluable for my progress and deserves my deepest gratitude.

Previous studies conducted at the Faculty of Aerospace Engineering at Delft University of Technology by dr. ir. Wei Fu on haptic perception thresholds and of human operator models by dr. ir. Kasper van der El were very enlightening and inspiring for my research and deserve explicit acknowledgement for their thoroughness and academic value.

With this thesis I am nearing the end of my time as student at Delft University of Technology during which I had countless valuable learning experiences thanks to the excellent staff and the offered support at the Faculty of Aerospace Engineering. This makes me feel ready as an engineer to start challenging myself in new ways to better understand and improve the world we live in.

*M. Boogaard
Delft, May 2021*

Contents

List of Figures	vi
List of Tables	viii
List of Abbreviations	xi
List of Symbols	xiii
I Scientific Paper	1
II Research Appendices	19
A Individual Subjects' Tracking Task Results	21
A.1 Subject 1	22
A.2 Subject 2	23
A.3 Subject 3	24
A.4 Subject 4	25
A.5 Subject 5	26
A.6 Subject 6	27
A.7 Subject 7	28
B Derivation of HO Neuromuscular Model Dynamics	29
C Tracking Task Metrics Correlation Analysis	31
C.1 Coherence and Tracking Error	31
C.2 GTO Activity and Tracking Error	32
D Experiment Briefing & Consent Form	33
III Preliminary Research Report	37
<i>As graded separately (08-03-2021) for AE4020 Literature Study</i>	
1 Introduction	41
2 Force- vs. Position Measurement	43
3 Muscle Sensory Afferent Activation	45
4 Pilot Model	49
4.1 Pilot Model Signals	51
4.2 Pilot Inaccuracies	52
4.3 Stick Variation	52
5 Effects of Pilot Model Remnant	53
5.1 Effects on Tracking Performance	53
6 Stability	57
6.1 Definitions of Stability	57
6.2 Poles at Stability Boundaries	59
7 Control Task Parameter Effects	63
7.1 Pilot Model Parameters' Effects on Stability	63
7.2 Stick Parameters	64
7.2.1 Variation of Stick Stiffness	64
7.2.2 Compensating Stiffness with Damping and Inertia	65
7.2.3 Effects on Stability	65

7.2.4	Effects on Performance	66
7.3	Target and Disturbance Signals	67
7.4	Pilot Adaptation	67
7.4.1	Cognitive Response	69
7.4.2	Proprioceptive Feedback	72
7.4.3	Parameter Dependency	72
8	Experiment Design	77
8.1	Experiment 1: JND Measurement	77
8.1.1	Hypothesis	78
8.2	Experiment 2: Control Task	78
8.2.1	Parameter Estimation	79
8.2.2	Hypothesis	79
9	Conclusion	81
IV	Preliminary Research Appendices	85
E	Root locus of varying K_p, K_v and K_f	87
F	Tuned Pilot Model Parameters at BW1 and BW3	95
G	Tuning selected model parameters with limited noise realizations	97
H	Final tuning of selected model parameters with 50 noise realizations	99

List of Figures

A.1	Measured and fitted results of subject 1 at C1.	22
A.2	Measured and fitted results of subject 1 at C3.	22
A.3	Measured and fitted results of subject 2 at C1.	23
A.4	Measured and fitted results of subject 2 at C3.	23
A.5	Measured and fitted results of subject 3 at C1.	24
A.6	Measured and fitted results of subject 3 at C3.	24
A.7	Measured and fitted results of subject 4 at C1.	25
A.8	Measured and fitted results of subject 4 at C3.	25
A.9	Measured and fitted results of subject 5 at C1.	26
A.10	Measured and fitted results of subject 5 at C3.	26
A.11	Measured and fitted results of subject 6 at C1.	27
A.12	Measured and fitted results of subject 6 at C3.	27
A.13	Measured and fitted results of subject 7 at C1.	28
A.14	Measured and fitted results of subject 7 at C3.	28
B.1	Schematic description of the detailed model of the HO neuromuscular system including intermediate signal names for analytical derivation.	29
C.1	Correlation between average HO input linearity or control activity and tracking error. Each datapoint represents the average obtained metrics of the three 120s measurement runs of one participant.	31
C.2	Correlation between theoretical GTO activity and tracking error. Each datapoint represents the average obtained metrics of the three 120s measurement runs of one participant. Each manipulator condition is analysed separately in this figure.	32
2.1	Visual display of target stick position in JND experiment [13].	43
3.1	Frequency response of proprioceptive sensors	46
3.2	Comparison of the sensitivity of primary (Ia) and secondary (II) muscle spindle endings to sinusoidal vibrations at varying frequency [23]	47
3.3	Simulated response to position perturbation in 2-DOF position control task [21]	47
4.1	Block diagram of the neuromuscular model with components described in Table 4.1	49
4.2	Spectral analysis of pilot model signals defined in Figure 4.1 with settings for PT from Table 4.2	51
5.1	Zoomed in section of the neuromuscular model blockdiagram from Figure 4.1	53
5.2	Tracking performance with varying pilot remnant intensity at 50 different noise realizations	54
5.3	Frequency response from noise input location (m_{refl}) to pilot output (u_p) with model parameters according to PT	55
6.1	Poles and zeros of entire tracking task ($H_{f,\phi}$) when becoming unstable. K_v and K_f are varied linearly from PT settings ($K_v = 2 \text{ N m s rad}^{-1}$ and $K_f = -1.5$, see Table 4.2) to $K_v = 0$ and $K_f = -5$	58
6.2	Stability regions by varying proprioceptive gains K_p , K_v and K_f	59
6.3	Isometric view of stable regions for K_p , K_v and K_f	60
6.4	Example of root locus line definition used in Figures E.1 to E.11	60
7.1	Open loop pilot dynamics between parameter settings of K_p , K_v , K_f and K_i for tasks PT, FT and RT from Table 4.2	64

7.2	Stick dynamics (H_{St}) with variation of K_{St}	65
7.3	Stick dynamics (H_{St}) with joint variation of K_{St} , B_{St} and I_{St}	66
7.4	Performance and feedback signal intensities at varying stick settings keeping other model parameters constant	66
7.5	Frequency response from u_{sup} to GTO and MS feedback at varying stick settings	68
7.6	Stability regions for K_p , K_v and K_f 'Sliced' at proprioceptive gains according to FT (see Table 4.2) (from left to right: $K_p = 9 \text{ N m rad}^{-1}$, $K_v = 2 \text{ N m s rad}^{-1}$ and $K_p = -1.5$) with different values for K_{St}	69
7.7	Isometric view of stable regions for K_p , K_v and K_f with different values for K_{St}	70
7.8	Definition of forcing function magnitudes	71
7.9	Open loop pilot dynamics from e to ϕ with very light and very heavy side stick dynamics	71
7.10	Controlled element dynamics defined in Chapter 4	72
7.11	Optimized cognitive dynamics (P_e , I_e and D_e) with changing stick dynamics	73
7.12	Tuned pilot model parameters (P_e , I_e , D_e , K_p , K_v and K_f) with changing stick dynamics at BW2 forcing functions	73
7.13	Tuned pilot model parameters (P_e , I_e , D_e , K_p , K_v and K_f) with different forcing functions	74
E.1	Root locus of $H_{u_{sup}, m_{mus}}$ at stability boundary due to too small K_f . From PT to A	88
E.2	Root locus of $H_{u_{sup}, m_{mus}}$ at stability boundary due to too large K_f . From PT to B	88
E.3	Root locus of $H_{u_{sup}, m_{mus}}$ at stability boundary due to too large K_f and large K_v . From PT to C	89
E.4	Root locus of $H_{u_{sup}, m_{mus}}$ at stability boundary due to too large K_v . From PT to D	89
E.5	Root locus of $H_{u_{sup}, m_{mus}}$ at stability boundary due to too small K_p . From PT to E	90
E.6	Root locus of $H_{u_{sup}, m_{mus}}$ at stability boundary due to too large K_p . From PT to F	90
E.7	Root locus of $H_{u_{sup}, m_{mus}}$ at stability boundary due to too large K_f . From PT to G	91
E.8	Root locus of $H_{u_{sup}, m_{mus}}$ at stability boundary due to too small K_v . From PT to H	91
E.9	Root locus of $H_{u_{sup}, m_{mus}}$ at stability boundary due to too small K_p . From PT to I	92
E.10	Root locus of $H_{u_{sup}, m_{mus}}$ at stability boundary due to too large K_p . From PT to J	92
E.11	Root locus of $H_{u_{sup}, m_{mus}}$ at stability boundary due to too large K_v . From PT to K	93
F.1	Tuned Pilot Model Parameters (P_e , I_e , D_e , K_p , K_v and K_f) with Changing Stick Dynamics at BW1 Forcing Functions	96
F.2	Tuned pilot model parameters (P_e , I_e , D_e , K_p , K_v and K_f) with changing stick dynamics at BW3 forcing functions	96
G.1	Tuned selection of pilot model parameters (K_p , P_e and D_e) with only five different noise realizations shown per bandwidth condition	98
H.1	Tuned parameters of interest (K_p , P_e and D_e) shown per bandwidth condition	100

List of Tables

A.1	Summary of measured results and estimated parameters of subject 1 at all conditions. .	22
A.2	Summary of measured results and estimated parameters of subject 2 at all conditions. .	23
A.3	Summary of measured results and estimated parameters of subject 3 at all conditions. .	24
A.4	Summary of measured results and estimated parameters of subject 4 at all conditions. .	25
A.5	Summary of measured results and estimated parameters of subject 5 at all conditions. .	26
A.6	Summary of measured results and estimated parameters of subject 6 at all conditions. .	27
A.7	Summary of measured results and estimated parameters of subject 7 at all conditions. .	28
2.1	Reference values for JND experiment	44
4.1	Mathematical model of the components of the pilot model	50
4.2	Pilot model parameters for PT, FT and RT. Values above the double line will not be discussed or investigated in detail in this thesis.	50
4.3	Baseline side stick parameters	50
5.1	Simulated signal magnitudes with BW2 forcing functions (see Section 7.3) and model parameters according to the position task without added noise signal	54
6.1	Pilot model stability classifications with numerical labels used later in Figure 6.2a	57
7.1	Forcing function bandwidth definition	67
7.2	Tracking performance and forcing function intensity at three BW conditions	70
7.3	Tuned pilot model parameters at $K_{st} = 0$, $B_{st} = 0.053 \text{ N m rad}^{-1}$ and $I_{st} = 0.00265 \text{ N m rad}^{-1}$	74
7.4	Pilot model signal/parameter dependency hypotheses	75
7.5	Expected trends of pilot model parameters of interest with changing task parameters based on fitted parameters (Figures F.1, F.2, 7.12, 7.13 and H.1)	75
8.1	Experiment matrix for JND experiment	77
8.2	Experiment matrix for control task experiment	78

List of Abbreviations

General

CD Control Device

HO Human Operator

Haptic Perception Experiment

GTO Golgi Tendon Organ

JND Just Noticeable Difference

MS Muscle Spindle

Manual Control Experiment

CE Controlled Element

CF Crest Factor

DI Double Integrator

DFT Discrete Fourier Transform

MLE Maximum Likelihood Estimator

RMS Root Mean Square

SNR Signal to Noise Ratio

VAF Variance Accounted For

List of Symbols

Haptic Perception Experiment

Symbol	Description	Unit
K_r	Reference manipulator stiffness	[N m rad ⁻¹]
K_c	Controlled manipulator stiffness	[N m rad ⁻¹]
δ_K	Stiffness increase K_c compared to K_r	[N m rad ⁻¹]
ΔK_{JND}	Just noticeable difference of stiffness	[N m rad ⁻¹]
W_K	Weber fraction of stiffness	[%]
X_{JND}	Increase of W_K at force conditions compared to position conditions ..	[%]
W_F	Weber fraction of force	[%]
W_P	Weber fraction of position	[%]
P_r	Applied manipulator deflection at the reference stiffness	[rad]
F_r	Exerted force on the manipulator at the reference stiffness	[N m]
P_c	Applied manipulator deflection at the controlled stiffness	[rad]
F_c	Exerted force on the manipulator at the controlled stiffness	[N m]
O_{ans}	Correctness of distinguishing the higher manipulator stiffness	correct or incorrect
\hat{C}_F	Force strategy model agreement of one trial	[-], 0 or 1
C_F	Force strategy model agreement rate of one measurement run	[-], decimal between 0 and 1
\hat{C}_P	Position strategy model agreement of one trial	[-], 0 or 1
C_P	Position strategy model agreement rate of one measurement run	[-], decimal between 0 and 1
b_p	Position reproduction bias in force conditions	[%]
b_f	Force reproduction bias in position conditions	[%]

Manual Control Experiment

Symbol	Description	Unit
K_{CD}	Manipulator stiffness	[N m rad ⁻¹]
B_{CD}	Manipulator damping	[N m s rad ⁻¹]
I_{CD}	Manipulator inertia	[kg m ²]
K_{stick}	Manipulator gain	[cm rad ⁻¹]
$x(t)$	Controlled element position	[cm]
$f_t(t)$	Target signal	[cm]
$u(t)$	HO input	[cm]
RMS_u	HO control activity	[cm]
$u_s(t)$	Phase-shifted HO input	[cm]
$\tilde{u}(t)$	Average HO input between measurement runs	[cm]
$e(t)$	Error signal	[cm]
RMS_e	Root mean square tracking error	[cm]
$\bar{e}(t)$	Average error signal between measurement runs	[cm]
ω_t	Frequencies where the target signal has energy	[rad s ⁻¹]
$\Gamma_{u,f_t}(\tilde{\omega}_t)$	HO input coherence with target signal	[-]
$S_{u,f_t}(j\omega)$	HO input cross power-spectral density with target signal	[cm ² /(rad/s)]
$S_{e,f_t}(j\omega)$	Error signal cross power-spectral density with target signal	[cm ² /(rad/s)]
$H_P(j\omega)$	HO describing function	[-]
$H_6(j\omega)$	Simple neuromuscular model	[-]
$H_{NMS-CD}(j\omega)$	Neuromuscular model with GTO and MS feedback and manipulator	[rad/(Nm)]
T_L	HO equalization lead time constant	[s]
ζ_{nm}	HO neuromuscular damping ratio	[-]
B_g	Skin grip damping	[N m s rad ⁻¹]
K_g	Skin grip stiffness	[N m rad ⁻¹]
I_{arm}	Arm inertia	[kg m ²]
B_i	Intrinsic muscle damping	[N m s rad ⁻¹]
K_i	Intrinsic muscle stiffness	[N m rad ⁻¹]
K_p	Position feedback gain in Muscle Spindles	[N m rad ⁻¹]
K_v	Velocity feedback gain in Muscles Spindles	[N m s rad ⁻¹]
K_f	Force feedback gain in Golgi Tendon Organ	[-]
τ_d	Transport delay time constant in MS and GTO	[s]
$\hat{\theta}$	Maximum likelihood estimated optimal parameter vector:	
K_e	HO equalization gain	[N m cm ⁻¹]
T_I	HO equalization lag time constant	[s]
τ_e	HO delay time constant	[s]
ω_{nm}	HO neuromuscular natural frequency	[rad s ⁻¹]
Q_{MLE}	Maximum likelihood estimator reward function	[-]
$u_{sim}(t)$	Simulated HO input	[cm]
VAR_{10}	Variance Accounted For windowed over the next 10 s	[%]
$u_{GTO}(t)$	Golgi Tendon Organ feedback signal	[N m]
$u_{MS}(t)$	Muscle Spindle feedback signal	[N m]
σ_{GTO}	Golgi Tendon Organ activity (standard deviation of u_{GTO})	[N m]
σ_{MS}	Muscle Spindle activity (standard deviation of u_{MS})	[N m]
Change of metrics at zero stiffness compared to non-zero stiffness:		
Y_{RMS_e}	Change of tracking error	[%]
Y_{RMS_u}	Change of control activity	[%]
Y_{RMS_Γ}	Change of HO input coherence	[%]



Scientific Paper

Proprioceptive Qualities in Manual Control

Menno Boogaard

Faculty of Aerospace Engineering

Delft University of Technology

Delft, The Netherlands

m.boogaard@student.tudelft.nl

Abstract—Human force proprioception has previously been shown to be important in manual control tasks. Recent experiments suggest that force proprioception is more accurate than position proprioception. Still, knowledge about proprioceptive qualities and their relevance in manual control is lacking or inconsistent. This paper aims to experimentally establish the respective difference in force and position perception performance and attempts to demonstrate its influence on the neuromuscular system in manual control tasks and on which manipulator properties are optimal. The first experiment confirmed that the force sensing Golgi Tendon Organ (GTO) is more accurate than position sensing Muscle Spindles, by measuring smaller human just noticeable differences of force than of position in an experiment of discriminating side-stick manipulator stiffness at various conditions. Offline simulations of a detailed model of the neuromuscular system in a manual control task validated higher GTO activity with non-zero stiffness manipulators than zero stiffness. The second experiment measured human control behavior in a double integrator controlled element pursuit task with varying manipulator stiffness intended to affect GTO activity. Zero stiffness manipulators showed worse tracking performance and lower degree of linearity of human control inputs which is related to less accurate control actions and higher uncertainty of quasi-linear human operator models. The two experiments combined demonstrate that humans' neuromuscular force sensors are more accurate than position sensors and that higher manipulator stiffness inducing higher force sensor activity results in more accurate control behavior.

Index Terms—Stiffness JND, Golgi Tendon Organ, Muscle Spindles, proprioception, man-machine systems, pursuit control, human control models, parameter estimation

I. INTRODUCTION

PROPRIOCEPTION in the human neuromuscular system is governed by Golgi Tendon Organs (GTO) and Muscle Spindles (MS). The Muscle Spindles, responsible for sensing muscle length and stretch velocity have previously been thought to be the dominant sensor in neuromuscular control [1]. Research showed, however, that the Golgi Tendon Organ, responsible for sensing muscle force, also plays an important role [2]. Recent research into haptic perception thresholds of changes in mechanical properties suggests that human's force perception is more accurate than position perception [3]. This could have significant implications for manual control tasks. A mapping of responsive force and position perception qualities would allow better understanding of how the human operator (HO) perceives the movements and forces of a manual control device, which can be useful in the design of haptic support systems [4] but also passive manipulators.

If force perception is indeed more accurate, one could imagine that a haptic support system may be more effective if it is more based on force cues. Design and qualification of simulators will also benefit from knowledge about the qualities of proprioceptive sensors. Furthermore, predicting pilot control inaccuracies is an important part of many studies of manual control behavior [5]–[9], where knowledge about inaccuracies of the human operator's proprioceptive sensors can be integrated.

In previous studies, experiments have been conducted to measure just noticeable difference (JND) of force [10]–[12] and the JND of position [13], [14] separately. However, making an accurate comparison between the two based on numerous different studies with varying experimental setups is impractical. In one study, both the force JND and position JND of index finger movements were measured [15]. This scenario is considerably different from arm movements made when performing a control task with a side-stick manipulator. Present research aims to make an accurate comparison of human force and position sensing accuracy of arm movements through measuring both force and position JNDs with a nearly identical experiment setup with a side-stick manipulator.

By varying the manipulator dynamics in a manual control task, it would then be possible to reveal what roles force and position sensing play in a manual control task. In previous studies, changing tracking performance was measured between various *non-zero* side-stick manipulator stiffness configurations [16], [17]. Present research aims to show how tracking performance is affected when GTO feedback in the HO neuromuscular system is removed. This is done by comparing tracking performance with a manipulator with zero stiffness with non-zero stiffness manipulators. With the zero stiffness manipulator, no spring force that induces GTO feedback in the HO neuromuscular system is present.

This paper focuses on a passive side-stick manipulator which is considered in two separate experiments. The first experiment, discussed in Section II, aims to establish the suggested better accuracy of GTO compared to MS in a manipulator stiffness discrimination task. According to Weber's law, the minimum threshold of changes in mechanical properties such as stiffness is reported as a constant fraction of the reference stimulus, known as the Weber fraction [18]. This is known to hold up to a minimum reference stiffness. The first goal of the conducted experiment is to demonstrate the qualities of human force perception compared to position

perception across various conditions. Secondly, it will be investigated if the selected conditions cross the minimum reference stimulus for Weber's law to hold.

The second experiment, discussed in Section III, aims to show how the qualities of GTO and MS affect human operator performance in a manual control task. Higher manipulator stiffness is expected to induce more activity of GTO compared to MS. Three stiffness settings are tested to relate the activity of the more accurate GTO to better control behavior. To validate the expected higher GTO activity with higher manipulator stiffness, a detailed model of the neuromuscular system will be used [19], contrary to a simpler model of the neuromuscular dynamics used commonly in pilot identification [5]–[9]. The second part of this paper also gives an outline of how the detailed neuromuscular model can be used to describe the human operator in a manual control task.

Sections II and III follow the same global structure: The respective experiment setups are described first; afterwards, the attained results and their implications are discussed. Section IV aims to show a correlation between the measured results of the two experiments and Section V draws the final conclusions.

II. HAPTIC PERCEPTION PERFORMANCE

In previous research into human perception thresholds of changing side-stick manipulator stiffness, two different visual representations were used, one of which required subjects to discriminate stiffness change by means of a position comparison, and the other visual required subjects to discriminate stiffness change by means of a force comparison. A relatively smaller difference of stiffness was noticeable for humans when comparing forces than when comparing positions. [3]

This finding suggests that the components of the neuromuscular system that measure force, GTO, are more accurate than the position sensing Muscle Spindles. The first experiment is designed to investigate whether this respective performance difference between GTO and MS holds over a range of conditions. Requiring the human operator to discriminate stiffness based on comparing forces is done by ensuring constant deflections of the control device. Position comparison is induced by fixing the applied force.

A. Experiment

Using an earlier established procedure [3], subjects were asked to compare the reference stiffness of a side-stick manipulator, K_r , with the controlled stiffness, $K_c = K_r + \delta_K$, $\delta_K > 0$, during two periods of 5 s separated by 1.2 s with equal probability of the reference, K_r , or controlled stimulus, K_c , first. When the subject correctly selected the stiffer manipulator twice in a row, δ_K was reduced. A ratio of 0.5488 between the down stepsize and the up stepsize in this one-up/two-down adaptive staircase procedure was used. This means that the procedure converges to an 80.35 % correct measurement of the upper stiffness JND, ΔK_{JND} [20]. Eq. (1) gives this threshold as a fraction of the reference stiffness known as the Weber fraction, which, according to Weber's law, is constant until a minimum reference stimulus [18]. This experiment has been

conducted in previous work and the evaluated metrics for the present experiment discussed in Section II-E are also based on this previous research [3].

$$W_K = \frac{\Delta K_{JND}}{K_r} \times 100\% \quad (1)$$

Subjects looked at an LCD screen, see Figure 1, on which information about the side stick manipulator movement was displayed in one of two ways. Either the applied moment on the manipulator, F , or the achieved position of the manipulator, P , was displayed with a circle. Displaying F is referred to as the force condition and displaying P as the position condition. Subjects were instructed to deflect the manipulator to the left and back such that the circle follows a target signal indicated by a cross, which ramps up in 1.5 s, holds constant for 2 s and ramps down in 1.5 s. The display showed a 1.5 s preview of this ramp signal, see Figure 2. We define $\{F_r, P_r\}$ as the average applied force and position during the 2 s constant part of the ramp signal at the reference stiffness and $\{F_c, P_c\}$ at the controlled stiffness.

When the circle on the display showed P , it was ensured that the subject applied the same manipulator position between K_r and K_c ($P_c = P_r$ and $F_c = F_r \times (W_K + 1)$). Now, the measured Weber fraction of stiffness is equal to the Weber fraction of force, W_F , because subjects had to discriminate stiffness based on the difference in applied force.

Equally, when the circle on the display showed F , the Weber fraction of position was measured ($F_c = F_r$ and $W_K = W_P$) because stiffness discrimination was based on position comparison.



Fig. 1. Experimental setup of the LCD screen and side-stick manipulator. [3]

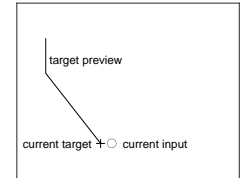


Fig. 2. Example of the visual display in the JND experiment at 0.5 s into the 5 s target signal. [3]

B. Conditions

W_K was measured at eight different conditions described in Table I. F , or P was visually displayed and hereby controlled between K_c and K_r . K_r was varied between two levels, labelled L and H. Finally the magnitude of the required target deflection to make the circle follow the displayed ramp was varied between $P_r = 0.25$ rad (l) and $P_r = 0.37$ rad (h). In the force conditions, this means that $F_r = F_c$ is defined by the target deflection times K_r . For example, for the first condition in Table I, F-L-l, $F_r = F_c = 2 \text{ N m rad}^{-1} \cdot 0.25 \text{ rad} = 0.5 \text{ N m}$.

In summary, the three independent variables, K_r , P_r and the visual type were varied between two levels, resulting in eight conditions. Varying the visual type was intended to reveal a

difference of human's respective accuracy of sensing force and position (W_F and W_P). K_r and P_r were both varied between two levels to show whether any difference between W_F and W_P exists at various conditions. This is also done to possibly find a lower bound where Weber's law no longer holds.

The visually displayed ramp was identical between all eight conditions. The inertia and damping of the manipulator were constant at $I = 0.01 \text{ kg m}^2$ and $B = 0.05 \text{ N m s rad}^{-1}$. Conditions F-H-1 and P-H-1 are equal to the conditions used in the experiment conducted earlier [3].

TABLE I
CONDITIONS FOR THE JND EXPERIMENT. DARK GRAY INDICATES IF P_r OR F_r WAS DISPLAYED VISUALLY. LIGHT GRAY HIGHLIGHTS THE CONDITIONS USED IN THE PREVIOUS EXPERIMENT [3].

Label	K_r [N m rad $^{-1}$]	P_r [rad]	F_r [N m]	Controlled input between K_r and K_c
F-L-1	2	0.25	0.5	$F_r = F_c$
F-L-h	2	0.37	0.74	$F_r = F_c$
F-H-1	3.5	0.25	0.875	$F_r = F_c$
F-H-h	3.5	0.37	1.295	$F_r = F_c$
P-L-1	2	0.25	0.5	$P_r = P_c$
P-L-h	2	0.37	0.74	$P_r = P_c$
P-H-1	3.5	0.25	0.875	$P_r = P_c$
P-H-h	3.5	0.37	1.295	$P_r = P_c$

C. Apparatus

The experiment was conducted in the Human-Machine Interaction Laboratory at the faculty of Aerospace Engineering, TU Delft. Subjects took place in a pilot seat in front of an LCD screen and controlled the side-stick manipulator movement left to right about the roll axis, with the subjects' hand positioned 9 cm above its pivot point. The manipulator was electro-hydraulically controlled by a computer at 2500 Hz to simulate the mechanical mass-spring-damper properties. The LCD showed the controlled input and target as in Figure 2 and a bar indicating the point in time in the set of two 5 s ramps.

D. Procedure

Each JND measurement run consisted of an adaptive staircase procedure where in the first trial, the stiffness difference was 50% ($\frac{\delta K}{K_r} = 0.5$). When the subject correctly identified the higher stiffness manipulator twice in a row, δK in the next trial was reduced and with each incorrect answer, δK was

increased, i.e., a one-up/two-down staircase. In the staircase procedure, a reversal is defined as a trial where the staircase curve changes direction. A one-up/one-down staircase was used until the first reversal occurred for faster convergence. The procedure was stopped after the seventh reversal or when the total number of trials reached 40. The staircase procedure typically converged in 30 trials totalling seven minutes for one JND measurement run. This human subject experiment was approved by the TU Delft Human Research Ethics Committee.

One training run was performed at the start of the session to familiarize the subject with the task. The eight conditions were tested by each of the eight participants in a session of approximately one hour with breaks of at least one minute between each condition and three minutes between the fourth and fifth. In order to minimize ordering effects due to fatigue or learning within one session, the order of the conditions was balanced between the subjects according to the balanced Latin square in Table II. This Latin square design balances the effects of conditions immediately tested after another [21]. The eight participants, aged 22-25 years old, reported no impairments to the right arm or eyes.

E. Metrics

The measured data during the staircase procedure after the third reversal were used for analysis. These data include $\{F_r, P_r\}$, $\{F_c, P_c\}$, K_c and subjects' answers' correctness, O_{ans} . These were then processed in the following ways.

1) W_K : ΔK_{JND} was measured as the average of K_c of the last four reversals minus K_r . This minimum threshold of perceivable difference is divided by the reference stimulus, K_r , to obtain the Weber fraction of stiffness, see Eq. (1).

2) *Strategy agreement rate*: When subjects discriminate the stiffness based on comparing the applied position between K_r and K_c , this is referred to as the position strategy. With the force strategy, discrimination is based on comparing applied forces to the manipulator. These strategies can be described by the position strategy model and force strategy model. The position strategy model agreement, \hat{C}_P , and the force strategy model agreement, \hat{C}_F , evaluated for one trial are defined by Eqs. (2) and (3), respectively. Averaged over the trials after the third reversal in one run, these become the strategy models' agreement rates, C_P and C_F . From these agreement rates, one can conclude whether participants discriminated the stiffness difference based on a comparison of positions or of forces. [3]

TABLE II
LATIN SQUARE OF CONDITION ORDER IN THE JND EXPERIMENT.

Subject	Conditions							
1	F-L-1	P-L-1	P-H-h	F-L-h	F-H-h	P-L-h	P-H-1	F-H-1
2	P-L-1	F-L-h	F-L-1	P-L-h	P-H-h	F-H-1	F-H-h	P-H-1
3	F-L-h	P-L-h	P-L-1	F-H-1	F-L-1	P-H-1	P-H-h	F-H-h
4	P-L-h	F-H-1	F-L-h	P-H-1	P-L-1	F-H-h	F-L-1	P-H-h
5	F-H-1	P-H-1	P-L-h	F-H-h	F-L-h	P-H-h	P-L-1	F-L-1
6	P-H-1	F-H-h	F-H-1	P-H-h	P-L-h	F-L-1	F-L-h	P-L-1
7	F-H-h	P-H-h	P-H-1	F-L-1	F-H-1	P-L-1	P-L-h	F-L-h
8	P-H-h	F-L-1	F-H-h	P-L-1	P-H-1	F-L-h	F-H-1	P-L-h

$$\text{if } P_c < P_r \begin{cases} \text{if } O_{ans} = \text{correct,} & C_P = 1 \\ \text{if } O_{ans} = \text{incorrect,} & C_P = 0 \end{cases} \quad (2)$$

$$\text{if } P_c > P_r \begin{cases} \text{if } O_{ans} = \text{correct,} & C_P = 0 \\ \text{if } O_{ans} = \text{incorrect,} & C_P = 1 \end{cases}$$

$$\text{if } F_c > F_r \begin{cases} \text{if } O_{ans} = \text{correct,} & C_F = 1 \\ \text{if } O_{ans} = \text{incorrect,} & C_F = 0 \end{cases} \quad (3)$$

$$\text{if } F_c < F_r \begin{cases} \text{if } O_{ans} = \text{correct,} & C_F = 0 \\ \text{if } O_{ans} = \text{incorrect,} & C_F = 1 \end{cases}$$

The agreement rates of the position strategy model and force strategy model are both evaluated for all force and position conditions and grouped according to the expectation about which strategy is expected to dominate in which condition, see Section II-F. These expectations yield the dominant and non-dominant strategy. In force conditions, the position strategy is called dominant and in position conditions, the force strategy is referred to as dominant. If an agreement rate is significantly higher than 50 %, it can be said that the corresponding model explains some of the decisions made by the participant.

3) *Reproduction bias*: The measured data can also be used to evaluate how accurately subjects reproduced the controlled manipulator input between K_r and K_c . For the force conditions, we define the force bias as the bias of reproducing the visually displayed force according to Eq. (4). Similarly, Eq. (5) defines the bias of reproducing the required manipulator position in the position conditions. Note that b_F is defined positive when larger forces are applied with the stiffer manipulator, K_c , and b_P is defined positive when smaller deflections are made with the stiffer manipulator. When subjects follow the visual target ramp equally closely between the higher stiffness, K_c , and the lower stiffness, K_r , these biases are zero. The biases are measured to show how well the controlled inputs are reproduced between K_r and K_c .

$$b_F = \frac{F_c - F_r}{F_r} \times 100 \% \quad (4)$$

$$b_P = -1 \times \frac{P_c - P_r}{P_r} \times 100 \% \quad (5)$$

F. Hypotheses

1a) *Smaller W_K with position visual compared to force visual*: The measured Weber fraction of stiffness is expected to be lower across all conditions where stiffness discrimination is based on the force difference (position conditions) than when it is based on position difference (force conditions).

1b) *No effect of K_r on the Weber fractions*: The two levels of K_r are not expected to have an effect on W_K . Weber's law (Eq. (1)) states that the minimal noticeable threshold is a constant fraction of the reference stiffness. Hence, no difference in results is expected between lower or higher K_r .

1c) *Small effect of P_r on the Weber fractions*: The different levels of target deflections are expected to have some effect on W_K . Weber's law is known to hold for changing mechanical properties [22]. However, this only holds up to a minimum reference stimulus. Therefore, the conditions with a lower target deflection ($P_r = 0.25$ rad) are expected to result in slightly higher measured Weber fractions of stiffness.

1d) *Position strategy in force conditions and vice versa*: The position strategy model is expected to agree most in force conditions and the force strategy model is expected to agree most in the position conditions. In the force conditions, participants are visually guided to apply equal forces between K_r and K_c . We can thus expect the position strategy to be used most in these conditions. Similarly, when applied positions

are kept constant in the position conditions, participants are expected to base their decisions on the force strategy.

G. Results

First, the statistical analysis procedure that was used for all metrics will be discussed. Afterwards, the results are examined per metric. This approach is chosen such that only significant results are discussed in detail. Figures 3 to 7 show the results with each datapoint representing one JND measurement run.

Shapiro-Wilk normality tests were conducted for each metric separately at each condition and reported in Table III. Three of the 24 conducted tests showed a significant departure from normality. Thus, the parametric analysis of variance (ANOVA) that was performed should be interpreted with care.

A three-way ANOVA was conducted for each metric separately. The results in Table IV show that only the visual type (force or position) has a significant effect on W_K . The effect of K_r is clearly insignificant showing that Weber's law holds here. The measured effect of the target deflection magnitude, P_r , was larger but still insignificant. Sphericity is not an issue here because the independent variables only have two levels.

TABLE III
SIGNIFICANCE p OF SHAPIRO-WILK NORMALITY TESTS OF JND METRICS. GRAY VALUES INDICATE A SIGNIFICANT DEPARTURE FROM NORMALITY.

Condition	W_K	Dominant model agreement rates	Non-dominant model agreement rates	Reproduction bias (b_P or b_F)
F-L-l	0.171	0.821	0.788	0.916
F-L-h	0.250	0.915	0.178	0.519
F-H-l	0.684	0.308	0.504	0.005
F-H-h	0.735	0.194	0.203	0.110
P-L-l	0.113	0.614	0.924	0.054
P-L-h	0.353	0.375	0.074	0.277
P-H-l	0.038	0.067	0.706	0.519
P-H-h	0.049	0.447	0.374	0.627

TABLE IV
THREE-WAY ANOVAS OF JND METRICS. GRAY ROWS INDICATE A SIGNIFICANT EFFECT OF THE INDEPENDENT VARIABLE ON THE CONSIDERED METRIC.

Metric	Independent variable	$F(1,7)$	p
W_K	Visual Type	14.066	0.007
	K_r	0.135	0.724
	P_r	1.891	0.212
Dominant model agreement Rates	Visual Type	0.089	0.774
	K_r	3.659	0.097
Non-dominant model agreement Rates	P_r	0.041	0.845
	Visual Type	0.737	0.419
	K_r	0.244	0.636
Reproduction Bias	P_r	0.917	0.370
	Visual Type	15.760	0.005
	K_r	0.467	0.516
	P_r	4.764	0.065

1) *Stiffness JND*: Figure 3 shows an average Weber fraction of stiffness in the position conditions of 38.4 % and in the force conditions 16.6 %. The ANOVA shows no effect of K_r or P_r .

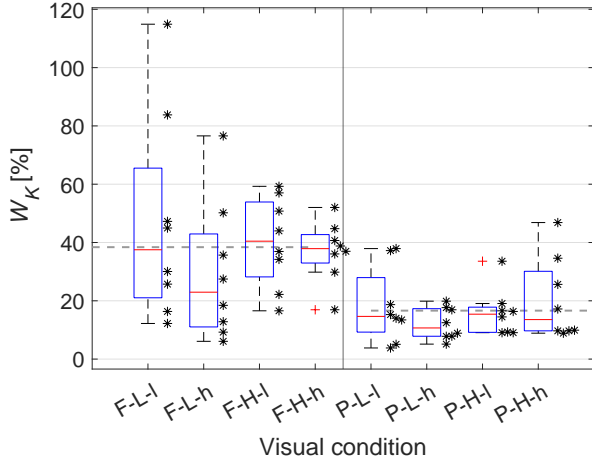


Fig. 3. Weber fraction of stiffness per condition.

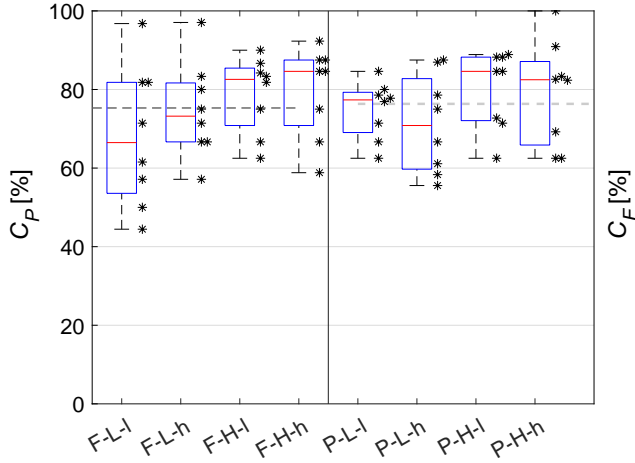


Fig. 4. Dominant strategy model agreement rate per condition.

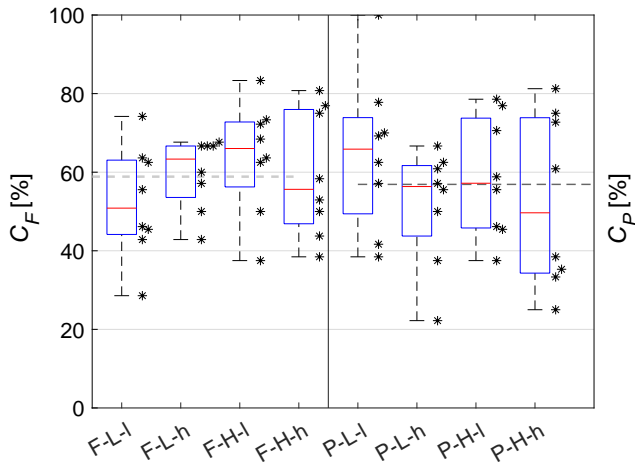


Fig. 5. Non-dominant strategy model agreement rate per condition.

2) *Model Agreement Rates*: The model agreement rates are compared to 50 % to say if the corresponding model explains some of the decisions made by the participant. This is done with one-sample t-tests reported in Table V. Figure 4 shows that the dominant strategy models have an average agreement rate of 75.3 % in the force conditions and 76.3 % in the position conditions. No significant difference between any of the conditions was found with the ANOVA. T-tests showed that the distributions' means were significantly higher than 50 %.

TABLE V
ONE-SAMPLE T-TESTS COMPARED TO 50 % OF THE STRATEGY MODEL AGREEMENT RATES. GRAY HIGHLIGHTS THE SIGNIFICANT P-VALUES.

Condition	Dominant model		Non-dominant model	
	$t(7)$	p	$t(7)$	p
F-L-l	2.852	0.025	2.084	0.076
F-L-h	5.694	0.001	0.297	0.775
F-H-l	8.297	< 0.001	1.597	0.154
F-H-h	7.168	< 0.001	0.350	0.736
P-L-l	9.527	< 0.001	0.463	0.657
P-L-h	4.753	0.002	2.982	0.020
P-H-l	8.593	< 0.001	2.727	0.029
P-H-h	6.138	< 0.001	1.67	0.139

In Figure 5, the non-dominant strategy agreement rates are shown with an average of 58.9 % in the force conditions and 56.9 % in the position conditions. The eight separate one-sample t-tests in Table V only showed that only for P-L-h and P-H-l, these distributions have means significantly higher than 50 %. No difference between the conditions was shown by the ANOVA so all non-dominant strategy agreement rates of all conditions can be grouped together and have an average of 57.9 % which was significantly higher than 50 %, $t(63) = 7.882$, $p < 0.001$. Hence, the non-dominant models do also sometimes explain the subjects' decision strategy. Still, the dominant model agreement rates were higher leading to the conclusion that in the force conditions, subjects based their answers most on different applied positions and in position conditions, decisions were more based on different forces which agrees with Hypothesis 1d.

3) *Reproduction Bias*: The ANOVA showed that the reproduction bias in the force conditions was significantly higher than in the position conditions. No effects of K_r and P_r exist so all force biases can be grouped and all position biases are grouped. The data of all reproduction biases of force shown in Figure 6 together are found to be significantly different from zero, $t(31) = 5.101$, $p < 0.001$. Also a systematic bias of reproduced position existed in the position conditions, $t(31) = 2.954$, $p = 0.006$. The average reproduction biases are $\tilde{b}_F = 1.32\%$ and $\tilde{b}_P = 0.49\%$. These biases in the force conditions show that, despite visually guiding participants to apply equal forces, higher forces were applied with the stiffer manipulator. In the position conditions smaller positions were applied with the stiffer manipulator even though the visual display allowed participants to apply the same displacement.

4) *JND of force and position*: In Section II-G2, it was shown that subjects made most decisions in the force conditions based on a comparison of positions, and in the position

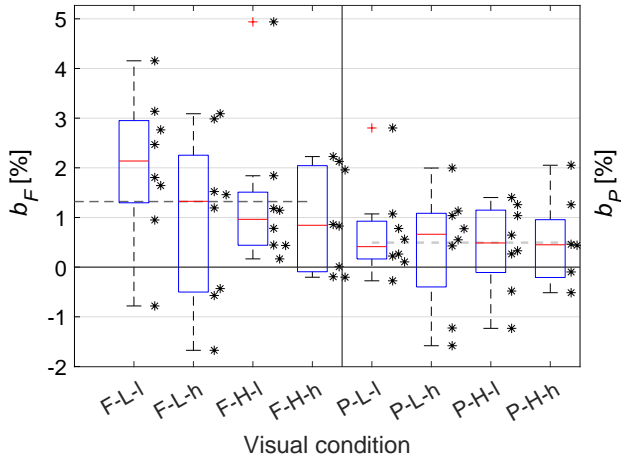


Fig. 6. Reproduction bias per condition.

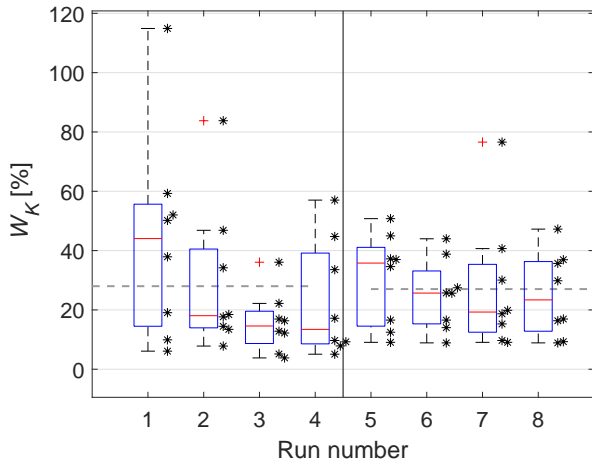


Fig. 7. Weber fraction of stiffness per moment in time within the experiment session.

conditions based on a force comparison. The measured Weber fractions of stiffness can thus be related to the just noticeable difference of position and force, respectively.

A way to convert the Weber fraction of stiffness, W_K , to the Weber fraction of force, W_F , in the position conditions, using systematic non-zero position reproduction bias, b_P , according to Eq. (7), was used earlier [3]. Eq. (6) is a variation, used in the force conditions to convert W_K to the Weber fraction of position, W_P , using systematic non-zero force bias b_F .

$$W_P = \frac{P_c - P_r}{P_r} = \frac{F_c/K_c - F_r/K_r}{F_r/K_r} = \frac{\tilde{b}_F - W_K}{W_K + 1} \quad (6)$$

$$W_F = \frac{F_c - F_r}{F_r} = \frac{P_c K_c - P_r K_r}{P_r K_r} = W_K(1 - \tilde{b}_P) - \tilde{b}_P \quad (7)$$

The ANOVA only showed a significant effect of the visual type on the reproduction bias. Hence, all stiffness Weber fractions in force conditions should be corrected with expectation

of b_F and in position conditions with b_P , i.e., the averages over all force conditions, \tilde{b}_F , and position conditions \tilde{b}_P , respectively. With the measured averages of W_K , Eqs. (6) and (7) yield the average lower position JND, $W_P = -26.8\%$, and the average upper force JND, $W_F = 16.0\%$. The lower position JND was measured since the higher controlled stiffness, K_r , results in smaller manipulator deflections.

5) *Ordering Effects*: All measured Weber fractions were compared based on the moment in time in the experiment session irrespective of the experiment condition in Figure 7. A Greenhouse-Geisser corrected ANOVA showed no effect of the moment in time within the session, $F(7,49) = 1.213$, $p = 0.327$. Hence, the data do not show any clear ordering effects caused by learning or fatigue with this experiment.

H. Discussion

The measured values of W_K are higher than those found in the earlier experiment (15% and 9% for the force and position condition, respectively) [3]. However, in other work, $W_K = 22\%$ has also been reported. The used staircase procedure is only correct up to 80.35%. One cause of this inherent uncertainty is the random guessed answers subjects give when the difference between K_r and K_c is smaller than their just noticeable difference. A different possible cause for the observed high Weber fractions is that participants' performance may have been worse because of the duration of the experiment session consisting of repeated mentally demanding experiment runs. Furthermore, the results are widely spread, possibly caused by differences between our subjects, but also by the uncertainty of JND measurement with this procedure.

The presented results can be taken as compelling evidence that human's haptic perception of force is more precise than that of position. This was shown to hold for the range of conditions that was tested. The relative difference between W_P and W_F is approximately a factor two. This confirms Hypothesis 1a and is consistent with the difference that was measured earlier [3]. We can thus conclude that, in the conducted experiment, the Golgi Tendon Organ is more accurate than the Muscle Spindles.

Irrespective of the visual type (F or P), the four different conditions from changing the reference stiffness, K_r , and target deflection magnitude, P_r , were not shown to have a measurable effect on the conducted experiment. The two levels of reference stiffness were not shown to have an effect which confirms Hypothesis 1b. Some effect of P_r on the measured Weber fraction of stiffness seems distinguishable from Figure 3. However, the ANOVA showed that this was insignificant, $p = 0.212 > 0.05$, so Hypothesis 1c is rejected.

In future research, a lower bound of P_r and K_r until which Weber's law holds could be found more effectively by investigating the effect of P_r or K_r in isolation rather than the mixed experiment conditions of present experiment. A lower number of conditions with only one independent variable produces significant results more easily. Furthermore, a higher number of participants is preferable considering the inherent uncertainty of the JND measurement procedure.

III. MANUAL CONTROL

In the second experiment, the effects of the superior performance of the Golgi Tendon Organ compared to the Muscle Spindles are investigated in a dynamic control task. A reasonably rudimentary control task is selected to allow for a clear performance comparison of GTO and MS. This classical control task with a side-stick control device has been documented and frequently adapted and researched [23], [24].

A. Control Task

During this experiment, subjects were instructed to minimize their tracking error between the visually displayed target signal and controlled element (CE) position, $e(t) = f_t(t) - x(t)$. This is known as a pursuit tracking task since no preview of the target signal was displayed. Using a passive side-stick manipulator with different mass-spring-damper dynamics, subjects controlled the CE with double integrator (DI) dynamics described by Eq. (8) with $K_{CE} = 1.5$. DI dynamics were selected to be able to see the effects of the manipulator conditions in a difficult control task.

With these dynamics, even a low bandwidth signal is difficult to track so a “6-4” spectrum is used [23]. The target signal, $f(t)$ is a sum of $N_f = 10$ sinusoids. Hence, it only has power at the forcing frequencies, ω_t . The amplitude of the sinusoids at the four highest frequencies are reduced by a factor ten resulting in a power attenuation of a factor 100. Different realizations are used to prevent subjects from memorizing the movements of $f_t(t)$. Table VI and Eq. (9) describe the three different used realizations, r1, r2 and r3, of $f_t(t)$. Each run lasted 128 s of which the first 8 s run-in time are discarded.

The amplitudes, A_t , cause $f(t)$ to have standard deviation, $\sigma_{f_t} = 1.254$ cm. The phases, ϕ , ensure that $f(t)$ appears to be quasi-random while having reasonably high power without exceeding the limits of the display. This is quantified by the crest factor, $CF = \frac{\max(|f_t(t)|)}{\sigma_{f_t}} \approx 2.8$ [25], [26].

The manipulator’s mass-spring-damper dynamics were set to conditions C1, C2 and C3, as defined in Table VII. The dynamics shown in Figure 8 result from increasing the control device stiffness, K_{CD} , from 0 at C1, to 3.5 N m rad^{-1} at C3 and adjusting the damping coefficient, B_{CD} , to maintain similar damping ratios while the inertia, I_{CD} , is held constant. These conditions were selected to be able to see any difference in control behavior resulting from higher dependency on GTO than MS. The manipulator gain was held constant at $K_{stick} = 25.4 \text{ cm rad}^{-1}$.

B. Human Operator Describing Function

For now, we make the simplifying assumption that HOs only base their control actions on the error signal on the visual display. This implies that the distance between the target (cross) and the current position (circle) is the only information the pilot uses from the visual display and we effectively analyze the measured data equally to the analysis of a compensatory task. This has previously been considered a valid assumption [23]. However, recent work demonstrated a method that models HO control actions based on different

$$H_{CE}(j\omega) = \frac{K_{CE}}{(j\omega)^2} \quad (8)$$

$$f_t(t) = \sum_{i=1}^{N_f} A_t[i] \sin(\omega_t[i]t + \phi_t[i]) \quad (9)$$

TABLE VI
MULTISINE TARGET SIGNAL DEFINITION.

i	k	A_t [cm]	ω_t [rad s ⁻¹]	ϕ_1 [rad s ⁻¹]	ϕ_2 [rad s ⁻¹]	ϕ_3 [rad s ⁻¹]
1	3	0.731	0.157	1.620	2.400	3.348
2	5	0.731	0.262	5.502	3.519	0.472
3	8	0.731	0.419	4.688	1.835	4.658
4	11	0.731	0.576	1.675	0.136	4.543
5	19	0.731	0.995	2.283	1.747	4.837
6	29	0.731	1.518	4.866	3.927	5.157
7	47	0.073	2.461	5.342	1.497	5.598
8	77	0.073	4.032	4.198	1.16	0.348
9	143	0.073	7.488	1.738	4.878	0.178
10	263	0.073	13.771	1.349	5.291	0.536

TABLE VII
MANIPULATOR CONDITIONS’ MASS-SPRING-DAMPER DYNAMICS.

		C1	C2	C3
K_{CD}	[N m rad ⁻¹]	0	2.0	3.5
B_{CD}	[N m s rad ⁻¹]	0.2	0.2	0.35
I_{CD}	[kg m ²]	0.1	0.1	0.1
$\omega_{CD} (= \sqrt{\frac{K_{CD}}{I_{CD}}})$	[rad s ⁻¹]	-	4.47	5.92
$\zeta_{CD} (= \frac{B_{CD}}{2\sqrt{K_{CD} \cdot I_{CD}}})$	[-]	-	0.224	0.296

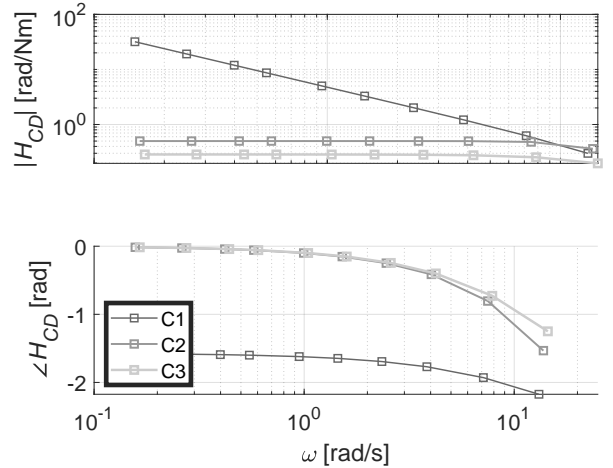


Fig. 8. Manipulator dynamics frequency response of the three conditions.

information channels [6], [9]. In pursuit tracking, three channels are available, $f_t(t)$ and $x(t)$ and the distance between the two, $e(t)$. If the model using only $e(t)$ fails to describe the measured control actions accurately, we may have to revisit the assumption that subjects only look at the visual distance between the target (cross) and target (circle). In this case, a multi-channel model may be needed.

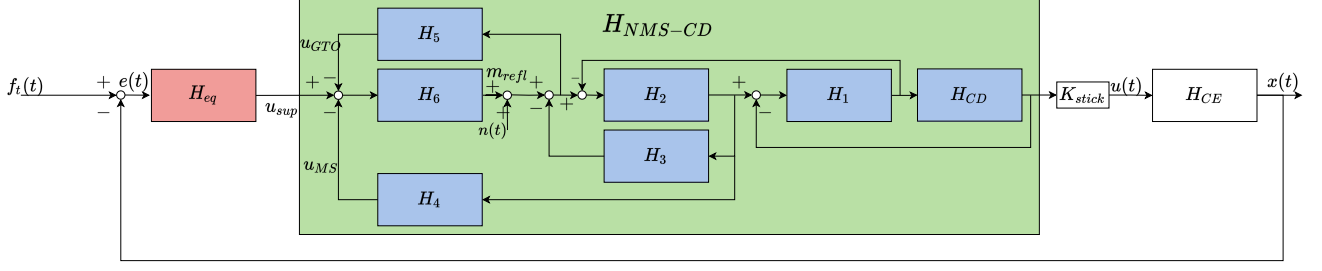


Fig. 9. Schematic description of the detailed model of the HO neuromuscular system in a pursuit tracking task assuming the HO only uses the error signal. $n(t)$ indicates the location where remnant is added for Monte Carlo simulations discussed in Section III-C.

TABLE VIII
CONSTANT HO MODEL PARAMETERS BETWEEN CONDITIONS C1, C2 AND C3.

T_L [s]	ζ_{nm} [-]	B_g [N m s rad ⁻¹]	K_g [N m rad ⁻¹]	I_{arm} [kg m ²]	B_i [N m s rad ⁻¹]	K_i [N m rad ⁻¹]	K_p [N m rad ⁻¹]	K_v [N m s rad ⁻¹]	K_f [-]	τ_d [s]
10	0.7	2	165	0.01	1	11	9	2	-1.5	0.025

TABLE IX
MATHEMATICAL DESCRIPTION OF THE COMPONENTS OF THE HO MODEL.

Description	Mathematical model
Grip dynamics	$H_1 = B_g j\omega + K_g$
Arm dynamics	$H_2 = \frac{1}{I_{arm}(j\omega)^2}$
Intrinsic muscle dynamics	$H_3 = B_i j\omega + K_i$
MS response	$H_4 = e^{-\tau_d j\omega} (K_v j\omega + K_p)$
GTO response	$H_5 = e^{-\tau_d j\omega} K_f$
Neuromuscular activation	$H_6 = \frac{\omega_{nm}^2}{(j\omega)^2 + 2\zeta_{nm}\omega_{nm}j\omega + \omega_{nm}^2}$
Manipulator	$H_{CD} = \frac{1}{I_{CD}(j\omega)^2 + B_{CD}j\omega + K_{CD}}$

The open-loop pilot response, $H_P(j\omega)$, describes HO control inputs, $u(t)$, as a function of the visually displayed error signal, $e(t)$. In most HO identification research, $H_P(j\omega)$ is modeled by Eq. (10) where the neuromuscular dynamics are typically described by a second-order system, $H_6(j\omega)$ [7], [23]. Here, the manipulator gain and dynamics are not described explicitly. HOs are assumed to adapt such that the pilot equalization, $H_{eq}(j\omega)$, describes the resulting pilot dynamics, adapted to the manipulator properties.

$$H_P(j\omega) = H_{eq}(j\omega)H_6(j\omega) \quad (10)$$

$$H_{eq}(j\omega) = K_e e^{-j\omega\tau_e} \frac{(T_L j\omega + 1)^2}{T_I j\omega + 1} \quad (11)$$

In the present research, a more detailed quasi-linear model of the HO's dynamics in a pursuit control task is used. This separately models the manipulator dynamics, including feedback from the Golgi Tendon Organ and Muscle Spindles, allowing their activity to be simulated. The model is introduced in Figure 9 and its components described in Table IX. GTO and MS are modelled by H_5 and H_4 , respectively, and include a transport delay of 0.025 s. The pilot time delay of τ_e is included in the equalization model block. The delays

TABLE X
BASELINE VALUES OF HO MODEL PARAMETERS DEPENDENT ON CONDITIONS C1, C2 AND C3.

K_e [N m cm ⁻¹]	T_I [s]	τ_e [s]	ω_{nm} [rad s ⁻¹]
0.08	1	0.25	5

are approximated by a second-order Padé time delay, given by Eq. (13). The supraspinal input, u_{sup} [Nm], is the input from the brain, into the neuromuscular system. In the present model, feedback signals from GTO and MS are subtracted from this input [27]. H_{NMS-CD} in Figure 9 represents this model, its dynamics were derived analytically for the parameter estimation procedure discussed in Section III-G2.

$$H_P(j\omega) = H_{eq}(j\omega)H_{NMS-CD}(j\omega)K_{stick} \quad (12)$$

$$e^{-\tau j\omega} \approx H_{Padé}^{2nd} = \frac{1 - \frac{1}{2}\tau^2 j\omega + \frac{1}{12}\tau^2 (j\omega)^2}{1 + \frac{1}{2}\tau j\omega + \frac{1}{12}\tau^2 (j\omega)^2} \quad (13)$$

The present model given by Eq. (12) replaces $H_6(j\omega)$ with $H_{NMS-CD}(j\omega)$ and K_{stick} compared to the traditional model in Eq. (10). When examining these frequency responses in Figure 10, we see that the magnitude of $H_{NMS-CD}(j\omega)$ starts to decrease at a higher frequency compared to $H_6(j\omega)$. This is equivalent to a higher natural frequency, i.e., higher neuromuscular stiffness, meaning that the GTO and MS feedback loops add to the neuromuscular stiffness. A significant implication of this is that, when using $H_{NMS-CD}(j\omega)$, estimated values of ω_{nm} will be lower compared to using $H_6(j\omega)$.

The gain and dynamics of the control device are included in the used model in Eq. (12), which is not the case with the simpler model from Eq. (10). This means that with the present model, the equalization gain, K_e , also includes a conversion from the visually displayed magnitude of $e(t)$ [cm] to the

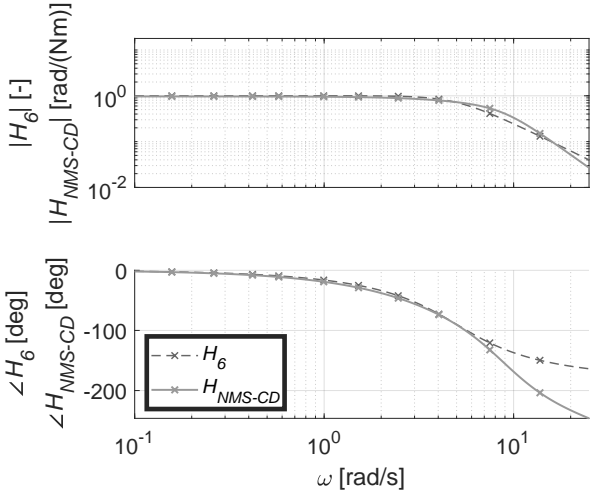


Fig. 10. Comparison between analytically derived dynamics of the simple model of neuromuscular dynamics, $H_6(j\omega)$, and the detailed model used for the present research, $H_{NMS-CD}(j\omega)$. The latter is scaled up by 13.5 dB such that the low-frequency magnitude is 0 dB. $\omega_{nm} = 5 \text{ rad s}^{-1}$ and parameters listed in Table VIII are used.

supraspinal input, $u_{sup}[\text{N m}]$. As a result, $K_e[\text{N m cm}^{-1}]$ used here will not be consistent with values of dimensionless $K_e[-]$ from literature. Note that the used model of $H_P(j\omega)$ from Eq. (12) remains dimensionless. $H_{NMS-CD}(j\omega)$ has units $[\text{rad}/(\text{N m})]$ while $H_6(j\omega)$ is dimensionless.

The used equalization model has been shown to be able to describe the human operator with a DI controlled element [28]. In the present research, only the pilot equalization gain, K_e , and lag time constant, T_I , delay time constant, τ_e , and neuromuscular natural frequency, ω_{nm} , are investigated. Their baseline values are presented in Table X, while Table VIII presents the constant pilot model parameters that are not investigated. Note that the lead time constant, T_L , is assumed constant at 10 s between the three conditions. McRuer's verbal adjustment rules state that the open-loop response of the HO and CE will have a negative slope of 20 dB/decade [23]. Hence, the HO frequency response has a positive slope of 20 dB/decade to compensate for the DI CE. Thus, a high T_L is needed with the equalization model given by Eq. (11).

C. Simulations

Figures 8 and 11 show how isolated changes of the manipulator dynamics, without adaptation of the parameters in Table VIII, affect the analytically derived dynamics, $H_P(j\omega)$. In these frequency response plots, the values for C2 and C3 are shifted to the right slightly. This will be done consistently in all frequency response graphs in this paper. Figure 11 shows an increase of the absolute value of $H_P(j\omega)$ of ~ 6 dB at the highest two frequencies with C1 compared to C3.

One would expect human operators to adapt their dynamics to the changing manipulator dynamics. For the purpose of numerical simulations of the tracking task, it is assumed that the human operator adapts by only adjusting the parameters listed in Table X. For now, we assume that the HO adjust

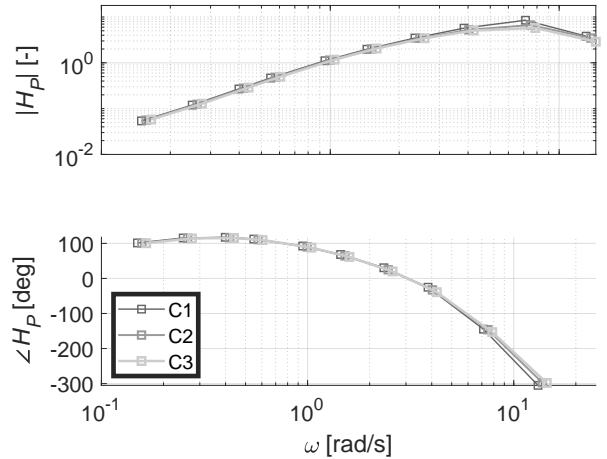


Fig. 11. Analytically derived isolated effects of the three manipulator conditions on the HO model frequency response without pilot adaptation.

the parameters in conditions C1 and C3 such that $H_P(j\omega)$ is as close as possible to its baseline dynamics with C2. The procedure used to find these parameters will be described in detail in Section III-G2. From the analytical results in Table XI, we can conclude that the human operator would compensate for increased manipulator stiffness with an increase of neuromuscular stiffness. This is represented inside $H_6(j\omega)$ by an increased ω_{nm} .

TABLE XI
CONDITION DEPENDENT PILOT MODEL PARAMETERS FOR C1 AND C3,
ANALYTICALLY ADJUSTED TO C2.

Condition	K_e [N m cm ⁻¹]	T_I [s]	τ_e [s]	ω_{nm} [rad s ⁻¹]
C1	0.0924	1.2636	0.2403	4.6387
C2	0.08	1	0.25	5
C3	0.0745	0.9103	0.2531	5.4554

The simulated experiment is conducted by adding the target signal, $f_t(t)$, and remnant, accounting for pilot behavior uncertainties. This HO remnant is represented by a Gaussian zero-mean white noise signal filtered with a first-order lag filter with break frequency 20 rad s^{-1} , added to the reflexive muscle moment, m_{refl} . The signal to noise ratio, $\text{SNR} = \frac{\sigma_{m_{refl}}^2}{\sigma_n^2}$, was either high (10), realistic (3) or low (2) [8], [29].

The standard deviations of the output signals of the numerical simulation presented in Figure 12 are calculated from the outputs of 1,000 different remnant realizations, $n(t)$, with the selected SNRs, averaged for conditions C1, C2 and C3 [8], and without adding remnant ($\text{SNR} = \infty$). We see that all signals' standard deviations increase with added noise intensity.

Without adding remnant, we see that with the non-zero manipulator stiffness conditions (C2 and C3) compared to zero stiffness (C1), tracking error, RMS_e , and control activity, RMS_u , decrease slightly, while GTO activity, σ_{GTO} (the

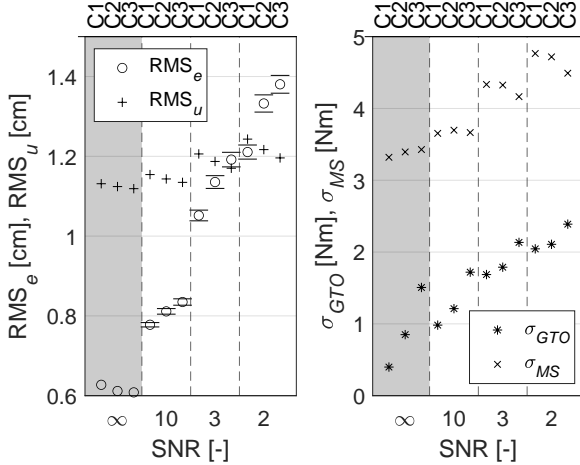


Fig. 12. Simulation results for C1 - C3 at various SNRs. The gray columns show results of one simulation per datapoint without remnant. The white columns show the averaged results of 1,000 remnant realizations. 95% confidence intervals are drawn for RMS_e . Values of RMS_u , σ_{GTO} and σ_{MS} from individual remnant realizations are distributed so close to their respective averages, that their confidence intervals cannot be visualized in this figure.

standard deviation of u_{GTO}), and MS activity, σ_{MS} (the standard deviation of u_{MS}), increase.

The same effects of the conditions on RMS_u and σ_{GTO} are found with Monte Carlo simulations where a remnant representation is added. However, the opposite effect on RMS_e is found. The effect on σ_{MS} also reverses but not as strongly.

These simulated results show a clear trend that GTO activity increases with manipulator stiffness. The effect of the manipulator stiffness on RMS_e depends on the addition of the remnant signal and effects on RMS_u and σ_{MS} are small.

The remnant SNR has a strong effect on the activity of GTO and MS. This is likely a result of adding the noise before the branches of the GTO and MS feedback loops, see Figure 9.

D. Apparatus

The same HMI experimental facility as described in Section II-C was used for this tracking task. In this experiment, the LCD only showed the controlled element position and the target position, but no preview of the target.

E. Procedure

The nine subjects that also performed the first experiment, performed all experiment runs in one session of less than one hour. Each subject performed one training run with condition C2. Each condition was then tested in five runs of the tracking task with five different realizations of the target signal. The five runs per condition were separated with breaks of 40 s. The three conditions were separated with breaks of 90 s. The order of the three conditions was mixed according to Table XII.

F. Metrics

The first two runs per condition are training runs and the last three are measurement runs referred to as r1, r2 and r3 with the forcing functions defined in Table VI. From the measured

TABLE XII
CONDITION ORDERING IN THE CONTROL TASK EXPERIMENT.

Subject	Training condition (one run)	First condition (five runs)	Second condition (five runs)	Third condition (five runs)
1	C2	C1	C2	C3
2	C2	C2	C3	C1
3	C2	C3	C1	C2
4	C2	C3	C2	C1
5	C2	C2	C1	C3
6	C2	C2	C3	C1
7	C2	C3	C1	C2
8	C2	C1	C3	C2
9	C2	C1	C3	C2

HO input, $u(t)$, and the controlled element position, $x(t)$, the following metrics were then calculated.

1) RMS_e : The root mean square of the error signal, i.e., the distance between $f_t(t)$ and $u(t)$, defines tracking performance.

2) RMS_u : The root mean square of the pilot input signal, $u(t)$, defines the control activity.

3) *Coherence*: The coherence, calculated with Eq. (14), measures the degree of linearity between a system's outputs and inputs. Its value is zero for a completely nonlinear system and one for a perfectly linear system. A high coherence between the input forcing function, $f_t(t)$, and the HO control actions, $u(t)$, justifies the use of quasi-linear pilot models such as the one considered in this paper. \tilde{S} indicates the average power-spectral density over the frequencies between two frequencies of $f_t(t)$. $\tilde{\omega}_{f_t}$ is the average of this band of frequencies. $f_t(t)$ consists of ten sines with frequencies ω_{f_t} allowing the coherence to be evaluated at the nine frequency bands, $\tilde{\omega}_{f_t}$ in-between frequencies ω_{f_t} . [6], [30]

$$\Gamma_{u,f_t}(\tilde{\omega}_t) = \sqrt{\frac{|\tilde{S}_{u,f_t}(\tilde{\omega}_{f_t})|^2}{\tilde{S}_{f_t,f_t}(\tilde{\omega}_t)\tilde{S}_{u,u}(\tilde{\omega}_t)}} \quad (14)$$

Verification of this method was performed by replacing $u(t)$ with a simulated signal obtained by passing $f_t(t)$ through an arbitrary linear filter. $\Gamma_{u,f_t}(\tilde{\omega}_t)$ then becomes equal to one at the nine frequency bands.

G. Human Operator Describing Function Estimation

The measured time traces are also used to estimate the human operator describing function in the frequency-domain.

1) *Phase Correction*: Because of the use of different realizations of the forcing functions, $u(t)$ cannot directly be averaged across the three realizations. For this to be possible, the components of $u(t)$ at the ten forcing frequencies with r1 and r2 were phase-shifted to r3. This phase-shift can be performed on $U(j\omega)$, the Fourier Transform of $u(t)$. Eq. (15) was applied at the ten positive and ten negative frequencies where $f_t(t)$ has power. The phase-shifted inputs, $u_s(t)$, are then found with the inverse Fourier Transform of $U_s(j\omega)$. These three time traces are then averaged to obtain the mean human operator input, $\tilde{u}(t)$. This is a variation of a method used in previous research on pilot identification [31].

$$\begin{aligned}
r1: & U_s(j\omega_t[i]) = U(j\omega_t[i])e^{j(\phi_3[i]-\phi_1[i])} \\
r2: & U_s(j\omega_t[i]) = U(j\omega_t[i])e^{j(\phi_3[i]-\phi_2[i])} \\
r3: & U_s(j\omega_t[i]) = U(j\omega_t[i])
\end{aligned} \tag{15}$$

The same operation is also used to obtain the average controlled element position, $\tilde{x}(t)$, and error signal, $\tilde{e}(t)$. With the Fourier Transforms of $f_t(t)$, $\tilde{u}(t)$ and $\tilde{e}(t)$, the estimated HO describing function, can be found with the instrumental variable method given by Eq. (16) [24].

$$\hat{H}_P(j\omega) = \frac{S_{u,f_t}(\omega_t)}{S_{e,f_t}(\omega_t)} \tag{16}$$

2) *Parameter Estimation Procedure:* In order to describe these dynamics with the model from Eq. (12), the distance in the complex plane between $\hat{H}_P(j\omega)$ and its modelled value with parameters Θ , $H_P(j\omega|\Theta)$, should be minimized at the ten forcing frequencies. The estimate of $\hat{H}_P(j\omega)$ is not equally precise at each of the ten forcing frequencies. In order to incorporate this knowledge, a maximum likelihood estimator (MLE) is used which is summarised in Eq. (17) [32]. This effectively minimizes the normalized distance in the complex plane. This normalized distance, D_i , is defined by the covariance matrix, Σ . Van Lunteren showed that the error in $H_P(j\omega)$ has an almost circular distribution in the complex plane [33]. Hence, Σ is chosen as a diagonal matrix with equal variances.

A working estimate of $\sigma_{H_P}^2[i]$ at each of the ten forcing frequencies is found by averaging the variance of the measured $\hat{H}_P(j\omega)$ at the six neighbouring (three lower and three higher) discrete frequencies. The maximum likelihood estimator reward function, Q_{MLE} , is calculated using the normalized complex distances. Eq. (17) defines the full procedure that is used for each participant at each condition to find the parameter vector, $\hat{\Theta}$, that best describes the measured response, $\hat{H}_P(j\omega)$. The parameters that make up Θ were selected

because these were found to be able to describe $\hat{H}_P(j\omega)$ well. As stated earlier, $T_L = 10$ s and is not included in Θ .

$$\begin{aligned}
\Theta &= [K_e \quad T_I \quad \tau_e \quad \omega_{nm}] \\
x_i &= [\text{Re}(H_P(j\omega_t[i]|\Theta)) \quad \text{Im}(H_P(j\omega_t[i]|\Theta))]^T \\
\mu_i &= [\text{Re}(\hat{H}_P(j\omega_t[i])) \quad \text{Im}(\hat{H}_P(j\omega_t[i]))]^T \\
\Sigma_i &= \begin{bmatrix} \sigma_{H_P}^2[i] & 0 \\ 0 & \sigma_{H_P}^2[i] \end{bmatrix} \\
D_i &= \frac{1}{2}(x_i - \mu_i)^T \Sigma_i^{-1} (x_i - \mu_i) \\
Q_{MLE} &= \frac{1}{N_f} \sum_{n=1}^{N_f} e^{-D_i} \\
\hat{\Theta} &= \underset{\Theta}{\text{argmax}} \quad Q_{MLE}
\end{aligned} \tag{17}$$

The found parameters, $\hat{\Theta}$, were then inserted in the model given in Figure 9 together with the constant parameters from Table VIII. This model was then numerically simulated to obtain time traces of the simulated control inputs, $u_{sim}(t)$ and internal feedback signals, $u_{GTO}(t)$ and $u_{MS}(t)$. The signals' standard deviations, $\sigma_{GTO}[\text{Nm}]$ and $\sigma_{MS}[\text{Nm}]$, then define the activity of the Golgi Tendon Organ and Muscle Spindles.

3) *Quality of fit:* When Q_{MLE} exactly equals one, the modelled frequency response, $H_P(j\omega)$, is identical to the measured response, $\hat{H}_P(j\omega)$, at each forcing frequency. Figure 13 shows one example of the modelled frequency response based on the measurements of one participant at one condition. A high MLE reward of 0.99 was achieved for these measured dynamics, reflected by small distances between the data and the model.

How well $H_P(j\omega)$ describes the time traces of the pilot inputs, $\tilde{u}(t)$, is then quantified with the Variance Accounted For, calculated with Eq. (18). This relates the measured and simulated discrete-time signals with N samples. VAFs were

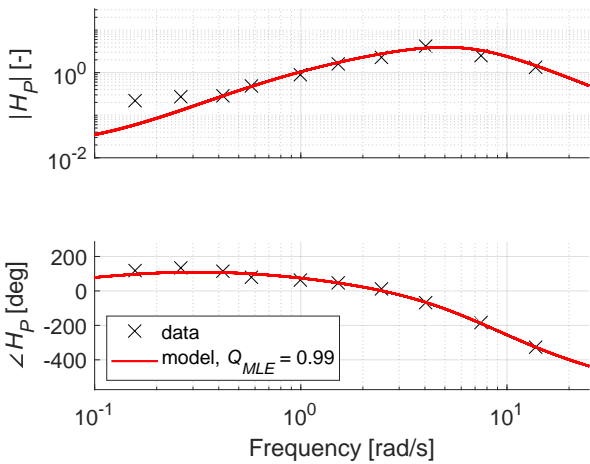


Fig. 13. Measured and fitted HO response of Participant 2 at C3.

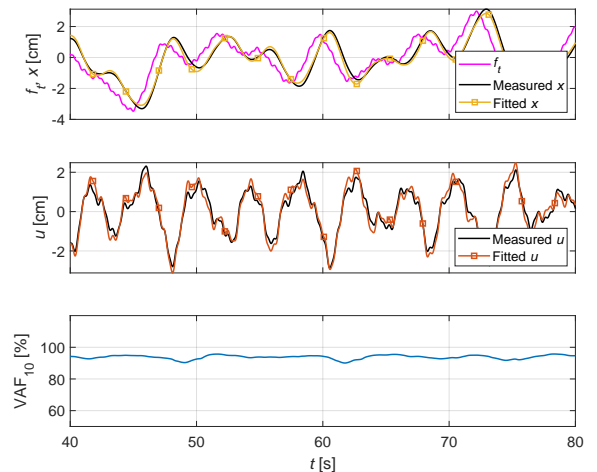


Fig. 14. Time traces of measured and simulated controlled element position and control inputs of Participant 2 at C3 (VAF = 94%).

calculated for the entire measurement time of each run. VAFs were also calculated at each point in the measurement time over the next ten seconds to obtain the time-windowed VAF, referred to as VAF₁₀. In Figure 14, the measured time traces and simulated time traces with the estimated parameters of one participant at one condition are compared. Plotted $u_{sim}(t)$ and $\tilde{u}(t)$ are fairly close together, reflected by VAF = 94 %.

$$\text{VAF} = \left(1 - \frac{\sum_{k=1}^N |u_{sim}(k) - \tilde{u}(k)|^2}{\sum_{k=1}^N \tilde{u}^2(k)} \right) \times 100 \% \quad (18)$$

H. Hypotheses

2a) *Higher RMS_e with C1*: With manipulator dynamics with zero stiffness, the human operator's tracking performance is expected to be worse. Here, no spring force in the manipulator is present that informs the HO about the position of the manipulator. A part of the numerical simulations supports this by showing worst tracking performance at this condition.

2b) *Reduced coherence with C1*: By the same reasoning, it is expected that HO's control actions are less linear with the target signal when the manipulator stiffness is zero.

2c) *Increased σ_{GTO} with increased manipulator stiffness*: The performed Monte Carlo simulations showed an increased GTO feedback signal power between the three conditions. This is expected to be true also for the experiment data.

I. Results

Upon examination of the tracking performance, RMS_e, and the coherence, $\Gamma_{u,ft}(\tilde{\omega}_t)$, it was decided to omit the measurements of two of the nine subjects from the results. The higher tracking errors and lower coherence of the control inputs indicated that these participants were not sufficiently able to control the DI dynamics. The results of the seven remaining subjects are presented.

Statistical analyses similar to those in Section II-G are performed to identify which observed effects are significant before examining the data more closely. For the statistical analysis of the coherence, the average of the nine coherence values of the frequency bands is used. Figure 15, each datapoint represents the average tracking error or control activity over the three measurement runs of one participant at one condition. Equally, each point in Figures 18 and 19 represents the processed results from the average of the measurement runs of one subject at one condition.

First, the normality of the data is assessed with a Shapiro-Wilk test reported in Table XIII. For normally distributed metrics, a one-way ANOVA between C1, C2 and C3 is conducted. If the ANOVA's result is significant, Bonferroni corrected pairwise comparisons of C1 and C2, C1 and C3 and between C2 and C3 are performed to distinguish if the effect between the three conditions is gradual or if the difference exists with one of the three conditions.

For non-normal data, the ANOVA is replaced with Friedman's test and Wilcoxon signed-rank tests are used to find between which specific conditions the difference exists.

TABLE XIII
SIGNIFICANCE p OF SHAPIRO-WILK NORMALITY TESTS OF TRACKING TASK METRICS. GRAY INDICATES THE METRICS THAT ARE CONCLUDED TO BE NON-NORMALLY DISTRIBUTED.

Metric	C1	C2	C3
RMS _e	0.932	0.444	0.833
RMS _u	0.175	0.460	0.127
$\Gamma_{u,ft}$	0.659	0.799	0.762
Q_{MLE}	0.014	0.002	0.005
VAF	0.575	0.047	0.116
K_e	0.865	0.371	0.174
T_I	0.842	0.623	0.712
ω_{nm}	0.843	0.877	0.985
τ_e	0.085	0.001	0.361
σ_{GTO}	0.025	0.014	0.353
σ_{MS}	0.245	0.004	0.111

TABLE XIV
ONE-WAY ANOVAS AND BONFERRONI CORRECTED PAIRWISE COMPARISONS OF TRACKING TASK METRICS. GREENHOUSE-GEISSER CORRECTED ANOVAS ARE INDICATED WITH (GG). SIGNIFICANT RESULTS HIGHLIGHTED IN GRAY.

Metric	ANOVA		Significance p of pairwise comparisons		
	$F(2,12)$	p	C1 and C2	C1 and C3	C2 and C3
RMS _e	8.282	0.005	0.040	0.025	1.000
RMS _u	2.099	0.165			
$\Gamma_{u,ft}$	13.833	0.001	0.019	0.011	0.775
VAF	1.506	0.261			
K_e (GG)	2.262	0.177			
T_I	0.671	0.529			
ω_{nm}	21.075	<0.001	0.010	0.001	0.239

TABLE XV
FRIEDMANN TESTS OF TRACKING TASK METRICS. SIGNIFICANT RESULTS HIGHLIGHTED IN GRAY.

Metric	$\chi^2(2)$	p
Q_{MLE}	0.286	0.867
τ_e	6.0	0.05
σ_{GTO}	14.0	0.001
σ_{MS}	6.0	0.05

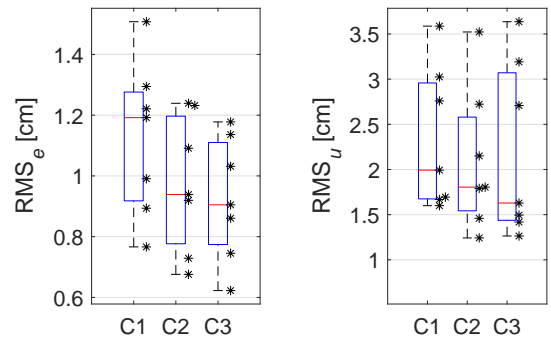


Fig. 15. Tracking error and control activity per condition. Each datapoint indicates the average over the three measurement runs of one participant.

1) *Tracking Performance and Control Activity and Linearity*: Figure 15 shows lower tracking error at conditions C2 and C3 than C1, confirming Hypothesis 2a. With zero manipulator stiffness, subjects' tracking performance was significantly worse but no significant effect was detected between the two non-zero stiffness conditions. No dependency of the control activity in terms of RMS_u on the three conditions is visible in Figure 15 and was confirmed by the ANOVA in Table XIV.

A clear effect on the degree of linearity of the HO's control actions in Figure 16 exists. The coherence of the pilot input signal with the target signal has values around 0.7 over the first six frequency bands. This is consistent with values found by Van Der El et al. for a pursuit tracking task with DI dynamics [6]. At the three highest frequency bands, where the amplitude of $f_t(t)$ is reduced, the coherence is considerably lower. This indicates that participants' control actions were less linear at these higher frequencies. This reduction of coherence coinciding with the bandwidth of the forcing function was not as clearly present in results that Van Der El et al. reported. The most likely cause for this difference is that our subjects were less skilled in performing a DI control task due to their natural ability or the limited amount of training they had.

The reduction of coherence at high frequencies can be attributed to the reduced amplitude of $f_t(t)$ at these frequencies. These small amplitudes become difficult for the HO to visually detect on the display, also because the order of magnitude is close to the resolution of the visual display.

The average coherence of all nine bands was significantly higher with C2 and C3, compared to C1. Hence, the non-zero stiffness of the manipulator caused the participants' control actions to be more linear with the target signal, agreeing with Hypothesis 2b. Figure 16 seems to show a difference between C2 and C3 as well, but this is insignificant, $p = 0.775$.

The absence of accurate GTO feedback with the zero stiffness manipulator is a possible explanation for the higher tracking error and lower coherence with C1. Without GTO feedback, HO control inputs are less accurate, i.e., contain more noise. This is reflected by larger tracking errors and lower coherence indicating a 'noisier' HO input spectrum.

2) *Human Operator DF Estimation*: The measured dynamics, $\hat{H}_P(j\omega)$, in Figure 17 at the three conditions coincide fairly well for the first eight forcing frequencies. At the highest two frequencies, a higher magnitude with C3 compared to C1 of approximately 5 dB was found. This is opposite to the isolated effect of the manipulator dynamics shown in Figure 11. Hence, HOs adjust their dynamics such that the manipulator dynamics are compensated for and the high-frequency response even increases.

The longer error-bars at the highest two frequencies indicate that, between participants, larger variations of the measured dynamics exist here. This is consistent with the lower coherence at these frequencies (Figure 16). Control behavior at high frequencies was overall less linear with the target signal, leading to larger variations of the measured linear $\hat{H}_P(j\omega)$.

The estimated parameters in Figure 18 show how the HO adapts to changing manipulator dynamics. The values

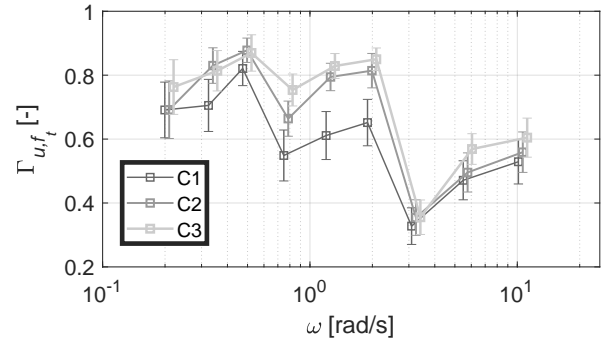


Fig. 16. Coherence between $u(t)$ and $f_t(t)$ at nine frequency bands between the ten forcing frequencies per condition with 95 % confidence error-bars.

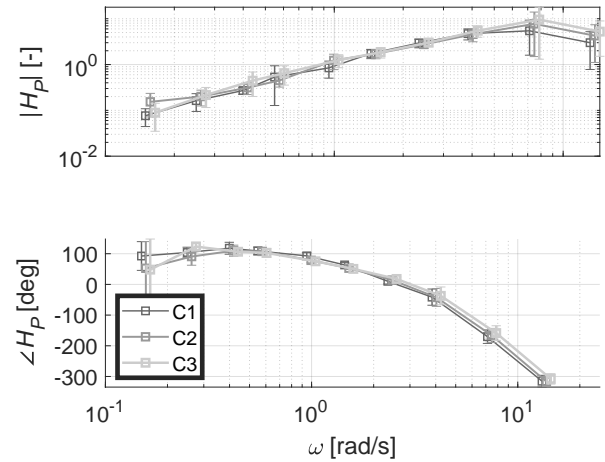


Fig. 17. Measured HO dynamics of all participants per condition with 95 % confidence error-bars.

of Q_{MLE} and VAF show that the used method describes the estimated dynamics, $\hat{H}_P(j\omega)$, equally well between the conditions. The model parameters are consistent with the expectations stated in Section III-B and when compared to previously reported values [6], [34].

The most significant trend in the parameters is that, on average, ω_{nm} is significantly larger with C2 and C3 than C1, agreeing with the trend in Table XI. The difference between C2 and C3 is insignificant. As expected, the magnitude of ω_{nm} is smaller than values found earlier when modelling $H_P(j\omega)$ without GTO and MS feedback loops [7]. The feedback loops add some neuromuscular stiffness to the stiffness represented by ω_{nm} . Hence, when GTO and MS feedback are included, modelled values of ω_{nm} are lower since it is no longer the only contributing factor to the neuromuscular stiffness.

No significant effect on T_I was shown between the conditions. τ_e seems to be slightly lower with C1 compared to C2 and C3 but this effect was on the limit of significance. A Wilcoxon signed-rank test of τ_e between C1 and C2 was significant, $Z = -2.366$, $p = 0.018$.

σ_{GTO} increases significantly between the three conditions

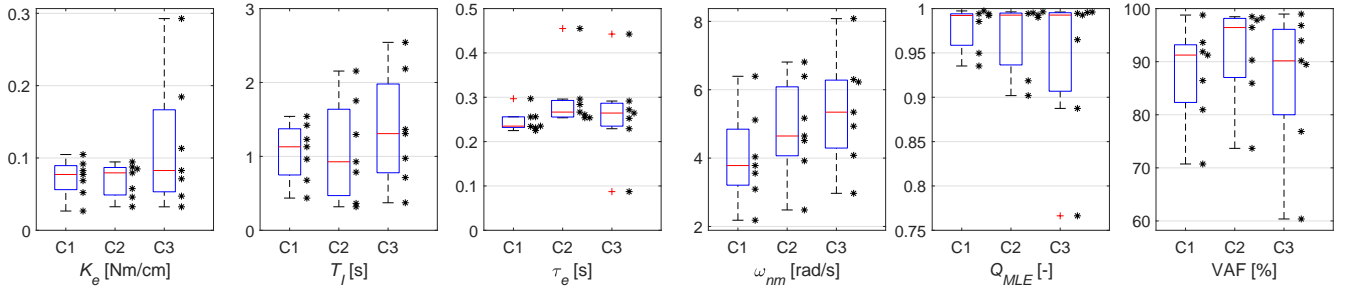


Fig. 18. Parameter estimation results per condition. Estimated parameter vector $\hat{\Theta} = [K_e \ T_I \ \tau_e \ \omega_{nm}]$ and the quality of fit in the frequency-domain, Q_{MLE} , and in the time-domain, VAF.

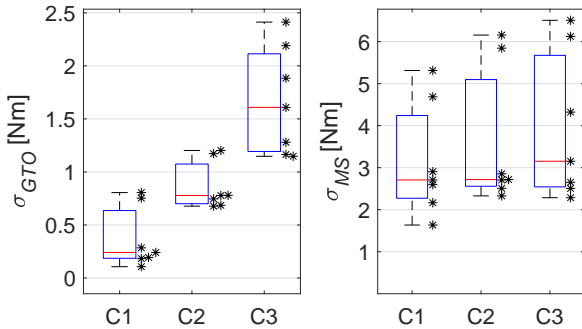


Fig. 19. Theoretical GTO and MS activity per condition from numerically simulating the control task with estimated parameters Figure 18. Values of σ_{GTO} are close to the simulations at $SNR = \infty$, see Figure 12. σ_{MS} values are slightly lower than simulations at all SNRs.

in Figure 19, agreeing with Hypothesis 2c. Hence, the Golgi Tendon Organ becomes more active with higher manipulator stiffness in the control task. Muscle Spindle activity, σ_{MS} , also seems to be slightly lower with C1 than with C2. A Wilcoxon signed-rank test confirmed this, $Z = -1.690$, $p = 0.091$.

The trends of σ_{GTO} and σ_{MS} between C1-C3 agree with the simulations, see Figure 12. Though, σ_{GTO} and σ_{MS} are slightly lower across all conditions compared to simulations.

The results with respect to σ_{GTO} and σ_{MS} have to be interpreted with care since they result from a parameter estimation followed by a numerical simulation. These procedures were documented and carried out carefully but are still not as conclusive as direct measurements would be.

J. Discussion

Numerical simulations without added remnant ($SNR = \infty$) showed lower tracking error, RMS_e , with increased manipulator stiffness, but with added remnant, RMS_e increased with manipulator stiffness, see Figure 12. The trend between the three conditions in Figure 15 agrees with the simulated result without adding remnant. However, the measured tracking error was overall closer to the simulation scenario with $SNR = 2$.

Because of the DI controlled element, tracking error was rather high and varied considerably between participants. We have to conclude that with this difficult to control CE, subjects' skill level of performing a control task is an important factor.

In the experiment, a significant increase of the tracking error with C1 was found, indicating that zero spring stiffness is an unfavourable manipulator configuration. The lower HO input coherence at C1 (Figure 16) supports this by demonstrating that control actions were less linear with the target signal.

The magnitude of the measured coherence suggests that in the present control task, a part of the pilot inputs cannot be described with quasi-linear models and that the manipulator configuration has an effect on the magnitude of this non-linear part. This knowledge can be used in the formulation of an adequate remnant model if we assume that high coherence is equivalent to a high signal to noise ratio. Present research demonstrated a dependency of the coherence on the manipulator dynamics and previous research illustrated how the coherence changes with the CE dynamics [6]. Future research could be performed to provide a more detailed map of the coherence of the HO inputs across different task variables, i.e., the controlled element, manipulator and display type. This could then be used to come up with a better definition of a remnant model where the signal to noise ratio and possibly the spectrum of the noise signal depend on the task variables.

The method of simulating the control task and its results with respect to the remnant SNR in Section III-C could be used as a framework for evaluating such a remnant model. The formulation of a model of pilot remnant remains an important problem in pilot identification.

The achieved VAFs with the estimated parameters are reasonably high, which is consistent with other work where the time-domain measurements were averaged before analysis in the frequency-domain [7]. The reported VAFs show that for the conducted experiment, it was justified to assume that subjects only looked at the error signal and that a multi-channel model was not needed. Higher VAFs might be attainable with a multi-channel method but the single-channel model has satisfactory performance for this research's purposes.

With the estimated parameters, it was validated that the theoretical GTO activity increases with the manipulator stiffness where a considerably smaller increase of MS activity was present and no change of the control activity was observed. Also, an increase of ω_{nm} with manipulator stiffness was found. These effects are to be expected considering that the used HO model includes the varying manipulator dynamics and should

therefore only be considered as validation that increased manipulator stiffness increases the *theoretical* GTO activity. Previous research does show that more precise knowledge of muscle activity is attainable using electromyography [35], but this is still no direct measurement of GTO and MS activity.

The conditions with higher theoretical GTO activity compared to MS showed better tracking performance and linearity. This improvement could be attributed to the demonstrated better accuracy of GTO compared to MS in Section II. However, with the manipulator conditions, we merely showed a correlation between the activity of GTO and the tracking performance. This does not imply a causal relationship. The changing performance between the conditions could, for example, have been caused by the higher stiffness manipulators automatically moving back to the center. This could be a cause for better performance which is not directly related to GTO or MS. Still, it is plausible that the found accuracy of GTO plays an important role. Increasing the importance of GTO in a manual control task without having this confound of different manipulator dynamics is more complicated. One could think of a way to make position sensing in the control task worthless by adding a form of disturbance to the position of the manipulator.

Not all metrics were shown to be significantly dependent on the used conditions. Significant effects were only found when C1 was compared to C2 or C3. Only σ_{GTO} was significantly different between C2 and C3 too. If a future experiment would be conducted to find the manipulator dynamics that result in the best tracking performance, a higher number of participants or more measurements per participant and more training would be beneficial to the statistical power of the results. On the other hand, the used number of participants in present research was sufficient to clearly distinguish the effects between zero and non-zero manipulator stiffness.

IV. CORRELATION BETWEEN JND EXPERIMENT AND TRACKING TASK METRICS

Each subject's JND-ratio, X_{JND} , denotes how much higher stiffness JND at all force conditions, W_K^F , (where stiffness discrimination is based on position difference) was, compared to position conditions, W_K^P (where stiffness discrimination is based on force difference). For instance, $X_{JND} = 100\%$ when the subject's stiffness JND in force conditions was exactly twice the stiffness JND in position conditions meaning that force sensing was twice as accurate as position sensing.

$$X_{JND} = \frac{W_K^F - W_K^P}{W_K^P} \times 100\% \quad (19)$$

Relative changes in tracking task metrics with the zero stiffness manipulator (C1) compared to the average of the two non-zero stiffness manipulators (C2 and C3) are calculated for each participant. For example, $Y_{RMS_e} = 10\%$ means a subject had 10% higher tracking error at C1 than C2 and C3.

$$Y_{RMS_e} = \frac{RMS_e^{C1} - \tilde{RMS}_e^{C2,C3}}{\tilde{RMS}_e^{C2,C3}} \times 100\% \quad (20)$$

Changes in control activity, Y_{RMS_u} , and HO input coherence, Y_Γ , are calculated in the same way.

We expect to see large absolute values of Y_{RMS_e} and Y_Γ for subjects with high JND-ratio. This would mean that subjects with higher difference in position and force perception accuracy have more benefit from a non-zero stiffness manipulator.

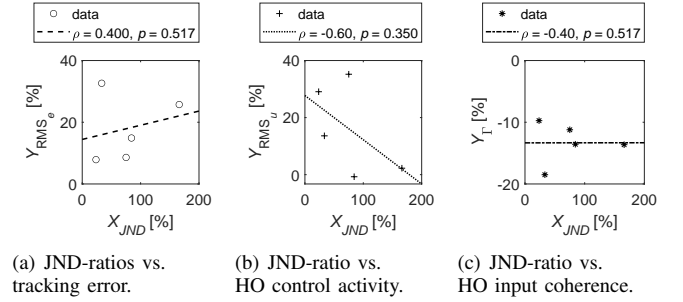


Fig. 20. Correlation between JND-ratios in the first experiment and changes in control behavior between zero and non-zero stiffness manipulator in the second experiment. Each datapoint represents one participant's results from the stiffness JND experiment and the control task.

Figure 20 examines the existence of a correlation between X_{JND} , measured in the first experiment, and changes in metrics measured in the second experiment, Y_{RMS_e} , Y_{RMS_u} and Y_Γ . Of the seven participants whose tracking task results were discussed in Section III, one did not perform the JND experiment and an outlier with $X_{JND} \approx 700\%$ was removed. Hence, only five subjects remain for this correlation analysis.

Note that Y_{RMS_e} and all except one datapoint of Y_{RMS_u} are positive, showing that each subject had relatively higher tracking error with C1 compared to C2 and C3 and all except one subject had higher control activity with C1 than with C2 and C3. Y_Γ is consistently negative since each participant performed control actions with a higher degree of linearity with C2 and C3 compared to the coherence measured at C1.

Spearman's rank correlation significance $p > 0.05$ between X_{JND} , and Y_{RMS_e} , Y_{RMS_u} or Y_Γ was found so no significant relation between these data exists. Only Figure 20(a) shows a weak trend that subjects with higher JND ratio have greater tracking performance improvement from a zero to non-zero stiffness manipulator. This is promising but insignificant. A future experiment with more participants that received more training with the DI CE, may confirm the trend that subjects with a larger accuracy difference of position and force perception have more benefit of a non-zero stiffness manipulator.

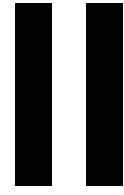
V. CONCLUSION

The first experiment confirmed that just noticeable differences of force are two times smaller than just noticeable differences of position in an experiment of discriminating side-stick manipulator stiffness. This is related to better Golgi Tendon Organ accuracy compared to Muscle Spindles. Weber's law appears to be applicable at four used conditions defined by the reference stiffness and target deflection. A human operator model including neuromuscular dynamics in a manual control

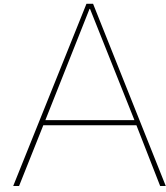
task, showed increasing theoretical GTO activity with increasing manipulator stiffness. A pursuit tracking task with zero and non-zero manipulator stiffness conditions, showed that zero stiffness leads to worse tracking performance and reduced linearity of the human operator's control inputs. Therefore, a correlation between the activity of GTO and better tracking performance exists. A method to relate specific subjects proprioceptive qualities measured in the first experiment to their control behavior in the second was proposed, but showed no significant results yet.

REFERENCES

- [1] R. Granit, "The functional role of the muscle spindles-facts and hypotheses," *Brain*, vol. 98, no. 4, pp. 531–556, 1975.
- [2] E. de Vlugt, A. C. Schouten, and F. C. T. van der Helm, "Adaptation of reflexive feedback during arm posture to different environments," *Biol. Cyb.*, vol. 87, pp. 10–26, 2002.
- [3] W. Fu, "Evidence-based development and evaluation of haptic interfaces for manual control," Ph.D. dissertation, Delft University of Technology, Faculty of Aerospace Engineering, June 2019.
- [4] J. Smisek, E. Sunil, M. M. van Paassen, D. A. Abbink, and M. Mulder, "Neuromuscular-system-based tuning of a haptic shared control interface for UAV teleoperation," *IEEE Trans. Human-Mach. Syst.* vol. 47 no. 4, pp. 449–461, 2017.
- [5] M. Mulder, D. M. Pool, D. A. Abbink, E. R. Boer, P. M. T. Zaal, F. M. Drop, K. van der El, and M. M. van Paassen, "Manual Control Cybernetics: State-of-the-Art and Current Trends," *IEEE Transactions on Human-Machine Systems*, vol. 48, no. 5, pp. 468–485, 2018.
- [6] K. van Der El, D. M. Pool, H. J. Damveld, M. M. van Paassen, and M. Mulder, "An empirical human controller model for preview tracking tasks," *IEEE Transactions on Cybernetics*, vol. 46, no. 10, oct 2015.
- [7] V. A. Laurens, D. M. Pool, H. J. Damveld, M. M. van Paassen, and M. Mulder, "Effects of Controlled Element Dynamics on Human Feedforward Behavior in Ramp-Tracking Tasks," *IEEE Trans. Cybernetics*, vol. 45, no. 2, pp. 253–265, Feb. 2015.
- [8] A. van Grootheest, D. M. Pool, M. M. van Paassen, and M. Mulder, "Identification of Time-Varying Manual Control Adaptations with Recursive ARX Models," *2018 AIAA Modeling and Simulation Technologies Conference*, 2018.
- [9] F. M. Nieuwenhuizen, P. M. T. Zaal, M. Mulder, M. M. van Paassen, and J. A. Mulder, "Modeling Human Multichannel Perception and Control Using Linear Time-Invariant Models," *Journal of Guidance, Control, and Dynamics*, vol. 31, no. 4, pp. 999–1013, 2008.
- [10] M. S. Raghu Prasad, S. Purswani, and M. Manivannan, "Force JND for Right Index Finger Using Contra Lateral Force Matching Paradigm," *Lecture Notes in Mechanical Engineering*, pp. 365–375, 2013.
- [11] S. Allin, Y. Matsuoka, and R. Klatzky, "Measuring just noticeable differences for haptic force feedback: implications for rehabilitation," *Proceedings 10th Symposium on Haptic Interfaces for Virtual Environment and Teleoperator Systems. HAPTICS 2002*.
- [12] H. E. Ross and E. E. Brodie, "Weber fractions for weight and mass as a function of stimulus intensity," *The Quarterly Journal of Experimental Psychology Section A*, vol. 39, no. 1, pp. 77–88, 1987.
- [13] N. I. Durlach, L. A. Delhorne, A. Wong, W. Y. Ko, W. M. Rabinowitz, and J. Hollerbach, "Manual discrimination and identification of length by the finger-span method," *Percept. Psychophys.*, vol. 46, pp. 29–38, 1989.
- [14] M. O. Ernst and M. S. Banks, "Humans integrate visual and haptic information in a statistically optimal fashion," *Nature*, vol. 415, pp. 429–433, 2002.
- [15] B. R. Brewer, M. Fagan, R. L. Klatzky, and Y. Matsuoka, "Perceptual Limits for a Robotic Rehabilitation Environment Using Visual Feedback Distortion," *IEEE Transactions on Neural Systems and Rehabilitation Engineering*, vol. 13, no. 1, pp. 1–11, 2005.
- [16] H. J. Damveld, D. A. Abbink, M. Mulder, M. M. van Paassen, F. C. T. van der Helm, and R. J. A. W. Hosman, "Identification of the Feedback Components of the Neuromuscular System in a Pitch Control Task," *AIAA Modeling and Simulation Technologies Conference*, 2010.
- [17] R. J. A. W. Hosman, and J. C. van der Vaart, "Active and Passive side-stick Controllers: Tracking Task Performance and Pilot Control Behavior," *Proceedings of the AGARD Conference on the Man-Machine Interface in Tactical Aircraft Design and Combat Automation*, Vol. AGARD-C8-424, Stuttgart, Germany, 1988, pp. 26–1 – 26–11.
- [18] H. Z. Tan, N. I. Durlach, G. L. Beauregard, and M. A. Srinivasan, "Manual discrimination of compliance using active pinch grasp: The roles of force and work cues," *Perception & Psychophysics*, vol. 57, no. 4, pp. 495–510, 1995.
- [19] J. Venrooij, D. A. Abbink, M. Mulder, M. M. van Paassen, M. Mulder, F. C. T. van der Helm, and H. H. Bülthoff, "A Biodynamic Feedthrough Model Based on Neuromuscular Principles," *IEEE Transactions on Cybernetics*, vol. 44, no. 7, pp. 1141–1154, 2014.
- [20] M. A. García-Pérez, "Forced-choice staircases with fixed step sizes: Asymptotic and small-sample properties," *Vision Research*, vol. 38, no. 12, pp. 1861–1881, 1998.
- [21] J. V. Bradley, "Complete Counterbalancing of Immediate Sequential Effects in a Latin Square Design," *Journal of the American Statistical Association*, vol. 53, no. 282, pp. 525–528, 1958.
- [22] L. A. Jones and I. W. Hunter, "A perceptual analysis of stiffness," *Experimental Brain Research*, vol. 79, no. 1, pp. 150–156, 1990.
- [23] D. T. McRuer and H. R. Jex, "A review of quasi-linear pilot models," *IEEE Transactions on Human Factors in Electronics*, vol. HFE-8, no. 3, pp. 231–249, 1967.
- [24] D. T. McRuer, D. Graham, E. S. Krendel, and W. J. Reisener, "Human Pilot Dynamics in Compensatory Systems, Theory Models and Experiments with Controlled Element and Forcing Function Variations," Air Force Flight Dynamics Laboratory, Wright-Patterson Air Force Base, OH, Tech. Rep. AFFDL-TR-65-15, 1965.
- [25] H. J. Damveld, G. C. Beerens, M. M. van Paassen, and M. Mulder, "Design of Forcing Functions for the Identification of Human Control Behavior," *Journal of Guidance, Control, and Dynamics*, vol. 33, no. 4, pp. 1064–1081, 2010.
- [26] H. J. Damveld, "A Cybernetic Approach to Assess the Longitudinal Handling Qualities of Aeroelastic Aircraft," Ph.D. dissertation, Delft University of Technology, Faculty of Aerospace Engineering, May 2009.
- [27] J. Lasschuit, M. Lam, M. Mulder, M. M. van Paassen, and D. A. Abbink, "Measuring and Modeling Neuromuscular System Dynamics for Haptic Interface Design," *AIAA Modeling and Simulation Technologies Conference and Exhibit*, 2008.
- [28] D. M. Pool, P. M. T. Zaal, H. J. Damveld, M. M. van Paassen, and M. Mulder, "Pilot equalization in manual control of aircraft dynamics," *2009 IEEE International Conference on Systems, Man and Cybernetics*, 2009.
- [29] K. van der El, D. M. Pool, M. M. van Paassen, and M. Mulder, "Effects of Target Trajectory Bandwidth on Manual Control Behavior in Pursuit and Preview Tracking," *IEEE Transactions on Human-Machine Systems*, vol. 50, no. 1, pp. 68–78, 2020.
- [30] L. Ljung, *System Identification Theory for the User*, 2nd ed. Upper Saddle River, NJ: Prentice Hall, Inc., 1999.
- [31] W. J. Kaljouw, M. Mulder, and M. M. van Paassen, "Multi-loop Identification of Pilot's Use of Central and Peripheral Visual Cues," *AIAA Modeling and Simulation Technologies Conference and Exhibit*, 2004.
- [32] P. M. T. Zaal, D. M. Pool, Q. P. Chu, M. M. van Paassen, M. Mulder, and J. A. Mulder, "Modeling Human Multimodal Perception and Control Using Genetic Maximum Likelihood Estimation," *Journal of Guidance, Control, and Dynamics*, vol. 32, no. 4, pp. 1089–1099, 2009.
- [33] A. van Lunteren, "Identification of Human Operator Describing Function Models with One or Two Inputs in Closed Loop Systems," Ph.D. dissertation, Delft University of Technology, Faculty of Mechanical Engineering, March 1979.
- [34] F. M. Drop, D. M. Pool, H. J. Damveld, M. M. van Paassen, and M. Mulder, "Identification of the Feedforward Component in Manual Control With Predictable Target Signals," *IEEE Trans. Cybernetics*, vol. 43, no. 6, pp. 1936–1949, Dec. 2013.
- [35] M. M. van Paassen, "Biophysics in Aircraft Control", Ph.D. dissertation, Delft University of Technology, Faculty of Aerospace Engineering, June 1994.



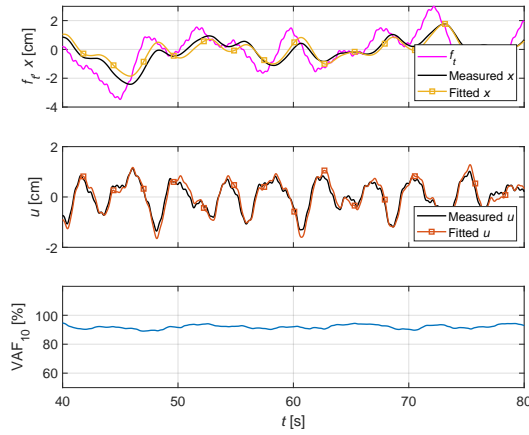
Research Appendices



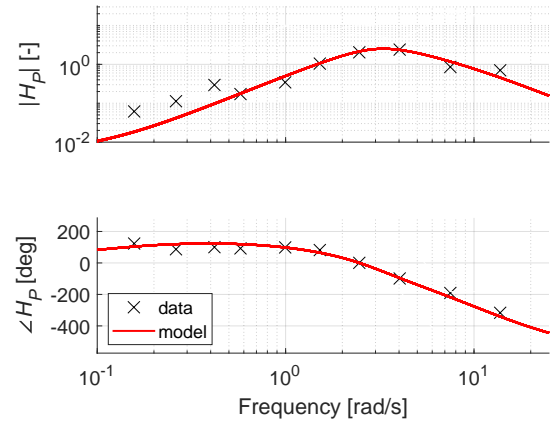
Individual Subjects' Tracking Task Results

The results of each participant's measurement runs are documented here. Per subject, C1 and C3 are presented graphically and all three condition's results are summarized in a table.

A.1. Subject 1

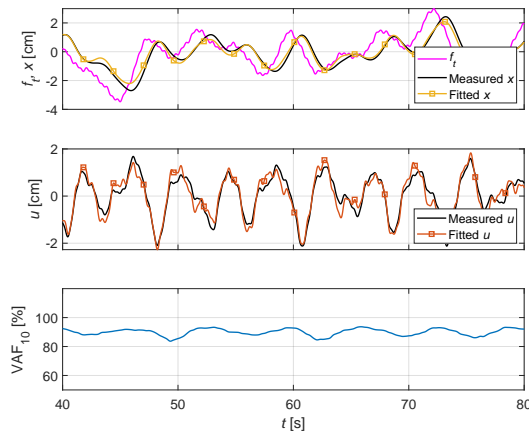


(a) CE position, x , and HO input, u time-traces of subject 1 at C1.

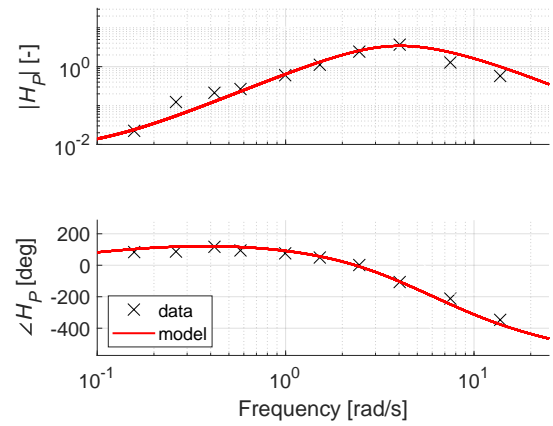


(b) Frequency response of subject 1 at C1.

Figure A.1: Measured and fitted results of subject 1 at C1.



(a) CE position, x , and HO input, u time-traces of subject 1 at C3.



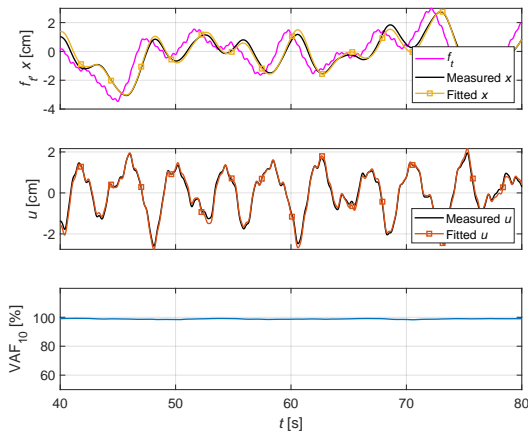
(b) Frequency response of subject 1 at C3.

Figure A.2: Measured and fitted results of subject 1 at C3.

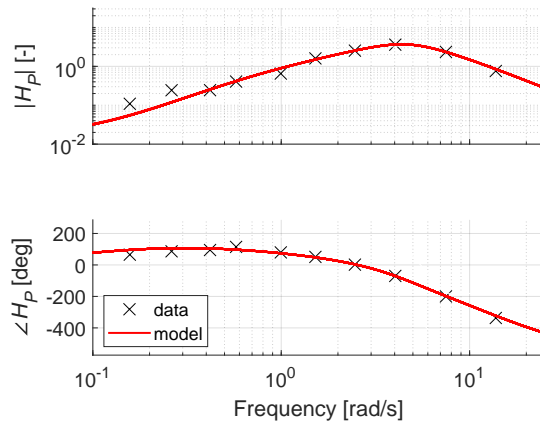
Table A.1: Summary of measured results and estimated parameters of subject 1 at all conditions.

	RMS_e [cm]	RMS_u [cm]	Γ_{u,f_t} [-]	K_e [N m cm ⁻¹]	T_I [s]	τ_e [s]	ω_{nm} [rad s ⁻¹]	Q_{MLE} [-]	VAF [%]
C1	1.508	1.668	0.434	0.027	0.436	0.297	2.18	0.994	91.86
C2	1.239	1.791	0.595	0.033	0.318	0.455	2.48	0.994	90.28
C3	1.178	1.495	0.629	0.032	0.373	0.443	2.97	0.995	90.16

A.2. Subject 2

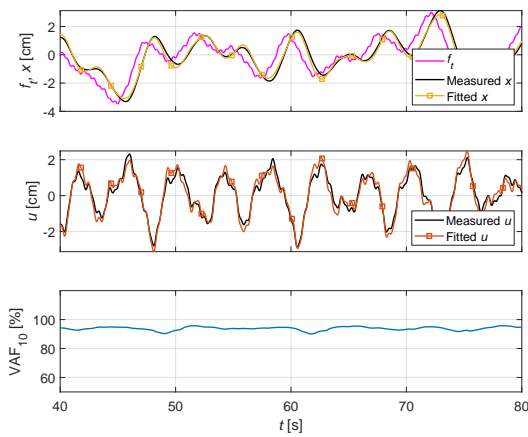


(a) CE position, x , and HO input, u time-traces of subject 2 at C1.

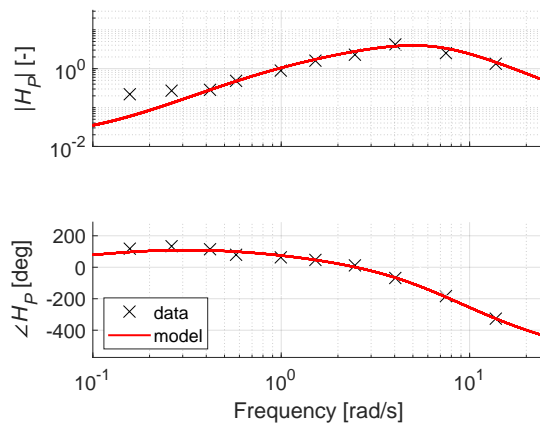


(b) Frequency response of subject 2 at C1.

Figure A.3: Measured and fitted results of subject 2 at C1.



(a) CE position, x , and HO input, u time-traces of subject 2 at C3.



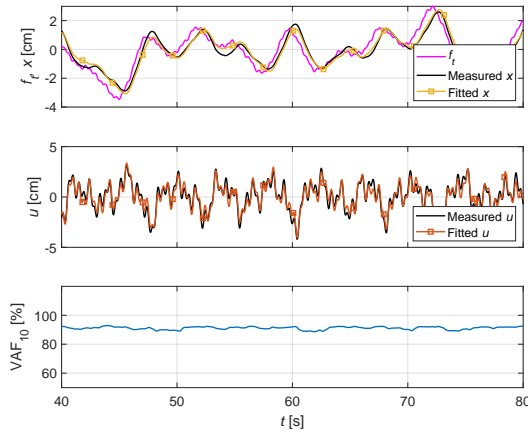
(b) Frequency response of subject 2 at C3.

Figure A.4: Measured and fitted results of subject 2 at C3.

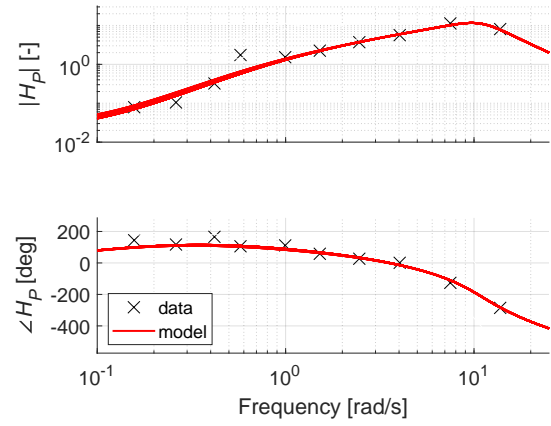
Table A.2: Summary of measured results and estimated parameters of subject 2 at all conditions.

	RMS_e [cm]	RMS_u [cm]	Γ_{u,f_t} [-]	K_e [N m cm ⁻¹]	T_I [s]	τ_e [s]	ω_{nm} [rad s ⁻¹]	Q_{MLE} [-]	VAF [%]
C1	1.221	1.993	0.612	0.083	1.541	0.256	3.09	0.997	98.78
C2	1.232	1.460	0.651	0.088	2.155	0.267	3.92	0.995	98.47
C3	1.032	1.629	0.706	0.083	1.308	0.292	4.08	0.993	93.93

A.3. Subject 3

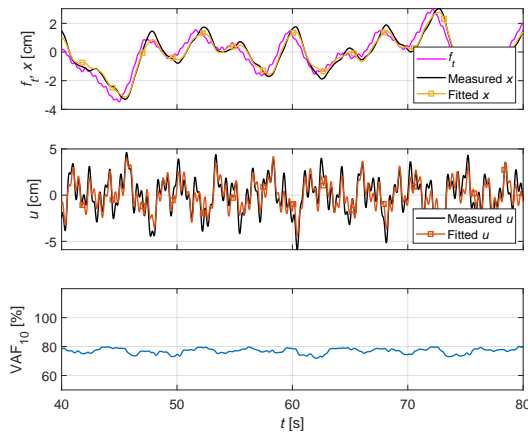


(a) CE position, x , and HO input, u time-traces of subject 3 at C1.

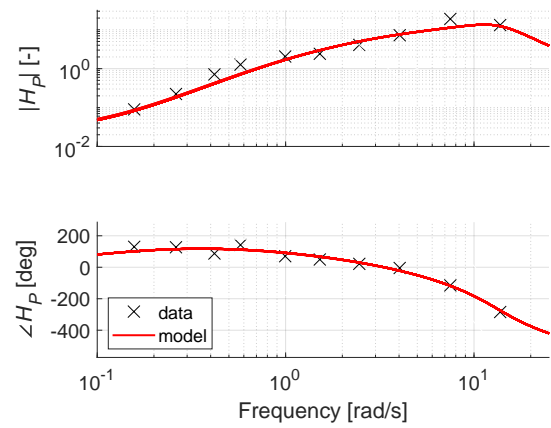


(b) Frequency response of subject 3 at C1.

Figure A.5: Measured and fitted results of subject 3 at C1.



(a) CE position, x , and HO input, u time-traces of subject 3 at C3.



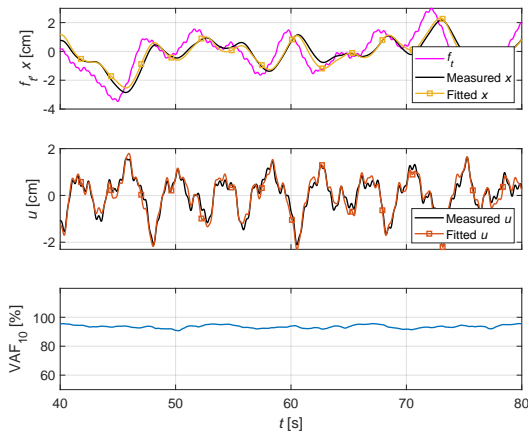
(b) Frequency response of subject 3 at C3.

Figure A.6: Measured and fitted results of subject 3 at C3.

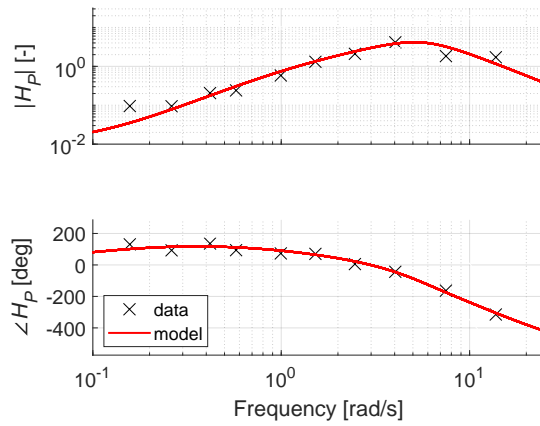
Table A.3: Summary of measured results and estimated parameters of subject 3 at all conditions.

	RMS_e [cm]	RMS_u [cm]	Γ_{u,f_t} [-]	K_e [N m cm ⁻¹]	T_I [s]	τ_e [s]	ω_{nm} [rad s ⁻¹]	Q_{MLE} [-]	VAF [%]
C1	0.894	3.024	0.648	0.105	1.231	0.234	6.39	0.935	91.24
C2	0.676	2.723	0.732	0.046	0.364	0.296	6.81	0.902	85.93
C3	0.746	3.191	0.769	0.113	0.974	0.272	8.08	0.887	76.85

A.4. Subject 4

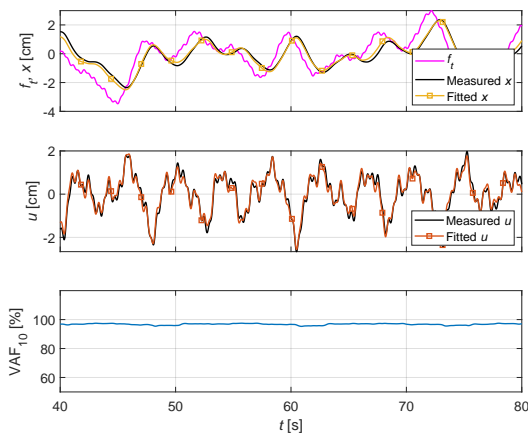


(a) CE position, x , and HO input, u time-traces of subject 4 at C1.

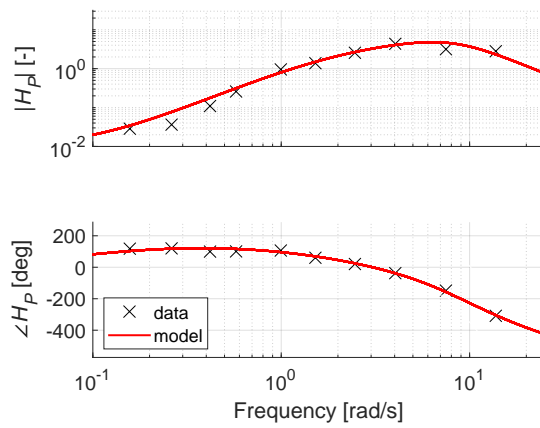


(b) Frequency response of subject 4 at C1.

Figure A.7: Measured and fitted results of subject 4 at C1.



(a) CE position, x , and HO input, u time-traces of subject 4 at C3.



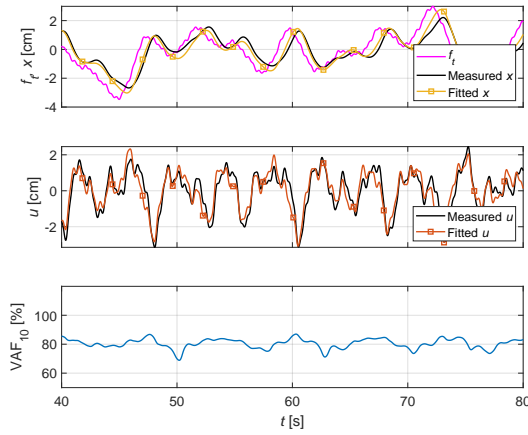
(b) Frequency response of subject 4 at C3.

Figure A.8: Measured and fitted results of subject 4 at C3.

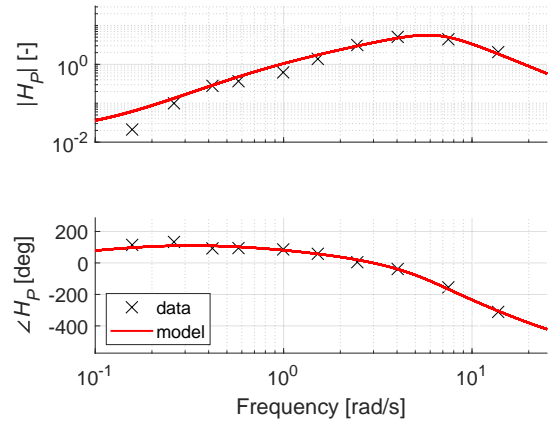
Table A.4: Summary of measured results and estimated parameters of subject 4 at all conditions.

	RMS_e [cm]	RMS_u [cm]	Γ_{u,f_t} [-]	K_e [N m cm ⁻¹]	T_I [s]	τ_e [s]	ω_{nm} [rad s ⁻¹]	Q_{MLE} [-]	VAF [%]
C1	1.192	1.600	0.572	0.052	0.963	0.231	3.56	0.994	93.62
C2	0.939	1.805	0.666	0.058	0.927	0.261	5.17	0.993	96.43
C3	1.136	1.418	0.657	0.047	0.713	0.264	4.93	0.996	96.81

A.5. Subject 5

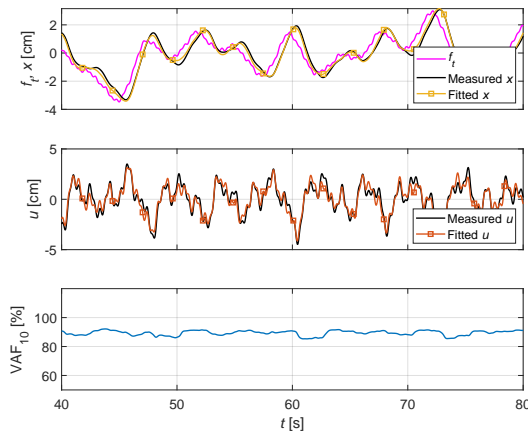


(a) CE position, x , and HO input, u time-traces of subject 5 at C1.

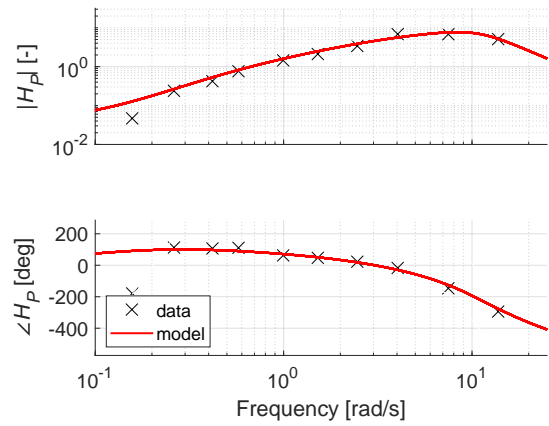


(b) Frequency response of subject 5 at C1.

Figure A.9: Measured and fitted results of subject 5 at C1.



(a) CE position, x , and HO input, u time-traces of subject 5 at C3.



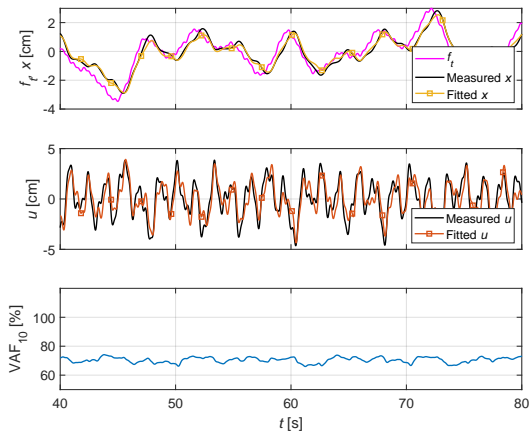
(b) Frequency response of subject 5 at C3.

Figure A.10: Measured and fitted results of subject 5 at C3.

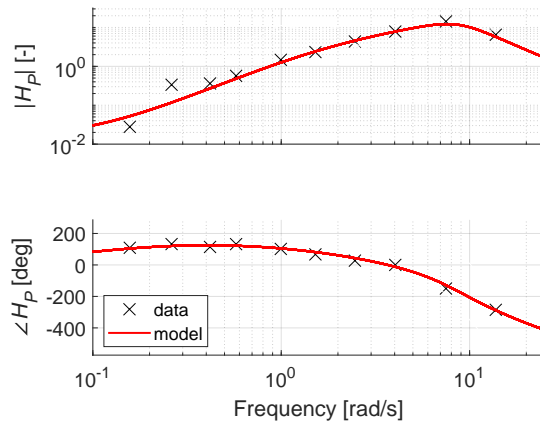
Table A.5: Summary of measured results and estimated parameters of subject 5 at all conditions.

	RMS_e [cm]	RMS_u [cm]	Γ_{u,f_t} [-]	K_e [N m cm ⁻¹]	T_I [s]	τ_e [s]	ω_{nm} [rad s ⁻¹]	Q_{MLE} [-]	VAF [%]
C1	1.294	2.759	0.545	0.092	1.421	0.235	4.04	0.992	80.95
C2	1.091	2.151	0.623	0.079	1.296	0.254	4.65	0.996	97.82
C3	0.861	2.707	0.715	0.184	2.184	0.229	6.30	0.965	89.46

A.6. Subject 6

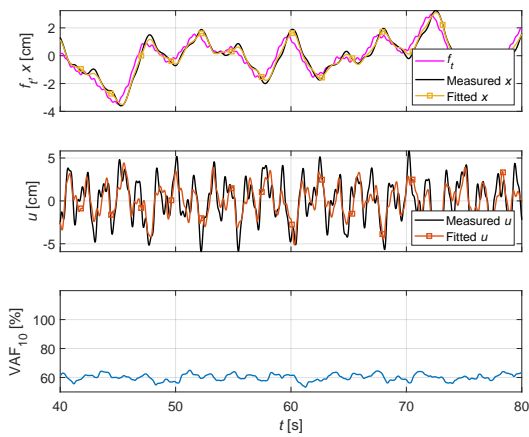


(a) CE position, x , and HO input, u time-traces of subject 6 at C1.

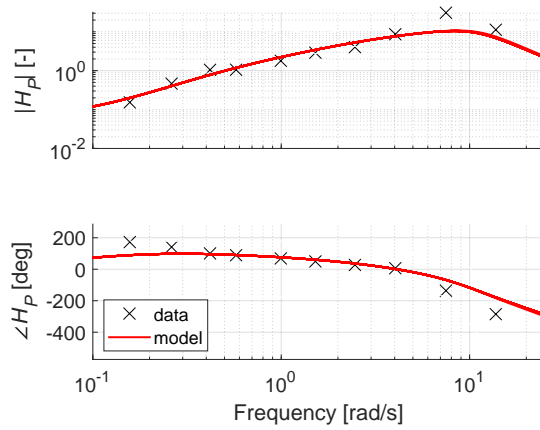


(b) Frequency response of subject 6 at C1.

Figure A.11: Measured and fitted results of subject 6 at C1.



(a) CE position, x , and HO input, u time-traces of subject 6 at C3.



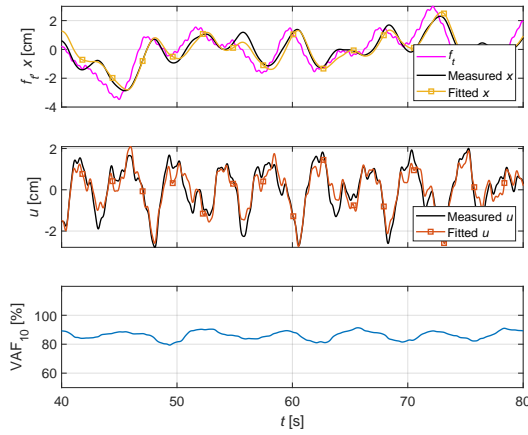
(b) Frequency response of subject 6 at C3.

Figure A.12: Measured and fitted results of subject 6 at C3.

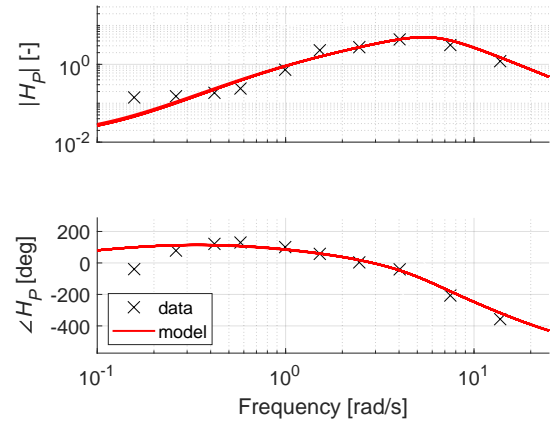
Table A.6: Summary of measured results and estimated parameters of subject 6 at all conditions.

	RMS_e [cm]	RMS_u [cm]	Γ_{u,f_t} [-]	K_e [N m cm ⁻¹]	T_I [s]	τ_e [s]	ω_{nm} [rad s ⁻¹]	Q_{MLE} [-]	VAF [%]
C1	0.766	3.587	0.700	0.077	0.677	0.225	5.12	0.950	70.73
C2	0.729	3.522	0.712	0.095	0.787	0.254	6.39	0.919	73.67
C3	0.623	3.636	0.783	0.293	2.543	0.087	6.23	0.766	60.37

A.7. Subject 7

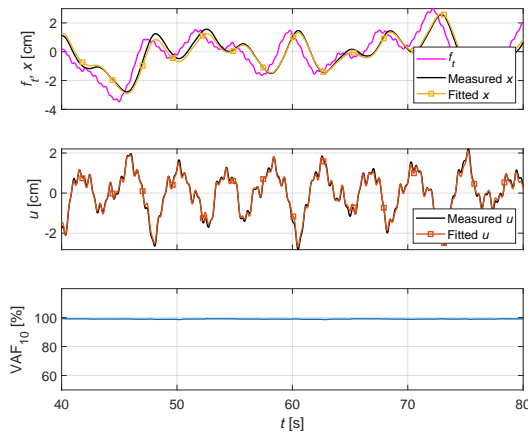


(a) CE position, x , and HO input, u time-traces of subject 7 at C1.

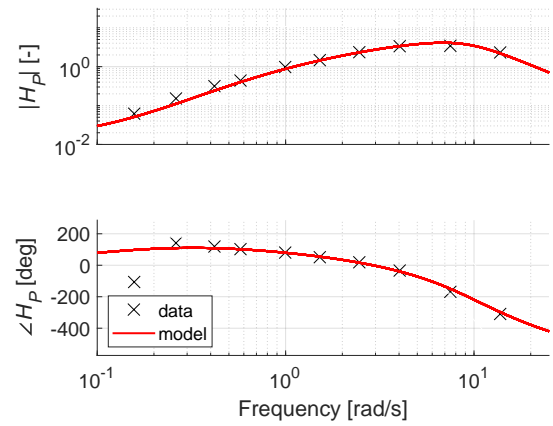


(b) Frequency response of subject 7 at C1.

Figure A.13: Measured and fitted results of subject 7 at C1.



(a) CE position, x , and HO input, u time-traces of subject 7 at C3.



(b) Frequency response of subject 7 at C3.

Figure A.14: Measured and fitted results of subject 7 at C3.

Table A.7: Summary of measured results and estimated parameters of subject 7 at all conditions.

	RMS_e [cm]	RMS_u [cm]	Γ_{u,f_t} [-]	K_e [N m cm ⁻¹]	T_I [s]	τ_e [s]	ω_{nm} [rad s ⁻¹]	Q_{MLE} [-]	VAF [%]
C1	0.991	1.694	0.655	0.069	1.13	0.256	3.78	0.985	86.44
C2	0.920	1.242	0.752	0.085	1.752	0.284	4.51	0.990	98.26
C3	0.905	1.264	0.724	0.071	1.366	0.252	5.34	0.996	98.97

B

Derivation of HO Neuromuscular Model Dynamics

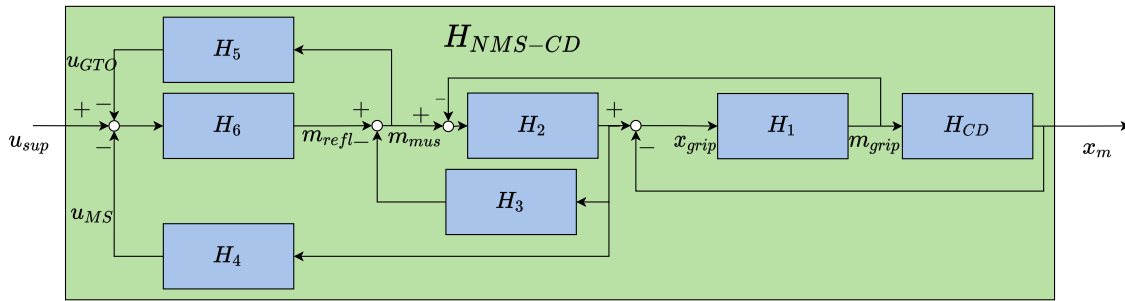
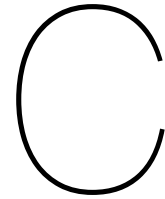


Figure B.1: Schematic description of the detailed model of the HO neuromuscular system including intermediate signal names for analytical derivation.

The dynamics of the model of HO neuromuscular dynamics, $H_{NMS-CD}(j\omega)$, were derived with the following steps.

$$\begin{aligned} \square(j\omega) &= \frac{m_{grip}}{x_{grip}} = \frac{H_1(j\omega)}{1 + H_1(j\omega)H_{CD}(j\omega)} \\ \Delta(j\omega) &= \frac{m_{grip}}{m_{mus}} = \frac{H_2(j\omega)\square(j\omega)}{1 + H_2(j\omega)\square(j\omega)} \\ \star(j\omega) &= \frac{m_{mus}}{m_{refl}} = \frac{1}{1 + (1 - \Delta(j\omega))H_2(j\omega)H_3(j\omega)} \\ H_{NMS-CD}(j\omega) &= \frac{x_m}{u_{sup}} = \frac{H_6(j\omega)\star(j\omega)}{1 + H_6(j\omega)\star(j\omega)(H_4(j\omega)H_2(j\omega)(1 - \Delta(j\omega)) + H_5(j\omega))} \Delta(j\omega)H_{CD}(j\omega) \end{aligned} \quad (B.1)$$

Any simple mistake in the analytical derivation of the dynamics a block diagram model of this complexity would make the outcome incorrect. Therefore, the outcome, $H_{NMS-CD}(j\omega)$, was verified using a MATLAB Simulink tool, `linearize.m`, that numerically approximates the frequency response of a block diagram model.



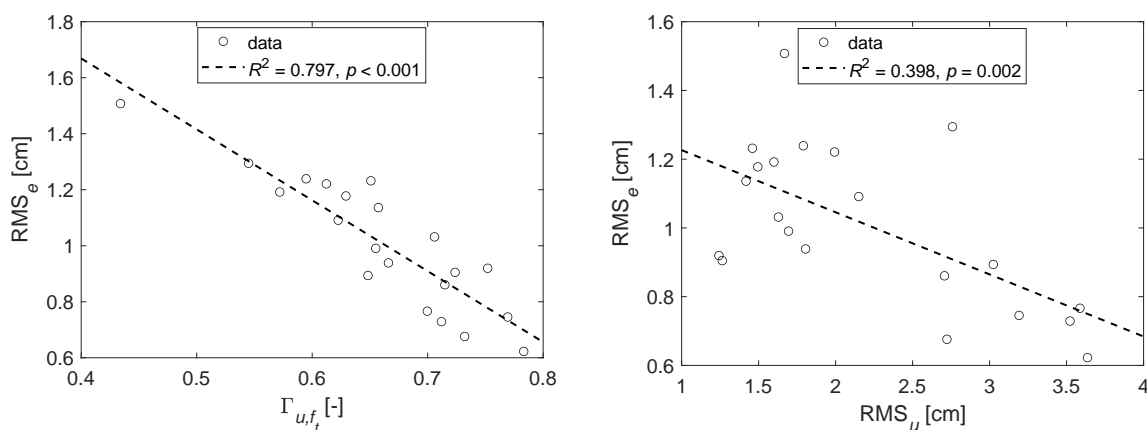
Tracking Task Metrics Correlation Analysis

A global correlation between theoretical GTO activity, σ_{GTO} , and tracking performance, RMS_e , was found with the three manipulator conditions. This appendix investigates this correlation in greater detail within each condition and also examines correlation between other metrics from the tracking task.

C.1. Coherence and Tracking Error

In the control task, the HO's task is to minimize RMS_e . When examining the HO inputs, $u(t)$, a high value of coherence, Γ_{u,f_t} , between $u(t)$ and the target signal, $f_t(t)$, is desired since it can justify the use of quasi-linear models of HO behavior. Figure C.1a shows that with our participants, a strong correlation exists between the average coherence and the achieved tracking error. Participants that performed control inputs with a high degree of linearity were hereby able to achieve lower tracking errors. This means that high coherence not only justifies quasi-linear models, but is also related to better tracking performance.

Equally, Figure C.1b demonstrates that higher control activity is also related to better tracking performance. However, this relationship is not as strong shown by the shallower gradient of the trendline.



(a) Correlation between average HO input coherence and tracking error. (b) Correlation between average HO control activity and tracking error.

Figure C.1: Correlation between average HO input linearity or control activity and tracking error. Each datapoint represents the average obtained metrics of the three 120 s measurement runs of one participant.

C.2. GTO Activity and Tracking Error

It was found that manipulator conditions that lead to higher theoretical GTO activity also showed better performance in terms of RMS_e . Figure C.2 confirms this when visually examining the location of the data clusters of each of the three conditions. This can partially be attributed to the used model setup that includes the varying manipulator conditions.

Furthermore, the figure reveals that within each condition, participants that had higher activity of the GTO, found after parameter estimation, also accomplished smaller tracking errors. This effect within each condition is not a direct result of the model setup. This indicates that higher GTO activity irrespective of the condition is related to better performance.

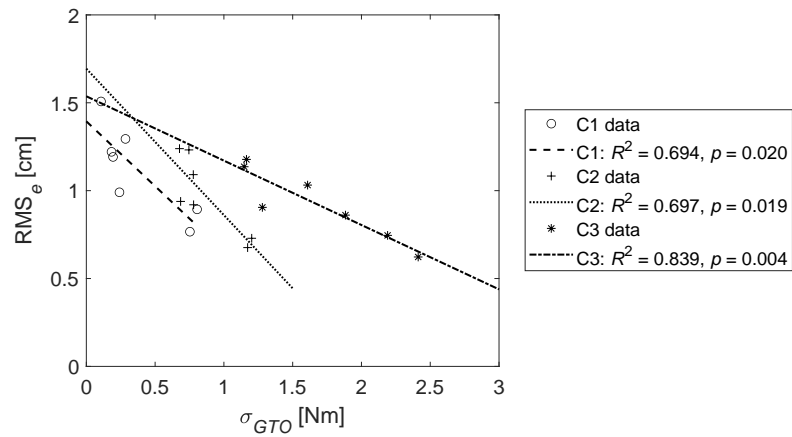
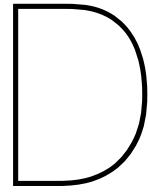


Figure C.2: Correlation between theoretical GTO activity and tracking error. Each datapoint represents the average obtained metrics of the three 120 s measurement runs of one participant. Each manipulator condition is analysed separately in this figure.



Experiment Briefing & Consent Form

Before conducting the experiments, participants were briefed and asked for their written consent for participation according to the requirements from the Human Research Ethics Committee using these two documents.

Proprioception in Manual Control

The two experiments you are about to participate in together aim to show what roles force and position measurement of the human arm play in a manual control task.

The first experiment intends to measure your accuracy in sensing different forces and different positions. In the second experiment, we will attempt to see if different side stick controller dynamics allow you to better make use of these capabilities in a tracking task.

Because of the simple nature of the experiments, you may feel mentally tired. There will be breaks to try to minimise this. If you feel tired at any point, or want to take extra breaks for no particular reason, we will do so when you wish to.

I hope you will enjoy the experiments! If you wish you can review your results in comparison to the statistics from other participants as soon as they have been processed, to see how you performed.

When publishing results, it will be ensured that these will not be identifiable to you. Your personal data will not be distributed. Stored data from this study will not be identifiable to any of the participants.

If you wish to retract from this study at any point, you are free to do so without giving a reason.

If you have any questions, comments or complaints about the experiments or the study, you can contact any of:

- Myself: m.boogaard@student.tudelft.nl, +31625380268
- My MSc thesis supervisors:
 - Dr.ir. M.M. (Rene) van Paassen M.M.vanPaassen@tudelft.nl
 - Prof. dr. ir. M. (Max) Mulder m.mulder@tudelft.nl

Consent Form for Proprioception in Manual Control

Please tick the appropriate boxes

Yes No

Taking part in the study

I have read and understood the study information dated [DD/MM/YYYY], or it has been read to me. I have been able to ask questions about the study and my questions have been answered to my satisfaction.

Yes No

I consent voluntarily to be a participant in this study and understand that I can refuse to answer questions and I can withdraw from the study at any time, without having to give a reason.

Yes No

I understand that taking part in the study involves two manual control experiments and short interviews documented with written notes.

Yes No

Risks associated with participating in the study

I understand that taking part in the study involves the following minimal risks: mental fatigue/boredom.

Yes No

Use of the information in the study

I understand that information I provide will be used for a published final thesis report.

Yes No

I understand that personal information collected about me that can identify me, such as my age, gender and name, will not be shared beyond the study team and will be anonymised to prevent identification of the participant.

Yes No

I agree that my comments during the experiments and short interviews can be quoted or paraphrased anonymously in research outputs.

Yes No

Future use and reuse of the information by others

I give permission for the control inputs, answers to questions and age and gender information that I provide to be anonymised and archived in 4TU.ResearchData so it can be used for future research and learning.

Yes No

Signatures

Name of participant: [printed]

Signature

Date

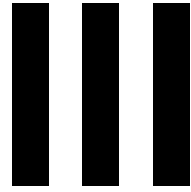
I have accurately read out the information sheet to the potential participant and, to the best of my ability, ensured that the participant understands to what they are freely consenting.

Researcher name: Menno Boogaard

Signature

Date

Study contact details for further information: Menno Boogaard, +31625380268, m.boogaard@student.tudelft.nl



Preliminary Research Report

As graded separately (08-03-2021) for AE4020 Literature Study

Abstract

Modelling pilot behavior in manual control tasks with a side stick has been researched in the past. Recent work showed how the Golgi tendon organ and muscle spindles can be included in a biodynamic feedthrough model of pilot dynamics. Evidence can be found that suggests that there is a significant difference between the relative accuracy of the Golgi tendon organ and the muscle spindle. Force measurement in the Golgi tendon organ is suggested to be more accurate than position and velocity measurement in the muscle spindle. The pilot model was examined to find that stiffer and heavier stick dynamics cause the pilot to rely more on the Golgi tendon organ. This suggests that tracking performance would be improved with a stiffer and heavier stick. Simulations did not confirm this but previous experiments in literature did show a performance improvement with heavier sticks. Present simulations of the pilot model and previous research did show coherent results that tracking performance is better with lower frequency forcing functions. Consistent results between literature and simulations were also found about which parameters in the pilot model depend on stick settings and forcing function bandwidth. With this knowledge, an initial experiment plan was drafted for two experiments. The first intends to show the suggested performance difference of force and position measurement and the applicable conditions for these results. The second aims to show the effects this performance difference has in a control task and validate expectations that were made based on literature and simulation for this control task.

Introduction

Within the field of manual control, having an accurate model of the pilots behavior and capabilities has many purposes. It can serve to predict how pilots will respond to automated support systems. Having accurate knowledge about the pilots sensing also helps with designing these support systems to appropriate specifications. This improvement of human machine interaction allow better safety and lower pilot workload when performing manual control tasks.

Furthermore, knowing the thresholds of human perception also has its uses in developing adequate simulator requirements. There is no point in requiring simulators to have higher fidelity than what is noticeable to the user. Having better requirements for simulators will allow them to be designed more efficiently to the users needs.

Manual control tasks have been studied extensively in the past. In particular a well documented model of the behavior of the human pilot in a compensatory tracking task is available [24]. This model uses an approach where the pilot is modeled by a simple pilot equalization and time delay. When formulating a more accurate model of the pilot in a control task, the pilot, control device and controlled element are modelled separately. Now, it is possible to zoom in on the pilot and distinguish the dynamics of the components that make up the pilot in a tracking task with a side stick. An important part of this neuromuscular interaction between the human operator and the control device is related to the proprioceptive sensing of the arm position and force. These are measured by the muscle spindles (MS) and Golgi tendon organs (GTO) respectively. These sensors are used in internal feedback loops that make up a crucial part of a more detailed pilot model. Recent work has shown evidence that Golgi tendon organs have considerably better accuracy than muscle spindles [13]. If this can be definitively proven, it would have significant implications for manual control tasks. This would allow haptic control support systems to be designed more effectively. Furthermore, better predictions on pilot inaccuracies can be made and the circumstances at which they occur can be better known. This knowledge could help predict which control device dynamics are best suited for particular control scenarios. Control tasks which require tracking at high frequency may benefit from different side stick settings than low frequency tracking. In order to make use of any knowledge about the performance of MS and GTO, this knowledge and its boundaries do need to be established. That means quantifying this performance and comparing it between MS and GTO. Also a description for which conditions any possible claims hold will be needed.

The scope of this thesis will be limited to a compensatory tracking task with a passive side stick with mass spring damper like dynamics. These dynamics will be varied to see how the activity of GTO and MS respond. However, results obtained from different passive side stick dynamics could well become useful when designing an active side stick that supports the human in performing a control task. Also the bandwidth of the target and disturbance forcing functions will be varied. The stick dynamics together with the forcing function bandwidth will be referred to as the control task parameters.

The main research question that will be explored is: **What roles do force and position measurement of the human arm play in neuromuscular control applied to a manual control task?**

This can be broken up into three narrower directions:

- How do human position measurement and force measurement compare across different conditions?
- How does the pilot use muscle spindles and Golgi tendon organs in a manual control task?
- In what way can a control task be optimized to exploit any possible performance difference between muscle spindles and Golgi tendon organs?

Answers to these questions may in the future be useful for improving human machine interaction in real vehicles or a simulator environment.

This preliminary report outlines how these answers can be found in this thesis. This will be done by examining results from previous research and using simulations which will also form a basis for designing the proposed experiments and predict their outcome.

The discussed literature deals with human capabilities of sensing force and position (Chapter 2), the components of the neuromuscular system that are responsible for sensing force and position (Chapter 3) and how this can be used in a model of pilot dynamics in a manual control task (Chapter 4).

Relevant computer simulations are proposed and their results are discussed. These computational experiments are intended to form a basis for predictions on the effects that the pilot qualities found in literature have in a manual control task. Chapter 5 discusses how the simulated representation of uncertainties of pilot behavior affects these simulations after which Chapter 6 defines a usable region of the used pilot model by examining its stability. In Chapter 7, several computational experiments are performed with changing parameters of a manual control task. These intend to reveal how force- and position sensing contribute in a control task and to examine what changes in control task parameters can be used to show the effects of these proprioceptive qualities.

Finally, Chapter 8 proposes two human-in-the-loop experiments. The first experiment will intend to reveal any proprioceptive accuracy difference between force and position measurement and the range where these conclusions would hold. The second experiment aims to uncover the effects of the conclusions of the first experiment in a manual control tracking task. It will thus be the physical form of the computational experiments conducted that have been conducted for this preliminary report. The results from these physical experiments will then allow the predictions that are made in this preliminary report to be validated. This may require repeating simulations with data from the physical experiments. Ultimately, conclusions that are useful in relevant fields such as haptic feedback systems need to be drawn.

2

Force- vs. Position Measurement

In work by Fu, evidence was found that suggests that human force measurement is more accurate than position measurement [13]. The participants were tasked to discriminate if a given stick stiffness was different from the reference stiffness (K_r) with three different conditions. In the force condition the participant only applies a different stick force and equal stick deflection is ensured with a visual display of a reference target displacement (δ_r) and the actual displacement. During the position condition a visual display is used to show a reference target torque (T_r) and the actual applied stick torque such that the stiffness discrimination is based on the participants perception of the applied stick displacement. For these two conditions, participants looked at a display such as the one in Figure 2.1. Finally, the free condition allowed the participants to discriminate between different stick stiffnesses without a target force or target position.

The minimum threshold of stiffness difference that was noticeable for the participants was determined using a staircase procedure, where the difference between the reference stiffness and the controlled stiffness was decreased incrementally until participants were no longer able to correctly identify which stiffness was higher. This resulted in the lowest noticeable difference known as just noticeable difference (JND) expressed as a percentage of the reference stiffness.

Participants performed significantly better in the force condition where discriminating the stick stiffness was based only on applied stick force. The JND of force was measured to be $8.01\% \pm 2.72\%$. In the position condition, the position JND of $14.64\% \pm 6.16\%$ was significantly higher. In the free condition, a stiffness JND of $10.28\% \pm 3.12\%$ was found. These results were obtained at one set of reference conditions shown in Table 2.1. Here the targets δ_r and T_r do match according to $T_r = \delta_r K_r$.

The results of this experiment are easily interpreted to suggest a better accuracy of controlling force exerted by the human arm than controlling the actual position of the arm. This leads to the expectation that the same accuracy difference holds for the perception of force and position. The conditions at

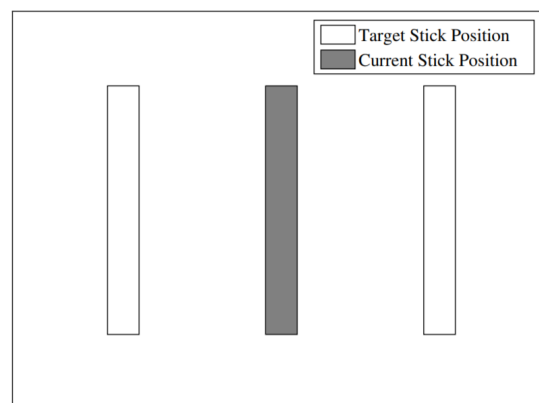


Figure 2.1: Visual display of target stick position in JND experiment [13]

Table 2.1: Reference values for JND experiment

Symbol	Value
K_r	3.5 N m rad^{-1}
δ_r	0.37 rad
T_r	1.295 N m

which this experiment were performed are, however, limited. In order to draw definitive and useful conclusions, the range of these conditions needs to be expanded. Other experiments show similar results when compliance JND is measured [31]. Here, force cues were shown to play an important role in discriminating the compliance when physically squeezing an object between two fingers. This is equivalent to the importance of force perception when discriminating between changing stick stiffness.

Other literature reports a similar observed value for the force JND [2]. Position JND has not been researched as much in the past. Experiments can be used to measure the absolute precision of position sensing [32]. The drawback is that this absolute precision can not be represented as a percentage in the way that was discussed earlier. This means that this absolute precision cannot be compared with the force JND. When investigating the human capability to reproduce a hand position actively or passively, a similar result can be observed. When the human actively reproduces a hand position by moving a handle to a target position by hand, this observed accuracy is better than with passive position reproduction where the handle was moved by an external force [22].

It would be useful to perform a comprehensive study on how force JND and position JND relate for a range of conditions pertaining the side stick, that would be relevant in manual control tasks. In order to compare the two JNDs, they should be measured with the same side stick under the same conditions. A discussion of this will follow in Chapter 8.

3

Muscle Sensory Afferent Activation

In Chapter 2 evidence was given that suggests that Golgi tendon organs have better accuracy than muscle spindles. This evidence is based on experiments that look at the human pilot as one system. This showed that the human pilot is better able to distinguish different forces than different positions of a side stick controller. The different parts of the neuromuscular system that play a role in this discrimination task were not measured separately. This chapter outlines these parts of the neuromuscular system and their roles.

In the past, experiments on isolated parts of the neuromuscular system have been performed and documented in literature. This chapter will focus on literature about the response of Golgi tendon organs and muscle spindles. In particular, their accuracy and response to different frequencies will be of interest.

The afferent fibers that play a role in proprioceptive sensing can be categorized by the following three types [12]:

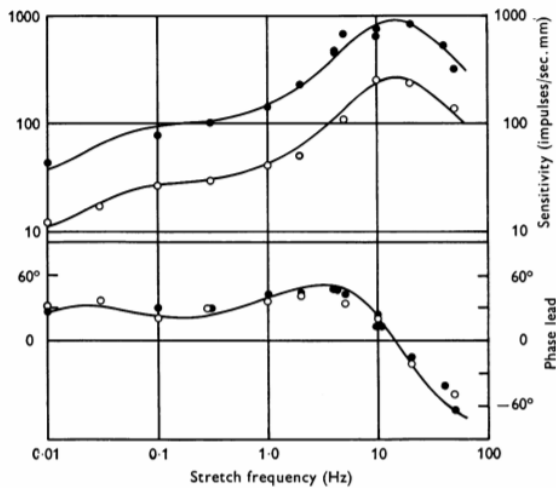
- Type II afferent fibers/ Secondary muscle spindle endings. Sensitive to muscle length modelled with K_p (MS)
- Type Ia afferent fibers/ Primary muscle spindle endings. Sensitive to muscle stretch velocity modelled with K_v (MS)
- Type Ib afferent fibers sensitive to muscle tension modelled with K_f (GTO)

The function of Golgi tendon organs was traditionally thought to be preventing excessive strain on muscle fibres [18].

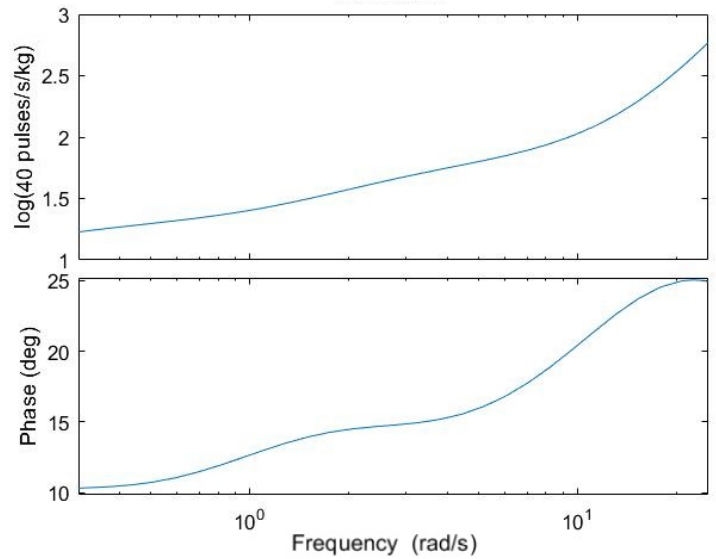
Figure 3.1 shows a relatively constant magnitude of the frequency response of Golgi tendon organs and muscle spindles.

Other research showed that the response of Golgi tendon organs is found to vary linearly with the applied tension [14]. This means that the model of the Golgi tendon organ of a static gain equal to K_f can be considered accurate. Research also showed that Golgi tendon organs have reasonably consistent responses to repeated successive stimulations [4]. Experiments that lead to these observations were performed on cats but are assumed to be relevant for humans as well.

Muscle spindles are known to respond to both position (by K_p) and stretch velocity (by K_v). Muscle spindle firing rates were found to show irregularities under specific conditions during shortening or stretching [5]. Other work showed that the primary muscle spindle endings which are sensitive to velocity are also more responsive to high frequency vibrations ~ 200 Hz. Secondary muscle spindle endings which are responsive to position are only responsive to vibrations up to ~ 100 Hz. [6] Though, both these frequencies are well above the relevant frequency range for manual control tasks such as the one considered for this thesis. When very small length changes are considered, a difference between the primary and secondary muscle spindle endings was shown. Primary muscle spindle response is much greater than secondary muscle spindle response in these situations. This was found in a study that measured the impulses from muscle spindles when the muscle length was changed [23]. Figure 3.2



(a) Response of a muscle spindle unit (Combined type II and Ia afferents) [20]



(b) Golgi tendon organ response in pulses per second to controlled applied muscle force [18]

Figure 3.1: Frequency response of proprioceptive sensors

shows that Ia afferents are more sensitive to small vibrations than II afferents over a range of stimulation frequencies.

A different study analyzed the vibration sensitivity of the muscle spindles and Golgi tendon organ. This showed that Golgi tendon organs as well as muscle spindles play a role in sensing small muscle length changes. [12]

Further work also provides evidence that only muscle spindles are not the only sensors that contribute in joint position control. Simulated experiments suggest that a combination of GTO and MS enables accurate perception of muscle and tendon length. Figure 3.3 shows how GTO feedback considerably improves the disturbance response compared to only MS feedback. [21]

Other experimental research further illustrated the differences in responses of the different afferent types to ramp stretching of the muscle [9]. Later, the responses of the different afferents was described for different manipulations. Clear differences were shown between ramp stretch, vibrations and isometric contraction. [10] One can conclude that Golgi tendon organs are better able to encode isometric muscle contraction than muscle spindles. This observed lower sensitivity to small position changes seems to correspond with recent results found in experiments with a side stick.

In conclusion, research on the different sensory afferents in muscles shows that the conventional concept that muscle spindles encode the length of muscles is not entirely comprehensive. Golgi tendon organs certainly also play a role in the sensing and control of the human arm.

Increased muscle tension without change in length

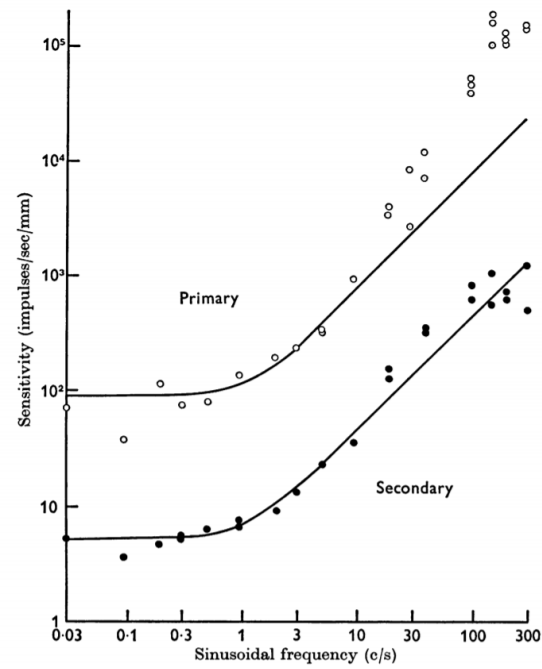


Figure 3.2: Comparison of the sensitivity of primary (Ia) and secondary (II) muscle spindle endings to sinusoidal vibrations at varying frequency [23]

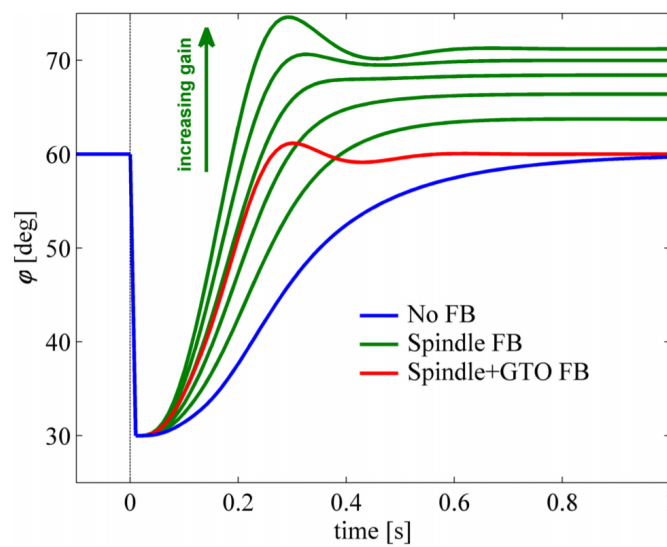


Figure 3.3: Simulated response to position perturbation in 2-DOF position control task [21]

4

Pilot Model

A model of the dynamics of the human pilot in a compensatory tracking task needs to be established as a basis for exploring the effects of human proprioceptive qualities discussed in Chapters 2 and 3. These dynamics are not known precisely due to the complexity of the neuromuscular system and the presence of nonlinearities. In the past, a robust model for these dynamics has been established [24]. This simple model of course has limited accuracy. A more accurate model of pilot dynamics was suggested [34]. Also, a model to represent the human pilots arm as a system with a mass spring and damper was explored [33]. More recently, a biodynamic feedthrough model of the pilot was proposed to achieve a more accurate representation of the pilot dynamics [35]. This most recent model is considered to be most useful in this thesis. This is because it separately addresses the Golgi tendon organs and muscle spindles with their own dynamics in individual feedback loops. The model will be discussed in more detail below and will form the basis for performed simulations for this thesis.

Figure 4.1 gives a visual representation of the biodynamic feedthrough model of the pilot dynamics inside a compensatory tracking task. In this task, the target signal (f_t) and disturbance signal (f_d) are sums of ten sinusoids. The goal of the tracking task is to make the output roll angle (ϕ) follow f_t , i.e., minimize the error signal (e). This error signal is visually displayed to the pilot. When the model is used to describe the pilot in a compensatory control task, the cognitive (supraspinal) input (u_{sup}) is added to the inputs of the neuromuscular activation dynamics (H_6). The output is the position of control device (in this case the side stick). u_{sup} is defined by the error signal which is first processed by the pilots cognitive processes which will be modeled by a PID controller. The stick dynamics are set to the dynamics of a mass spring damper system.

The hand grip dynamics are modeled by the grip stiffness (K_g) and damping (B_g). The intrinsic muscle dynamics are modeled by the intrinsic muscle stiffness (K_i) and damping (B_i). The response of the pilots arm is defined by its inertia (I_{arm}). The response of the muscle spindle is described by a proportional response to the arm position (K_p) and the arm velocity (K_v). The response of the Golgi tendon organ is proportional to the exerted muscle force (K_f). The response of the muscle fibres (m_{refl}) to the input from the nervous system (u_{tot}) is described by the neuromuscular dynamics.

Finally, the controlled element which will be considered in this thesis is defined by H_{CE} in Table 4.1 [13]. Time delays of 0.025 s are present in the model at the muscle spindle and Golgi tendon organ

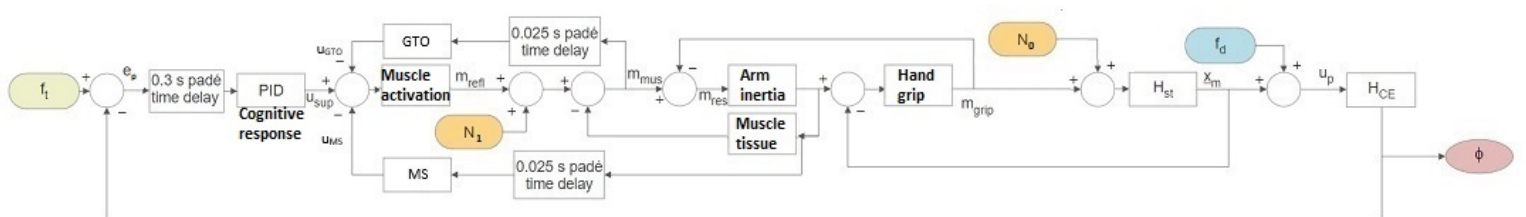


Figure 4.1: Block diagram of the neuromuscular model with components described in Table 4.1

Table 4.1: Mathematical model of the components of the pilot model

Description	Mathematical model
Cognitive response	$PID = P_e + \frac{I_e}{s} + D_e s$
Stick dynamics	$H_{st} = \frac{1}{I_{st}^2 s + B_{st} s + K_{st}}$
Grip dynamics	$H_1 = B_g s + K_g$
Arm dynamics	$H_2 = \frac{1}{I_{arm}^2 s}$
Intrinsic muscle dynamics	$H_3 = B_i s + K_i$
MS response	$H_4 = K_v s + K_p$
GTO response	$H_5 = K_f$
Neuromuscular activation	$H_6 = \frac{1}{\omega_{act}^2 s^2 + 2 \frac{\zeta_{act}}{\omega_{act}} s + 1}$
Controlled element	$H_{CE} = \frac{1}{0.083s+1} \cdot \frac{K_{plant}}{0.4s^2s} \cdot \frac{2.259s^2+0.821s+1}{1.647s^2+0.336s+1}$

blocks and a time delay of 0.3s is present in the cognitive response of the pilot. A mathematical description of the dynamics of these pilot model blocks is given by Table 4.1. Tables 4.2 and 4.3 report the numerical values for the discussed parameters of this model. In Table 4.2, only the values of the parameters below the double line will be investigated further in the following chapters. These values were considered task dependent in previous research. Hence the scope of this thesis will be limited to these parameters. This task dependency implies the values differ between the position task (PT), relax task (RT) and force task (FT). As with any model of a real process, this pilot model will not cover the dynamics fully due to nonlinearities. This is represented by the pilot remnant (N). This noise signal is discussed in Section 4.2.

Table 4.2: Pilot model parameters for PT, FT and RT. Values above the double line will not be discussed or investigated in detail in this thesis.

Symbol	Unit	PT	FT	RT
ω_{act}	rad s ⁻¹			13.823
ζ_{act}	-			0.7071
B_g	N m s rad ⁻¹			2
K_g	N m rad ⁻¹			165
I_{arm}	kg m ²			0.01
B_i	N m s rad ⁻¹			1
K_i	N m rad ⁻¹	11	9	10
K_p	N m rad ⁻¹	9	-6	10×10^{-10}
K_v	N m s rad ⁻¹	2	3	10×10^{-10}
K_f	-	-1.5	1.5	10×10^{-10}

Table 4.3: Baseline side stick parameters

Symbol	Value
K_{st}	2 N m rad ⁻¹
I_{st}	0.01 kg m ²
B_{st}	0.2 N m s rad ⁻¹
resulting in:	
$\omega_{0st} (= \sqrt{\frac{K_{st}}{I_{st}}})$	14.14 rad s ⁻¹
$\zeta_{st} (= \frac{B_{st}}{2\sqrt{K_{st} \cdot I_{st}}})$	0.7071

A more detailed description of this model can be found in the documentation by Venrooij et al. [35].

The parameters of the PID block that define the pilot's cognitive response are initially set to $P_e = 5$, $I_e = 0$ and $D_e = 5$. At this point, it is worth noting that these parameters are likely to depend on the control task settings defined by the side stick dynamics and the forcing functions (f_t and f_a). When the

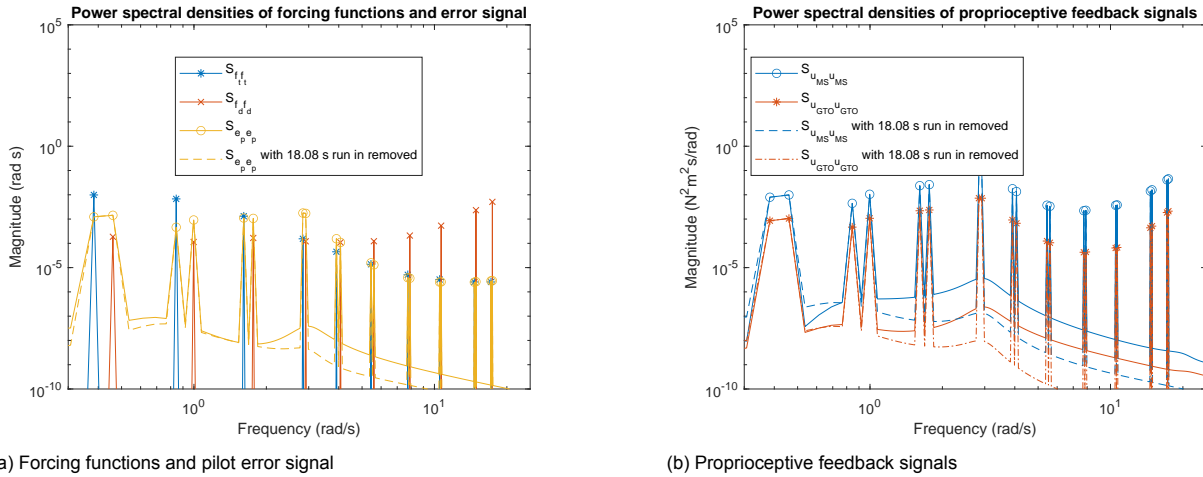


Figure 4.2: Spectral analysis of pilot model signals defined in Figure 4.1 with settings for PT from Table 4.2

stiffness of the stick is increased, the pilot will likely increase parameters P_e , I_e or D_e to generate the higher required force to move the stiffer stick. This concept will be explored in more detail in Chapter 7.

4.1. Pilot Model Signals

The compensatory control task is simulated with forcing functions f_t and f_d according to BW2 defined in Section 7.3, resulting in time traces of 90 s sampled at 200 Hz for all model signals. The first 8.08 seconds of these signals are removed such that only the steady state behavior and not the transient behavior is examined, resulting in a measurement time of 81.92 s. Drawing relevant conclusions from looking at these time traces from this computational experiment is too difficult. Examining their spectra will give useful information about the frequencies at which these signals have power. The auto power spectral densities were generated defined by the squared absolute value of the discrete Fourier transform (DFT) of the signal, divided by the squared number of samples. [15] The spectra of the forcing functions ($S_{f_t f_t}$ and $S_{f_d f_d}$) in Figure 4.2a clearly only show energy at the ten forcing frequencies. No spectral leakage is visible in these spectra because the ten forcing frequencies were defined at integer multiples of the DFT's frequency resolution ($= \frac{1}{81.92}$). For a linear model such as this one, output signals should only contain energy at the same frequencies of the inputs. Hence, one would also expect to see only energy at the ten forcing frequencies in the model signals' spectra. However, a small amount of energy is present at other frequencies as well in the spectra of the pilot error signal ($S_{e_p e_p}$) and the position- and force feedback signals ($S_{u_{MS} u_{MS}}$ and $S_{u_{GTO} u_{GTO}}$). This is likely caused by the transient response of the model which is still present in the model signals (e_p , u_{MS} and u_{GTO}) despite that the first 8.08 s of the data were not used. This is shown by the dashed lines in Figure 4.2b with an increased the run-in time of 18.08 s. Here, less energy is present at frequencies different from the forcing frequencies compared to the data with only 8.08 s run-in time.

A different possible cause of this artifact comes from inaccuracies of the numerical solver used for this simulation in MATLAB Simulink. This was concluded because the same behavior was observed spectra of the simulated output signals of very simple systems.

4.2. Pilot Inaccuracies

In previous work, the inaccuracies of the pilot were modelled by adding a source of noise between the output of the pilot (m_{grip}) and the manipulator dynamics according to N_0 in Figure 4.1 [1, 26, 33]. Modelling the remnant in this way would be applicable if uncertainties were present in the pilot up until this last point, i.e., the hand grip dynamics (H_1). However, in order to better model these uncertainties, they can be isolated to the parts of the neuromuscular model that cover proprioceptive sensing (GTO and MS) and muscle activation. By this reasoning, a more accurate way of introducing pilot remnant would be by adding noise to signals proprioceptive feedback signals u_{GTO} or u_{MS} , or after the neuromuscular activation dynamics at m_{refl} (according to N_1 in Figure 4.1). This can be done systematically by first measuring the variance $\sigma_{u_{GTO}}^2$, $\sigma_{u_{MS}}^2$ or $\sigma_{m_{refl}}^2$ of these three signals in a simulation of a relevant control task when no noise to model pilot remnant is added to the tracking task. Now, a noise signal can be added to these signals with an appropriate fraction $\frac{\sigma_{noise}^2}{\sigma_{signal}^2}$. This fraction is equal to the inverse of the signal to noise ratio (SNR) which relates signal- and noise energies which are defined as their variance (σ^2).

For all simulations in this thesis that do not take into account variations of the added noise or otherwise state any specifications of the pilot remnant noise, the pilot model remnant will be modelled by the following noise signal. A noise signal filtered by a first order low-pass filter with $\omega_c = 15 \text{ rad s}^{-1}$ will be added to m_{refl} with a noise intensity such that the signal to noise ratio ($\frac{\sigma_{m_{refl}}^2}{\sigma_{noise}^2}$) will be equal to ten. This means that pilot inaccuracies are summarized to be an uncertainty added to the generated muscle force after the neuromuscular activation dynamics. Chapter 5 discusses the effects of this noise signal in more detail.

4.3. Stick Variation

Changing the side stick characteristics in a tracking task, such as the one considered for the current pilot model will influence pilot behavior. It would be desirable to show how changing the settings of the side stick affects how the pilot uses GTO and MS in a manual control task. This is why this thesis explores changes of the stick configuration.

Research has shown that a so called force stick, where $K_{st} = \infty$, resulted in better tracking performance than two other stick configurations that did allow movement of the stick [17]. With a force stick, the force that the pilot exerts on the stick is measured and used as pilot input. Contrarily, with a normal moving side stick, the position of the stick is measured as the pilot input. This research also showed that the pilot adapts to changes between a passive stick and a side stick with haptic feedback.

The observed better tracking performance when the exerted force (rather than achieved stick position) is used as pilot input is consistent with the believed better accuracy of sensing force than position that was introduced in Chapter 2.

Other work based on subjective qualities of the stick showed seemingly different results [36]. Subjective qualities indicated by pilots were generally unsatisfactory with a force stick without movement ($K_{st} = \infty$). Allowing stick movement by a decrease in K_{st} improves the pilots subjective rating of the stick. This work also showed that the force-response gain setting of the side stick is more critical with fixed stick than with a movable side stick.

A comparison of two stick configurations representing the feeling of cruise condition with a stiffer stick and a softer stick for approach showed a clear effect when all other task parameters remained constant [7]. It was shown that a stiffer side stick lowers the pilot admittance and improves the tracking performance.

These previous experiments did show that changes in stick parameters cause significant changes in pilot model parameters as well as in the tracking performance.

5

Effects of Pilot Model Remnant

A representation of the pilot control inaccuracies which cannot be modelled analytically was defined in Section 4.2 as a noise signal added to m_{refl} . This chapter will briefly discuss how variation of the intensity of this noise signal and the location in the model where it is added affects the model. This is done with the goal of establishing a definition of the noise signal representing the model inaccuracies that should be used consistently for all computational experiments for this thesis.

Adding a noise signal to either u_{sup} , u_{GTO} or u_{MS} would all have the same effect. Figure 5.1 shows that these three signals directly sum up as u_{tot} , the input to the neuromuscular activation dynamics (H_6). Hence, adding noise of the same magnitude and spectrum to either of these signals is effectively the same. However, the signal magnitudes of u_{sup} , u_{GTO} or u_{MS} themselves, reported in Table 5.1, are different. u_{tot} is clearly dominated by u_{sup} , followed by the feedback signals u_{GTO} and u_{MS} where u_{GTO} contributes the least. Hence, when adding a noise signal with equal signal to noise ratio as proposed in Section 4.2 to u_{GTO} or u_{MS} , the impact on the performance will be significantly larger when noise is added to u_{MS} . The consequence is that the pilot model in this configuration is more sensitive to relative inaccuracies in the muscle spindles compared to the Golgi tendon organs. It will be of interest to see how relative changes in $\sigma_{u_{GTO}}^2$ and $\sigma_{u_{MS}}^2$ caused by changing the stick dynamics or other experiment conditions impact the tracking performance. This will be investigated in more detail in Chapter 7.

5.1. Effects on Tracking Performance

In a compensatory tracking task, the pilot's goal is to minimize the error (e_p) that is displayed visually and defined as the difference between the target position (ϕ_t) and the controlled element location (ϕ). Hence the tracking performance of the pilot model can be characterised by the standard deviation of the error signal (σ_{e_p}). When no noise is added to the system, and the tracking task is performed at the initially defined conditions, the performance amounts to a baseline of $\sigma_{e_p} \approx 0.1385$ rad. The sensitivity of this performance to changes in model parameters and noise characteristics will be an indication if these changes in model parameters will improve the performance in an actual experiment run.

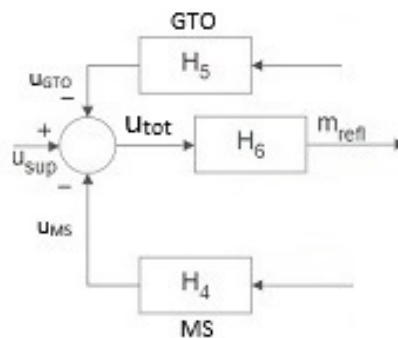


Figure 5.1: Zoomed in section of the neuromuscular model blockdiagram from Figure 4.1

Table 5.1: Simulated signal magnitudes with BW2 forcing functions (see Section 7.3) and model parameters according to the position task without added noise signal

Signal	σ_{signal}^2 (N ² m ²)
u_{sup}	2.641
u_{GTO}	0.056
u_{MS}	0.862
m_{refl}	1.078

In theory, the relation between the variance of the tracking error ($\sigma_{e_p}^2$) and the intensity of the added noise (σ_{noise}^2) with one particular noise bandwidth should be proportional [29]. Figure 5.2 shows how this is also the case in this computational experiment. Here, the tracking performance attained in the computational experiment with increasing signal energy of the noise signal added to m_{refl} representing model remnant is evaluated with 50 different noise realizations. To see this relationship ($\frac{\sigma_{e_p}^2}{\sigma_{noise}^2}$), the variance of e_p is used rather than the σ_{e_p} which is more often used as the definition of the tracking performance.

On average, the slope of $\frac{\sigma_{e_p}^2}{\sigma_{noise}^2}$ in Figure 5.2 is approximately equal to 0.003. According to theory, this is slope should be equal to the system dynamics squared. The added noise signal has energy up to 15 rad s^{-1} so the system dynamics should be evaluated up to this frequency. Figure 5.3 shows that, for these frequencies, the magnitude of the system response is approximately equal to -25 dB . Evaluating the square of these dynamics results in $(10^{-\frac{25}{20}})^2 \approx 0.003$. This confirms that in the results from repeated computational experiments, the way that the energy of the pilot output scales with the noise input agrees with the trend expected from theory.

Importantly, Figure 5.2 shows that different realizations of the same noise signal have considerably different effects on the outcome of simulating the tracking experiment. The figure does show that the average results of 50 noise realizations is coherent with the theoretical outcome. Hence, for all simulated results in this thesis that do include this remnant noise signal, a simple form of Monte Carlo simulation will be required for results to be meaningful [30]. Simulations will be performed by adding 50 different realizations of the filtered noise signal to m_{refl} with corner frequency $\omega_c = 15 \text{ rad s}^{-1}$ at SNR=10 (as introduced in Section 4.2) and reporting the average of the results that come from the 50

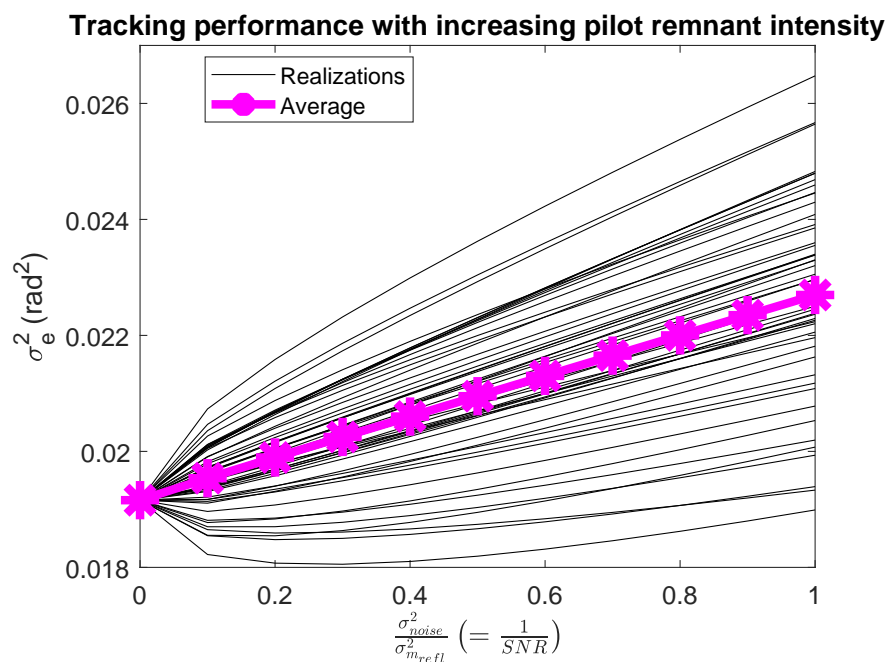


Figure 5.2: Tracking performance with varying pilot remnant intensity at 50 different noise realizations

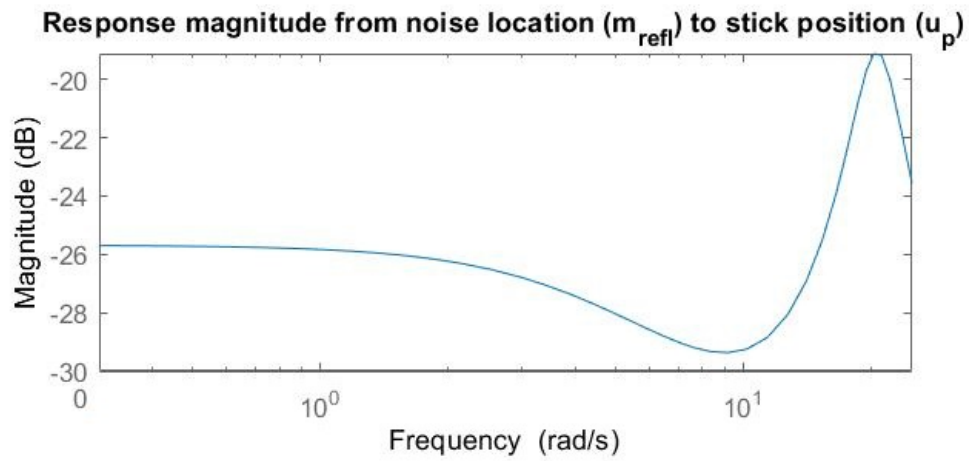


Figure 5.3: Frequency response from noise input location (m_{refl}) to pilot output (u_p) with model parameters according to PT simulations.

6

Stability

After deriving the analytic system dynamics of the pilot model and its various feedback channels, these dynamics can be investigated in the frequency-domain to assess the stability of the model. This is needed to establish the usable region where this model of the pilot dynamics can be used in simulations. The stability of the open loop pilot model (from signal u_{sup} to m_{mus} ($H_{u_{sup},m_{mus}}$)) can be considered separately from the stability of the model acting in a tracking task. This complete tracking task (from the target signal (f_t) to the output signal (ϕ) ($H_{f_t,\phi}$)) includes a feedback channel which represents the visual error the pilot responds to. By looking at the open loop pilot model and the entire tracking task separately, different degrees of stability can be distinguished. The stability of these models is examined for varying values of the proprioceptive gains (K_p , K_v and K_f) introduced in Chapter 4.

6.1. Definitions of Stability

The continuous-time representation of the open loop pilot model has many poles and zeros due to its several internal feedback loops. Some of these poles can move to the right half-plane when parameters of these feedback loops are changed. Figures E.1 to E.11 which will be explained in Section 6.2 show this in detail. When this happens the open loop pilot model becomes unstable. In physical terms this would mean that the pilot output (u_p) would become unbounded when the pilot gets a visual moving input target signal but no visual feedback of the error. GTO and MS feedback channels can lead to this instability, hence this stability can be assessed based on the system up until the point where these feedback channels are added. This will thus be the system from u_{sup} to the force exerted by the muscle (m_{mus}) ($H_{u_{sup},m_{mus}}$).

On the other hand, the stability of the tracking task is not always the same as that of the open loop pilot. In this closed loop tracking task, the pilot would only have a visual display of the error signal (e_p). In order to assess this stability dynamics of the entire tracking task ($H_{f_t,\phi}$) with the pilot model and controlled element in a unit feedback loop were derived. Similarly the presence of unstable poles in these dynamics was checked. Table 6.1 shows a brief overview of these different degrees of stability. For example, CuOs indicates a setting of the pilot model where the entire tracking task becomes unstable whilst the open loop pilot (from signal u_{sup} to m_{mus}) is stable.

Instability of the open loop pilot (CsOu & CuOu) is caused by the GTO and MS feedback channels and occur at relatively high frequencies ($\omega > 5 \text{ rad s}^{-1}$). This is clear from Figures E.1 to E.11 where the cause of instabilities of the pilot model is investigated in detail. Here the location of the poles and

Table 6.1: Pilot model stability classifications with numerical labels used later in Figure 6.2a

	Closed loop ($H_{f_t,\phi}$)	Stable	Unstable
Open loop ($H_{u_{sup},m_{mus}}$)			
Stable		CsOs (2)	CuOs (1.5)
Unstable		CsOu (1)	CuOu (0)

zeros of the system from u_{sup} to m_{mus} are shown. Instability of the closed loop tracking task (CuOs & CuOu) is caused by insufficient stability margins of the open loop pilot. This implies that the open loop system becomes unstable in a unit feedback loop. This is illustrated by Figure 6.1 with the poles and zeros of the feedback system representing the entire tracking task. This shows that the closed loop system becomes unstable at considerably lower frequencies ($\omega < 5 \text{ rad s}^{-1}$) than the instabilities of the open loop pilot. This is according to expectations since the neuromuscular system dynamics are faster than the cognitive process of performing the tracking task.

The parameters that define the GTO and MS feedback blocks were varied to find which combinations result in a stable open loop or closed pilot model. In general, the stability of the open loop pilot and the tracking task were consistent. Yet, in the boundaries of the stable regions, sometimes only the open loop or only the tracking task was stable. The force gain (K_f), position gain (K_p) and velocity gain (K_v) were initially set to the values appropriate for the position task, relax task and force task as in Table 4.2. In Section 6.2, the details of this search for the stable regions will be discussed.

From Figure 6.2, one can deduce that the selected setting of the GTO sensor gain $K_f = -1.5$ for RT allows significantly smaller variations of the MS sensor gains K_p and K_v than $K_f = 1.5$ for FT would. A three dimensional representation of the settings for K_p , K_v and K_f that result in a stable pilot model is given in figure 6.3. This also shows that $K_f = 1.5$ limits the allowed variations of K_p and K_v .

These stability regions were found to change with different stick configurations defined by the parameters in the model of H_{st} in Table 4.1. This is logically caused by changes in the dynamics of the

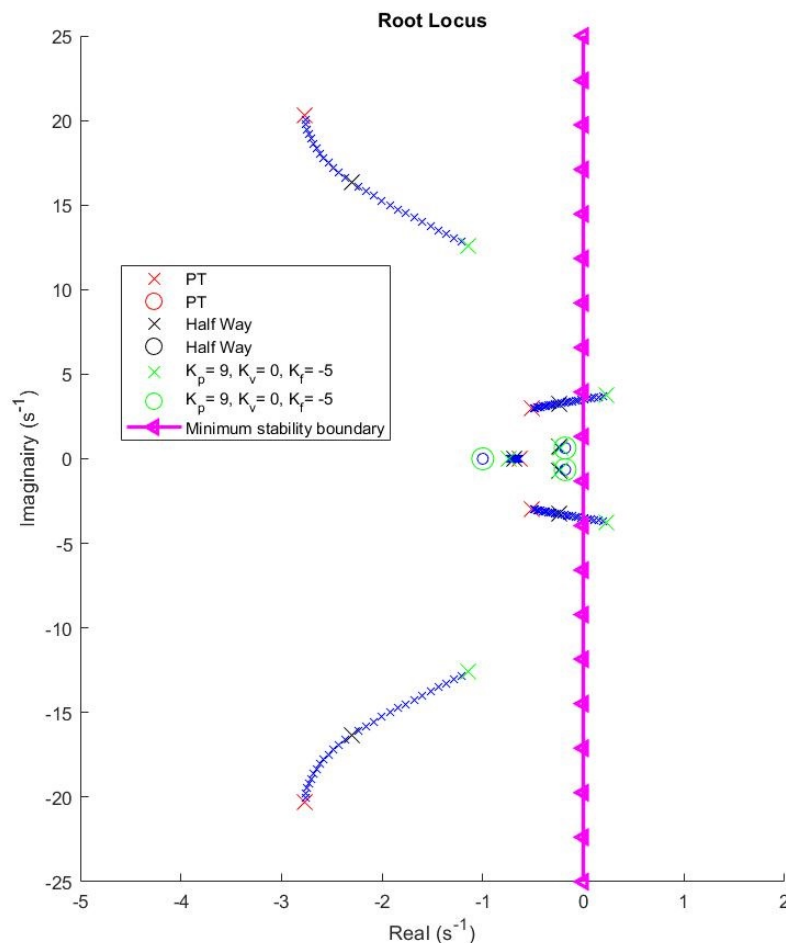
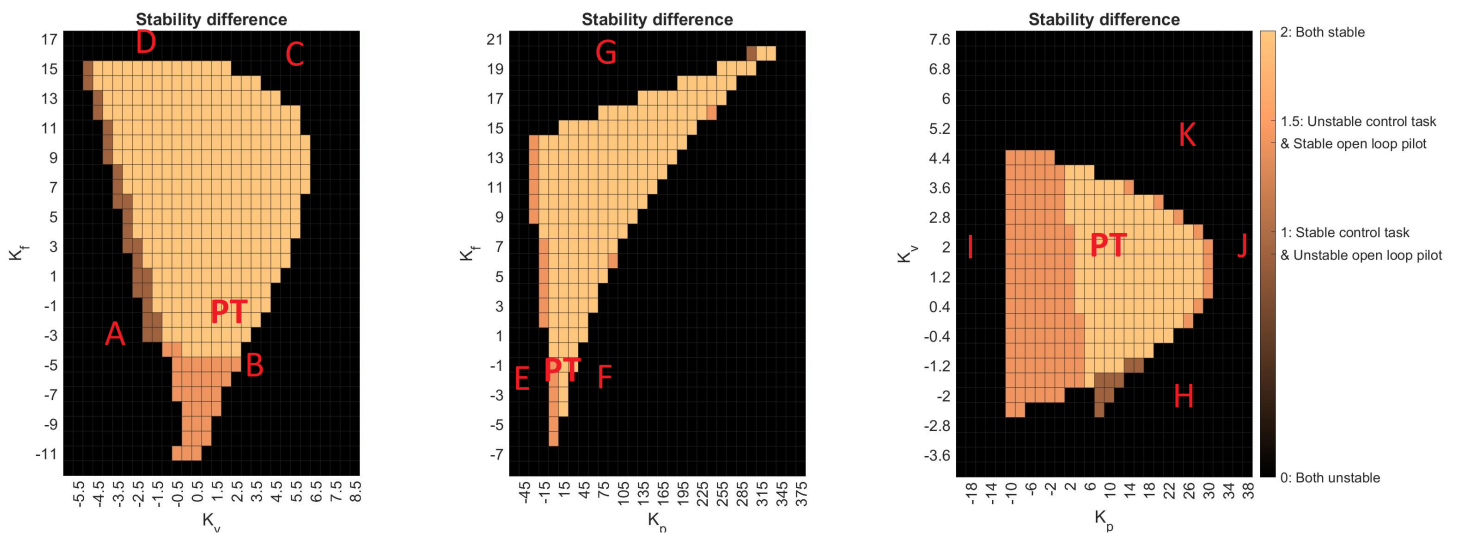


Figure 6.1: Poles and zeros of entire tracking task ($H_{f,t,\phi}$) when becoming unstable. K_v and K_f are varied linearly from PT settings ($K_v = 2 \text{ N m s rad}^{-1}$ and $K_f = -1.5$, see Table 4.2) to $K_v = 0$ and $K_f = -5$.

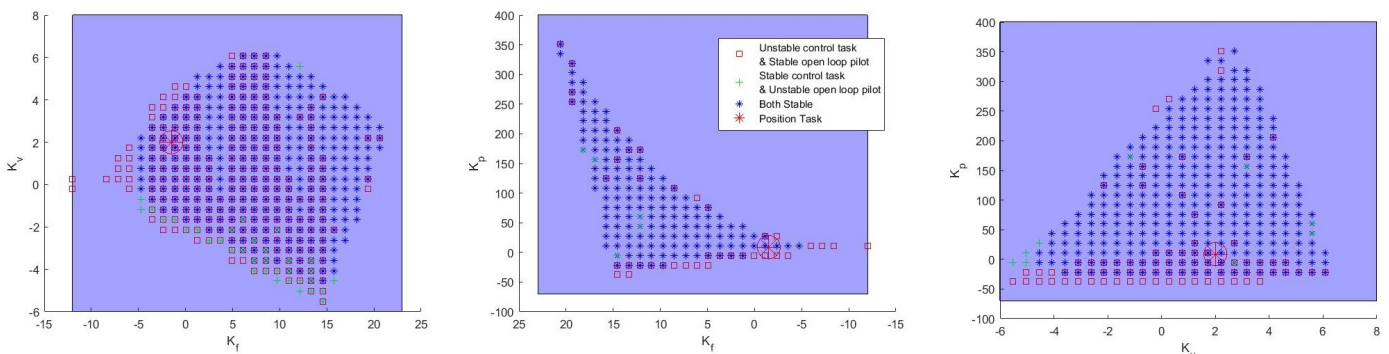
model of the pilot in combination with the stick Figure 7.2. When the stick dynamics change, the poles and zeros of $H_{u_{sup},m_{mus}}$ and $H_{f_t,\phi}$ may be moved to the right half plane.

6.2. Poles at Stability Boundaries

In order to see what causes the instabilities of the open loop pilot model, a root locus plot can be helpful to see how the poles move into the right half plane. This was done at each of the boundaries of the stable regions visible in Figure 6.2a. The root locus plots of $H_{u_{sup},m_{mus}}$ are reported for these boundary crossings in each of the three views separately. If the poles behave apparently equally at the different boundaries within one stability heatmap, the root locus is only shown for one of these boundaries. The root locus plots are generated by drawing the locations of the poles and zeros in the complex plane with varying settings of the proprioceptive gains (K_p , K_v and K_f). For each plot, they are initially set according to values for PT from Table 4.2, and then linearly moved to endvalues outside of the stable region according to locations A until K in Figure 6.2a. These endvalues are selected such that the stability boundaries are crossed close to perpendicular to show the clearest effect in the root locus plots. If the instability boundaries in Figure 6.2a were crossed at a shallower angle, the resulting root locus plots in Figures E.1 to E.11 would show less clear movements of the poles of $H_{u_{sup},m_{mus}}$. Figure 6.4 shows one example of the definition of a line along which the proprioceptive gains are varied. This particular line according to point A in Figure 6.2a leads to the root locus in Figure E.1. The other root



(a) 'Sliced' at proprioceptive gains according to FT (see Table 4.2) (from left to right: $K_p = 9 \text{ N m rad}^{-1}$, $K_v = 2 \text{ N m s rad}^{-1}$ and $K_f = -1.5$) with letters for subsequent root locus analysis and position task indicated by PT



(b) Full side projections

Figure 6.2: Stability regions by varying proprioceptive gains K_p , K_v and K_f .

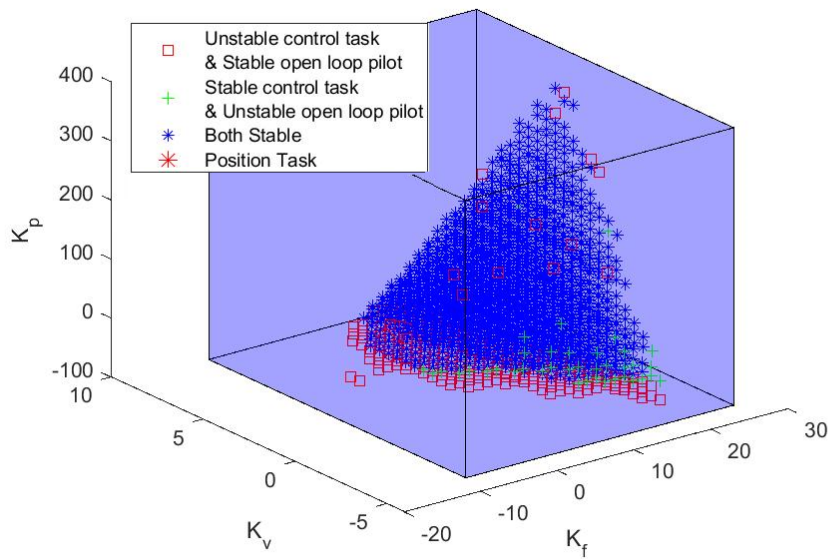


Figure 6.3: Isometric view of stable regions for K_p , K_v and K_f

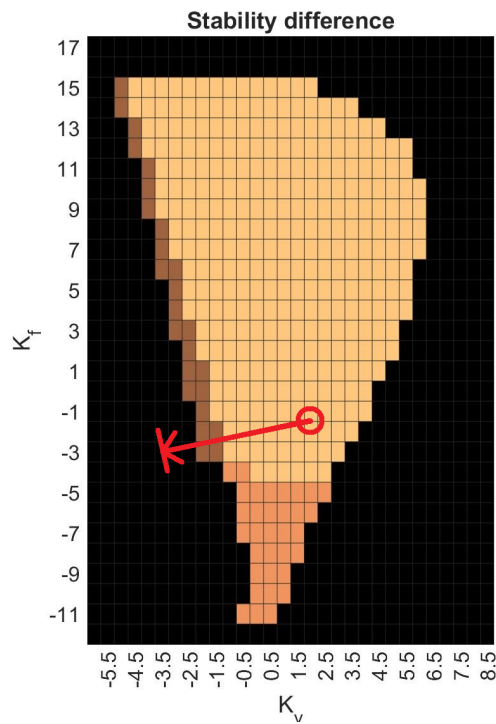


Figure 6.4: Example of root locus line definition used in Figures E.1 to E.11

locus plots in (Figures E.2 to E.11) are generated by variations of two of the three proprioceptive gains to endvalues indicated in the respective legends of the plots. These gain settings are also represented by letters in Figure 6.2a.

Instabilities of the open loop pilot model are caused by insufficient stability margins on either the GTO feedback signal or the MS feedback signal. When either gain margin drops below one, the system becomes unstable when these proprioceptive feedback loops are closed. This is simply the definition of the gain margin. Plots on the right side of Figures E.1 to E.11 show the evolution of these gain margins. The consequences of these gain margins becoming insufficient is shown in the plots on the left. These root locus plots show how the poles move into the right half plane when $\log(\text{gain margin}) < 0 \Leftrightarrow \text{gain margin} < 1$. The plots consistently show that instability caused by too high K_f is caused by insufficient GTO gain margin and too large K_p or K_v is associated with a MS gain margin below 1. Furthermore, the root locus plots allow conclusions to be drawn pertaining to the frequency of the unstable poles that occur. It is clear that two sets of periodic poles of $\sim 20 \text{ rad s}^{-1}$ and $\sim 50 \text{ rad s}^{-1}$ and one aperiodic pole at the imaginary axis are the three possible causes of instability of the open loop pilot. Their causes can be summarized by the following points.

Instability boundaries:

1. When K_f grows larger than a particular boundary dependent on K_p and K_v a high frequency pole of $\sim 50 \text{ rad s}^{-1}$ becomes unstable as shown in Figures E.4 and E.7.
2. When K_p becomes lower than a particular boundary dependent on K_f and K_v an aperiodic pole on the imaginary axis becomes unstable clear in Figures E.5 and E.9
3. At all other stability boundaries, a pole of originally $\sim 20 \text{ rad s}^{-1}$ becomes unstable shown in Figures E.1 to E.3, E.6, E.8, E.10 and E.11. The proprioceptive gain settings at which this occurs are interdependent.

These three boundaries are also distinguishable in 3D in Figures 6.2b and 6.3. The right figure in Figure 6.2b faces stability boundary 1, the left figure faces stability boundary 2. The middle figure shows a part of the 3D curve describing stability boundary 3. The listed stability boundaries do not imply that poles that cause instability at one particular boundary, have the same frequency on this entire boundary. Each of the three boundaries is associated with one particular pole or pair of periodic poles. The frequency of these poles at the boundary is dependent on the exact location on the boundary. In other words, the frequency of the unstable poles changes when the proprioceptive gains are moved along the stability boundary.

In physical terms these boundaries mean that a too high force feedback gain causes high frequency instability of the open loop pilot. A too low position feedback causes aperiodic instability. All other combinations of proprioceptive feedback gains that lead to instabilities, cause instabilities at still reasonably high ($> 10 \text{ rad s}^{-1}$) frequencies.

In Figures E.1 to E.11, the gain margin of the open loop pilot (made up by the pilot model, control device and controlled element, i.e., from the visually displayed error signal to the controlled element position ($H_{e,\phi}$)) is included as well. This is to illustrate the changes pertaining to the closed loop tracking task. This gain margin can be interpreted in a similar way as the internal proprioceptive loops. When the open loop gain margin is lower than one, the open loop pilot will be unstable when placed in the closed loop tracking task. The trend of this gain margin is not that similar between all stability boundaries, so a general conclusion about the gain margin of the open loop pilot cannot be drawn. At FT, the open loop gain margin is approximately equal to 1.5. This reduces to one at some stability boundaries. At other boundaries however, the open loop gain margin does increase. In general, it can be stated that the gain margin magnitude of the open loop pilot does not change as rapidly as the gain margin of the feedback loops for the muscle spindle and Golgi tendon organ.

7

Control Task Parameter Effects

The pilot model that was discussed up to this point can be used to simulate how a pilot would behave in a compensatory tracking task. This will also be the framework of one of the two experiments to be performed which will be discussed in Chapter 8. Here, also the possible parameters to be varied will be discussed. Before selecting which parameters to vary and between what values, it is worthwhile to see if any effects of these variations can be predicted. In this chapter, this will be done by means of theoretical knowledge and simulation of the experiment using the established pilot model. Variations of the task parameters can be distinguished into variation of the stick dynamics (discussed in Section 7.2) and variation of the target and disturbance signals (covered in Section 7.3). The variations of these task parameters are intended ultimately to generate different conditions between which changing behavior of the Golgi tendon organ and muscle can be observed, in computational- as well as human-in-the-loop experiments.

The parameters that define the neuromuscular model that were identified as task dependent in previous work are K_i , K_f , K_p and K_v [3]. In this chapter, the effects of changing these parameters will be investigated. Initially, these parameters will be varied between the appropriate values for the three different tasks, PT, FT and RT from Table 4.2.

Section 7.4 discusses how the pilot would adapt to changing the stick settings or forcing functions in a control task. Specifically, it covers what expectations of this pilot adaptation can be made, based on performing simulations of the used pilot model. This discussion will include the effects of different realizations of the noise signal to model pilot remnant, will be discussed.

7.1. Pilot Model Parameters' Effects on Stability

Varying K_i , K_f , K_p and K_v changes the dynamics of the pilot model which can cause instabilities as mentioned in Chapter 6. Modelling the pilot remnant differently with different noise signals does not affect the system dynamics. Hence, the pilot remnant will not be discussed in detail in this section.

With the parameters for PT, the closed loop and open loop pilot are both stable (CsOs). Changing to FT or RT causes no instability of the open loop pilot model but does make the pilot unable to perform the closed loop tracking task (CuOs). Figure 7.1 shows the changing frequency response between these three settings. This shows that for RT the neuromuscular model strongly resembles a mass spring damper system. This is reasonable since K_f , K_p and K_v are approximately zero for RT. The dynamics for FT and PT are significantly different from a mass spring damper system with all nonzero K_f , K_p and K_v . A straightforward observation from Figure 7.1 is that the magnitude of the steady-state response is lowest for PT, caused by its settings for K_p , K_v , K_f and K_i . This means that these parameter settings make the pilot model less sensitive to low frequency forcing function components than the settings for the force task (FT). With FT, the stick position (u_p) will be more sensitive to low frequency disturbance inputs.

Stability classification from Table 6.1

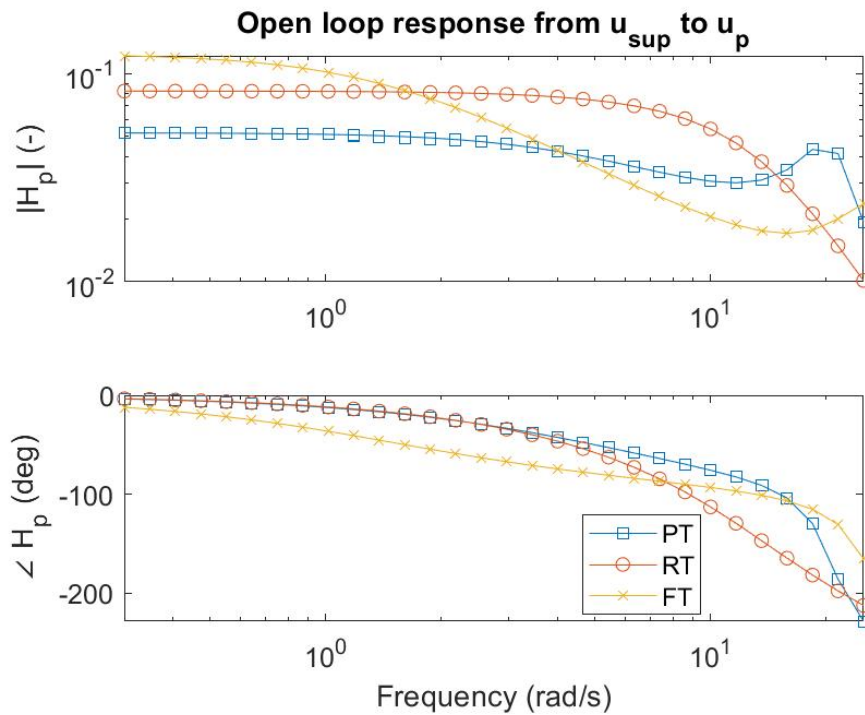


Figure 7.1: Open loop pilot dynamics between parameter settings of K_p , K_v , K_f and K_i for tasks PT, FT and RT from Table 4.2

7.2. Stick Parameters

The dynamics of sidestick are characterised by a mass spring damper system with baseline parameters in Table 4.3 and dynamics described by the transfer function for H_{st} in Table 4.1.

Due to the complexity of the system dynamics described in Chapter 4, analysis of the effects of changing stick parameters will in some scenarios be done based on quantitative effects rather than qualitative analysis.

Previous research discussed in Section 4.3 has shown the effects that variations in stick parameters can have on tracking tasks. Here, it was reported that the pilot model parameters certainly depend on the stick settings. This leads to the intention to show any dependency the current model has on the stick settings.

7.2.1. Variation of Stick Stiffness

Since force measurement is suggested to be approximately 50 % more accurate than position measurement, one could expect that a stiffer stick would allow the pilot to perform the control task based more on force perception than position perception. And in a simulations with increased K_{st} , $\sigma_{u_{GTO}}$ increases as well, while $\sigma_{u_{MS}}$ remains approximately equal. This is shown in Figure 7.4. Figure 7.2 gives a representation of how the dynamics of the stick change when only the stiffness of the stick is increased between a suggested range of values higher or lower than the initial setting of $K_{st} = 2 \text{ N m rad}^{-1}$. Here the input and output are m_{grip} and u_p respectively.

The figure shows how an increase in K_{st} causes a proportional decrease of the magnitude of the frequency response in the lower frequency range ($\omega < 5 \text{ rad s}^{-1}$). However, at $\omega > 10 \text{ rad s}^{-1}$, the increased natural frequency due to the increased stiffness increases the response at these higher frequencies. Therefore, it might be worthwhile to consider increasing I_{st} as well to maintain equal natural frequency. This would mean that the relative damping (ζ_{st} , see Table 4.3) would decrease resulting in a peak in the magnitude at the natural frequency.

Between $K_{st} = 0.5 \text{ N m rad}^{-1}$ and 8 N m rad^{-1} the lower frequency response magnitude changes proportionally $\frac{1}{4} \approx -12 \text{ dB}$

7.2.2. Compensating Stiffness with Damping and Inertia

In order to prevent unwanted effects from changing dynamics due to changing natural frequency and damping ratio shown in Figure 7.2, a proportional increase of all stick parameters (K_{st} , B_{st} and I_{st}) together could possibly show a more clear effect of changing the stick dynamics. This would thus be a better comparison to allow the pilot to perform the control task more abased on force perception and less using position perception. In Figure 7.3, the effect of multiplying all stick parameters by the same factor is shown to be equal to multiplying the stick dynamics by a static gain equal to the reciprocal of that factor. When this is done, the consequent values of ω_{0st} and ζ_{st} will remain set to their original value in Table 4.3. This means that the magnitude of the frequency response of the stick will be changed by the same factor for all frequencies. This joint variation of the stick parameters ensures that the phase of the frequency response of the stick remains unchanged. Figure 7.4a shows the wanted effects from increasing the stick stiffness. But Figure 7.4b shows the same effect can be observed when K_{st} , B_{st} and I_{st} are varied together. This variation of stick dynamics can thus be used similarly with the benefit of preventing any unexpected effect of changing stick dynamics.

From this point forward in this thesis, when an increase in stick stiffness is discussed, this implies the joint variation of K_{st} , B_{st} and I_{st} . This will be done with a lower bound of $K_{st} = 0.53 \text{ N m rad}^{-1}$. This is because when $K_{st} < 0.53 \text{ N m rad}^{-1}$ and B_{st} and I_{st} are proportionally changed with this, the tracking task becomes unstable. An upper bound for the stick stiffness is set to 8 N m rad^{-1} . Selecting a wider range of stick settings will likely make it impossible to draw worthwhile conclusions. Furthermore, when $K_{st} > 8 \text{ N m rad}^{-1}$, one should start to consider resulting implications on the pilots physical fatigue since this stiffness will be require the pilot to exert forces which can become exhausting even over one 90s experiment run.

7.2.3. Effects on Stability

In general, it can be stated that an increased stick stiffness will lead to a more stable pilot model. This is logical from a physical standpoint but is also quantifiable by assessing the stability regions shown previously in Figure 6.2 at different stick settings. This is done for $K_{st} = 1 \text{ N m rad}^{-1}$ and $K_{st} = 4 \text{ N m rad}^{-1}$. The results in Figures 7.6 and 7.7 consistently show that a stiffer stick will lead to larger allowed variations of the proprioceptive feedback gains K_p , K_v and K_f whilst maintaining a stable pilot model, both open loop as well as in the closed loop tracking task. Figure 7.5 shows how changing

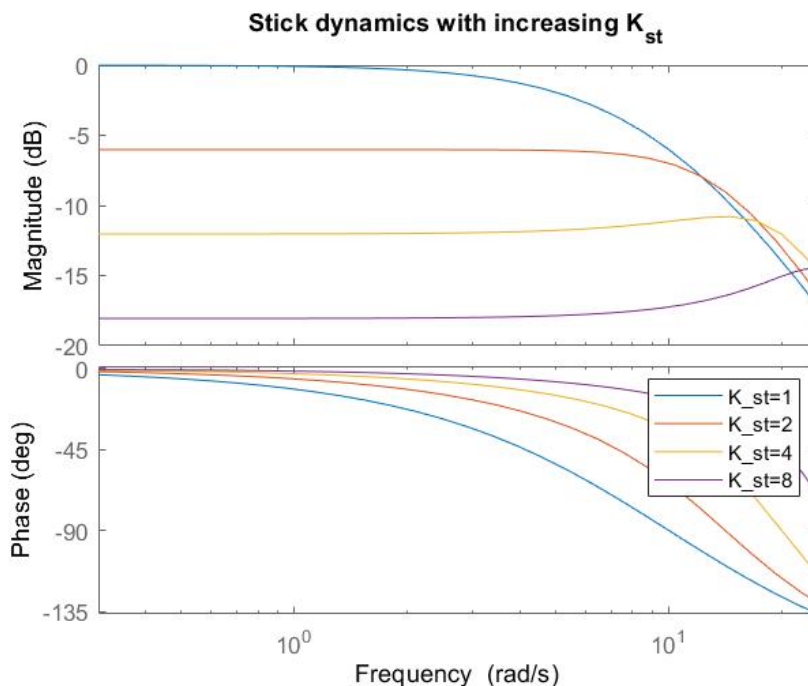


Figure 7.2: Stick dynamics (H_{st}) with variation of K_{st}

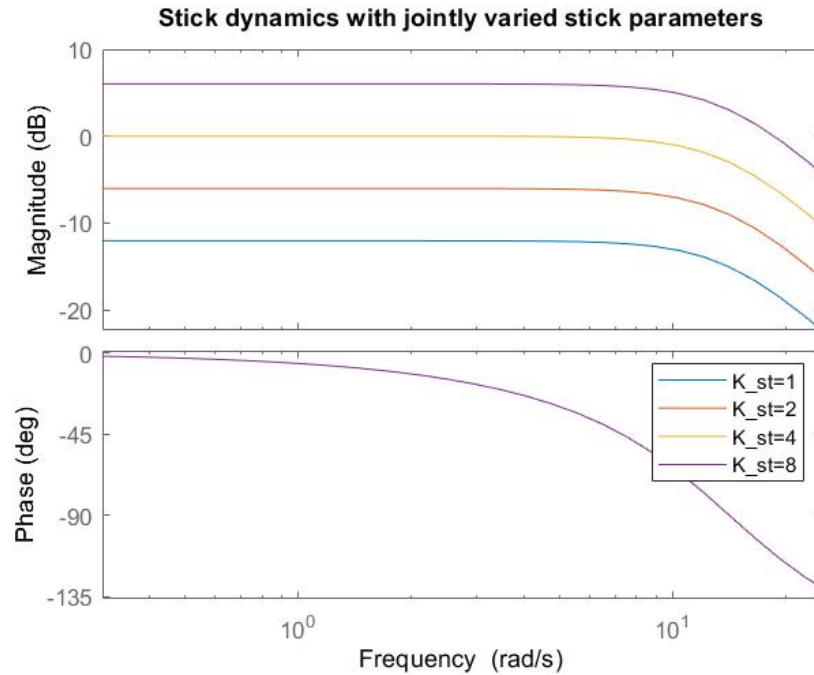
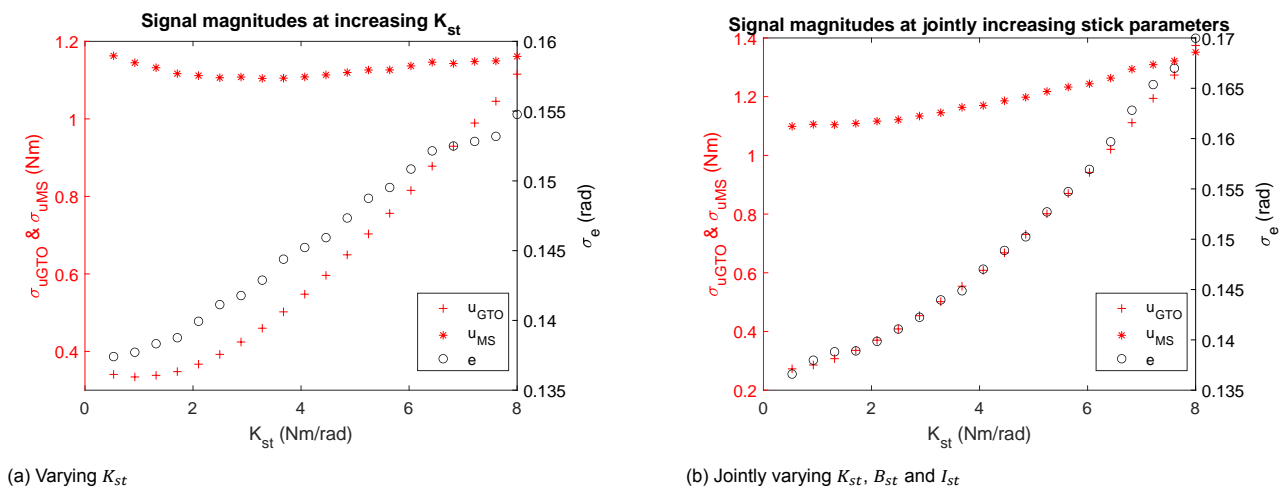


Figure 7.3: Stick dynamics (H_{st}) with joint variation of K_{st} , B_{st} and I_{st}

stick dynamics affect the frequency response of the feedback signals of the Golgi tendon organ and muscle spindles. These plots confirm the changing stability margins between stick settings that lead to instabilities discussed in Chapter 6.

7.2.4. Effects on Performance

When the stick is changed from very light to very heavy dynamics as done for the results in Figure 7.4b, the following conclusions can be drawn regarding the performance. An increased stick stiffness causes a deterioration of the tracking performance and results in a higher magnitude of the GTO feedback signal and no significant change of the MS feedback signal. At first glance this does not seem to imply that better force measurement is used efficiently by the pilot when the stick stiffness is increased. With a stiffer stick, the GTO feedback signal is stronger so the input to the neuromuscular activation is defined



(a) Varying K_{st}

(b) Jointly varying K_{st} , B_{st} and I_{st}

Figure 7.4: Performance and feedback signal intensities at varying stick settings keeping other model parameters constant

more by force measurement which is supposed to be more accurate. Yet, the pilot performs worse in the tracking task with an increase in σ_{ep} . These conclusions hold for changes of the side stick dynamics without any changes in other parts of the model of the pilot. As specified in Chapter 5, the results in Figure 7.4 were obtained by averaging the results from simulations with 50 different noise realizations.

In Section 7.4, changes that happen in the pilot model caused by changes in the stick dynamics will be discussed. This may be a better representation of how a real pilot would react to changes in stick dynamics.

7.3. Target and Disturbance Signals

A dependency of the tracking performance on three different sets of target (f_t) and disturbance (f_d) signals was clearly shown in previous work [13]. The evident result was that the tracking performance is best with the set of forcing functions at the lower frequencies (BW1) and worst at the highest frequency forcing functions (BW3). These bandwidth conditions are defined with by the corner frequencies in Table 7.1 defined in previous work [13]. These three bandwidths were selected with equal width on a logarithmic scale. Figure 7.8 gives a graphical representation of the magnitude of the forcing functions at different frequencies. For generating the disturbance signal, these magnitudes were scaled by the inverse of the magnitude of the controlled element dynamics to ensure equal task difficulty. The forcing functions were then generated as a sum of ten sinusoids at frequencies between $\sim 0.4 \text{ rad s}^{-1}$ and $\sim 17 \text{ rad s}^{-1}$. The exact description of these forcing functions can be found in the relevant publication [13]. In this thesis, condition BW2 is selected if not mentioned otherwise.

These forcing functions will also be used in this thesis. The result that the tracking error (σ_{ep}) increases with the higher frequency forcing functions is easily checked with the simulated pilot model as reported in Table 7.2. The forcing functions with higher frequencies have higher amplitudes at all frequencies and result in higher signal intensities as well, as reported by the values for σ_{f_t} and σ_{f_d} . This is confirmed by looking at the amplitudes of f_t and f_d reported by Fu. Here, at any of the ten forcing frequencies, the amplitude of f_t and f_d was highest for BW3 and lowest for BW1.

Still, the relative increase of σ_{ep} between bandwidth conditions is larger than that of σ_{f_t} or σ_{f_d} . In order to be more thorough, the forcing functions for BW1 and BW3 were scaled such that σ_{f_t} and σ_{f_d} were equal to the values for BW2. The simulated results in Table 7.2 still showed that the higher frequency forcing functions resulted in worse tracking performance.

Earlier work did include the estimation of the frequency response function of the pilot for different bandwidth forcing functions, and significant changes were reported [13]. In this thesis, this change in frequency response will be attempted to be expressed by changes in model parameters.

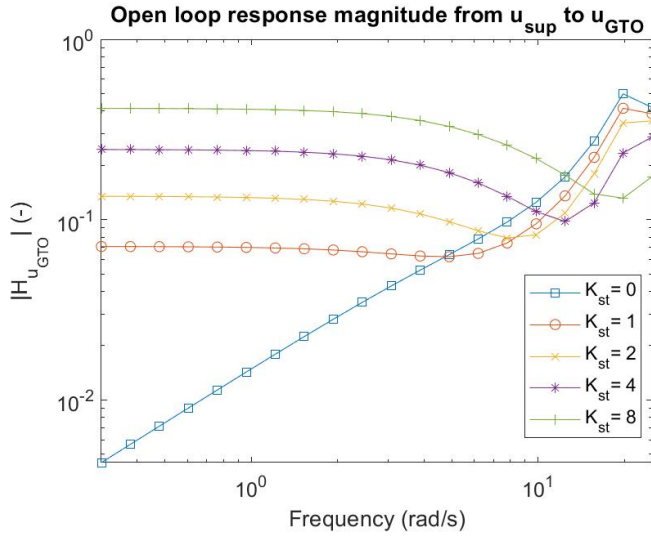
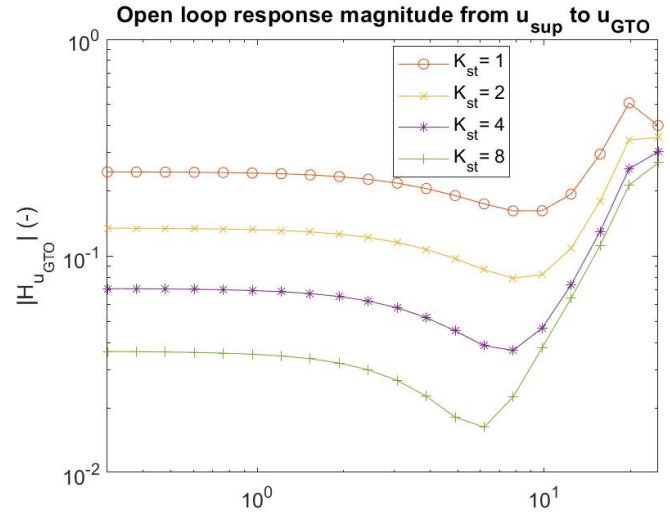
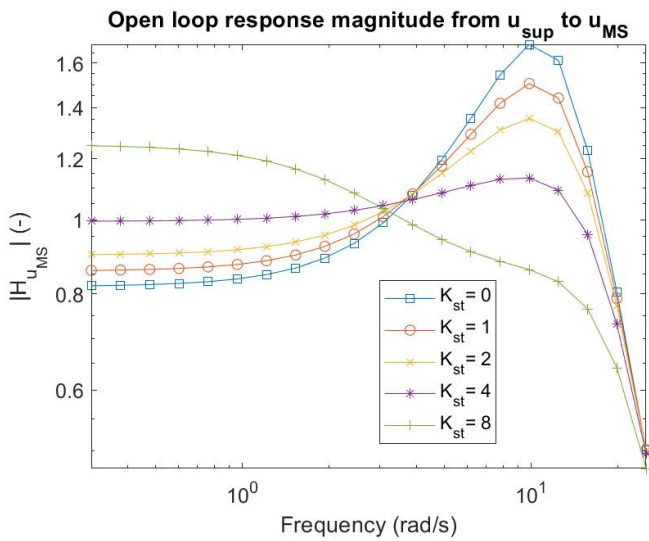
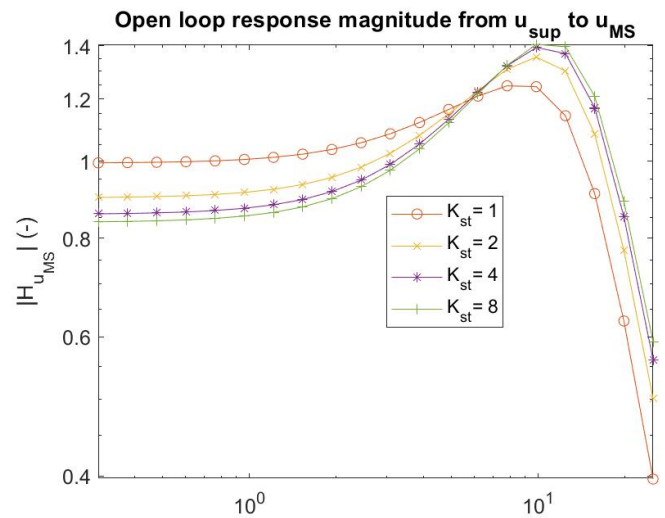
7.4. Pilot Adaptation

Up to this point, only the direct result of variations of one parameter in the model of the tracking task has been considered. That is to say that all other model parameters remain unchanged. It is highly likely that this is not the best representation of what would happen in a real experiment. In all probability, the pilot will adapt to incorporated changes in some way to better perform the tracking task. In previous work, significant pilot adaptation was observed when the side stick parameters were changed [8]. Other research showed that pilot model parameters are also dependent on other control task parameters [16]. Knowledge of how the pilot adapts to parameters in a tracking task is of great relevance for aiding the pilot as well. Pilots have been shown to adapt to different types of haptic support systems in a control task [27]. This suggests that accurate knowledge of pilot adaptation will allow these support systems to be designed more effectively.

Table 2.3 and Table 2.4 of [13]

Table 7.1: Forcing function bandwidth definition

Bandwidth	Lower corner frequency (rad s^{-1})	Higher corner frequency (rad s^{-1})
BW1	0.6	4.8
BW2	1	8
BW3	1.65	13.2

(a) GTO, varying K_{st} (b) GTO, jointly varying K_{st} , B_{st} and I_{st} (c) MS, varying K_{st} (d) MS, jointly varying K_{st} , B_{st} and I_{st} Figure 7.5: Frequency response from u_{sup} to GTO and MS feedback at varying stick settings

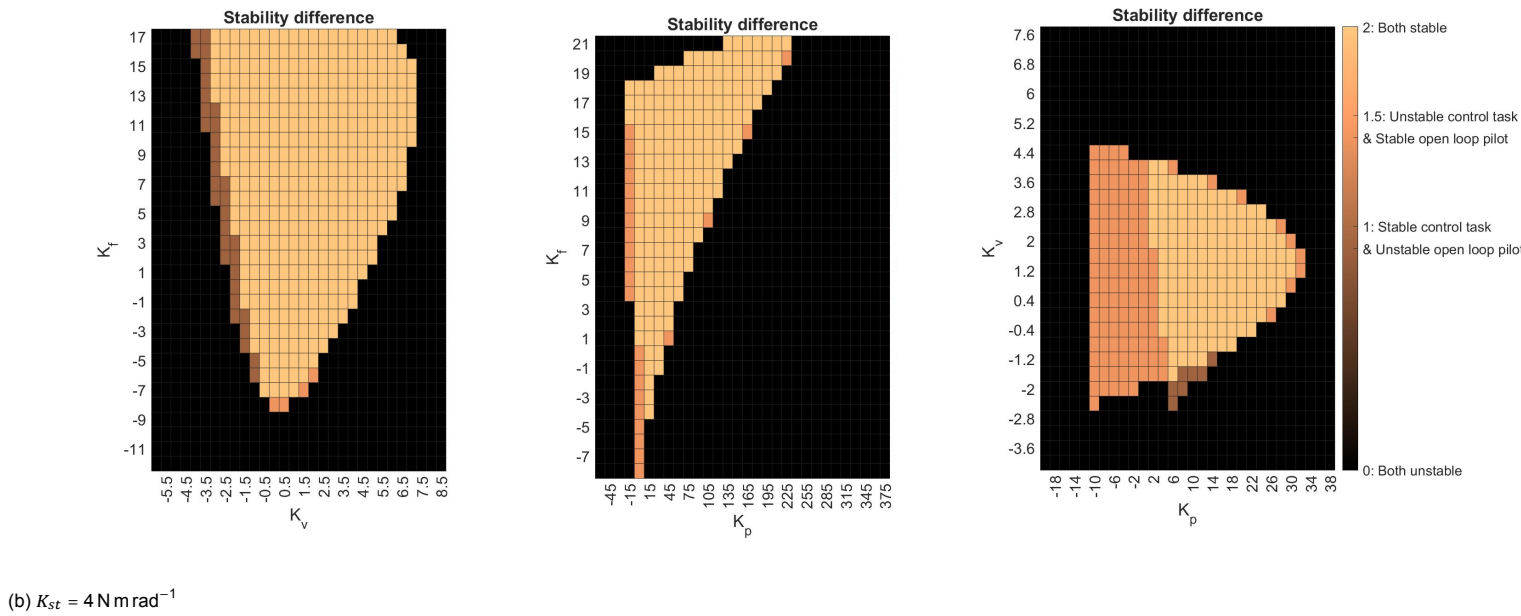
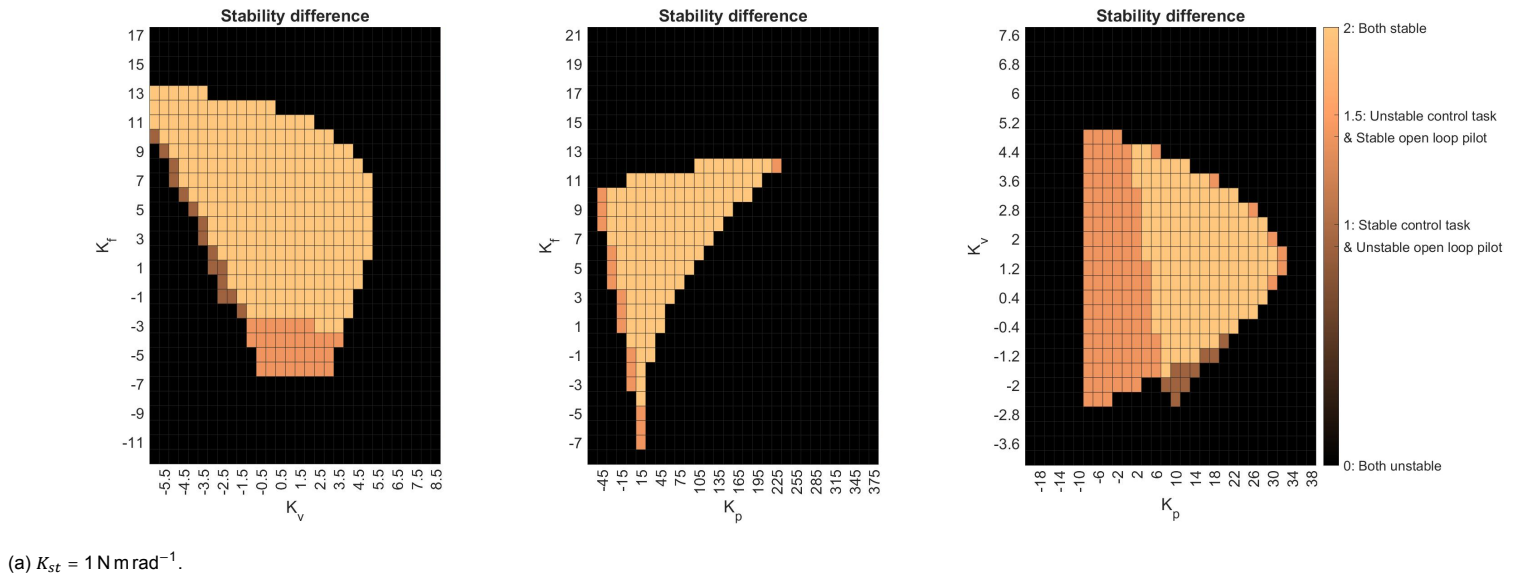


Figure 7.6: Stability regions for K_p , K_v and K_f 'Sliced' at proprioceptive gains according to FT (see Table 4.2) (from left to right: $K_p = 9 \text{ N m rad}^{-1}$, $K_v = 2 \text{ N m s rad}^{-1}$ and $K_f = -1.5$) with different values for K_{st}

This section will explore pilot adaptation in the simulated environment aiming to make predictions with respect to a real tracking experiment. Predicting how the detailed pilot model that is considered for this thesis will adapt to experiment settings is expected to be challenging to do based on only simulation of a model. Dependency of parameters in this model on experiment settings are not known. This means the changes of these parameters have to be approximated in some way. These approximation should be considered only that, until they are validated in an experiment.

7.4.1. Cognitive Response

The cognitive inputs the pilot gives to his muscles represented by H_6 in Table 4.1. This supraspinal input (u_{sup}) is determined by the cognitive response of the pilot modelled in this thesis by a PID controller. One can expect these cognitive dynamics to change when the stick dynamics are changed. The pilot

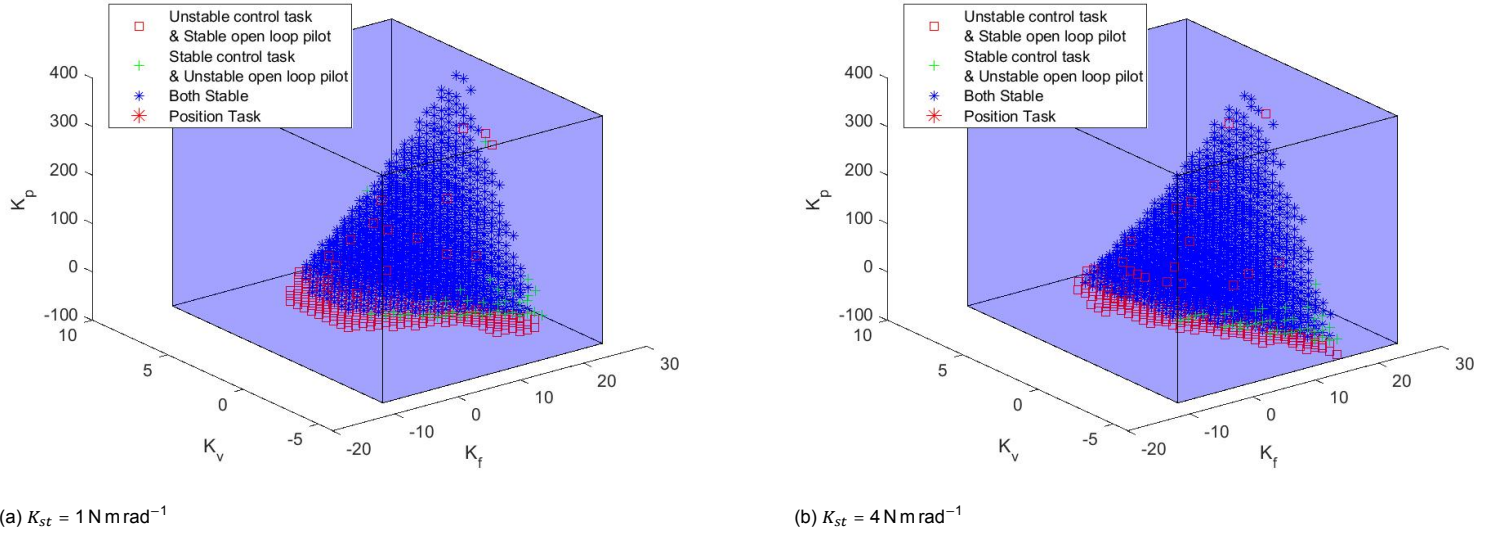


Figure 7.7: Isometric view of stable regions for K_p , K_v and K_f with different values for K_{st}

Table 7.2: Tracking performance and forcing function intensity at three BW conditions

Bandwidth	σ_e (rad)	σ_e (rad) with forcing functions scaled to BW2	σ_{f_t} (rad)	σ_{f_d} (rad)
BW1	0.0815	0.0821	0.1506	0.1260
BW2	0.1400	"	0.1936	0.1339
BW3	0.2733	0.2720	0.2255	0.1771

performing the tracking task would feel that the stick needs more force to be moved when the stick is stiffer. By this analogy, one would thus expect to observe an increased P_e for an optimally tuned PID controller. This optimally tuned PID is approximated by finding P_e , I_e and D_e that minimize σ_{e_p} using a search algorithm. Figure 7.11 shows how this cognitive response changes when the stick dynamics are changed. The PID settings that result in the minimal σ_{e_p} are found and presented. From this figure, it is clear that for this particular tracking task and controlled element the pilot does not have to cognitively act as an integrator since $I_e = 0$ for any stick setting. The dynamics of the controlled element defined in Table 4.1 and illustrated by Figure 7.10 show a negative slope equal to 1, which according to theory in manual control [24], is the preferred slope in the crossover region. Consequently, the tracking task with this controlled element does not require the pilot to act as an integrator making the tracking task cognitively easy. The most difficult controlled elements pilots can handle have been studied in the past [19]. When comparing the controlled element for this thesis to those, it becomes clear that the considered controlled element indeed can be regarded easily controllable.

Figure 7.11 does not confirm the expectation that P_e immediately increases with K_{st} . To see why this is, the dynamics of the pilot model from u_{sup} to u_p , shown in Figure 7.9 gives an explanation. First of all, a significant variation in the stick parameters only makes a marginal change in the open loop dynamics of the entire pilot, control device and controlled element together. The way to achieve the best closed loop performance is for the magnitude of the dynamics to equal one at the target frequencies. An increase of P_e would cause a proportional increase of the magnitude of the open loop dynamics ($|H_{OL}|$) over all frequencies. However, an increase in $|H_{OL}|$ at higher frequencies may compensate better for a heavier stick than at low frequencies. This can only be done by increasing D_e . Hence, the prediction that the pilot adapts to an increase of K_{st} by increasing P_e is too simple and inaccurate. Still the better conclusion from this plot and the observed changes in optimal PID settings is that it is probably worthwhile to use available tools to find the PID settings that best represent the actual pilot's cognitive processes. This is because the considered system has a high degree of complexity.

It was also attempted to tune the cognitive response PID controller using classical Zeigler–Nichols tuning [25]. This gave inferior results compared to the search algorithm discussed earlier and will thus

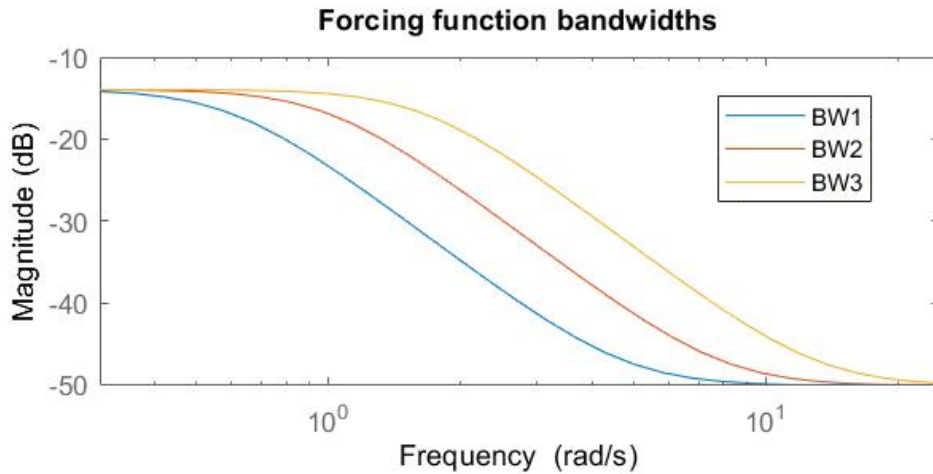


Figure 7.8: Definition of forcing function magnitudes

not be explored going forward. This worse performance is not surprising since heuristic methods are adopted regularly for PID-tuning. Optimal PID parameters are often found using complex methods [28].

The method that lead to the results in Figure 7.11 was performed at increasing stick settings to find out if any maximum limit for K_{st} exists. An upper limit for K_{st} was found, which, if exceeded, made the pilot model unable to perform the control task with $\sigma_e \gg 1$. A limit was found at $K_{st} > 45 \text{ N m rad}^{-1}$ when all stick parameters were varied together. This value was 65 N m rad^{-1} when only K_{st} was increased and 22 N m rad^{-1} when the PID settings were left to their original from Table 4.2. The implication is that the way pilot adaptation is modeled in this section allows an unstable configuration to be resolved. When

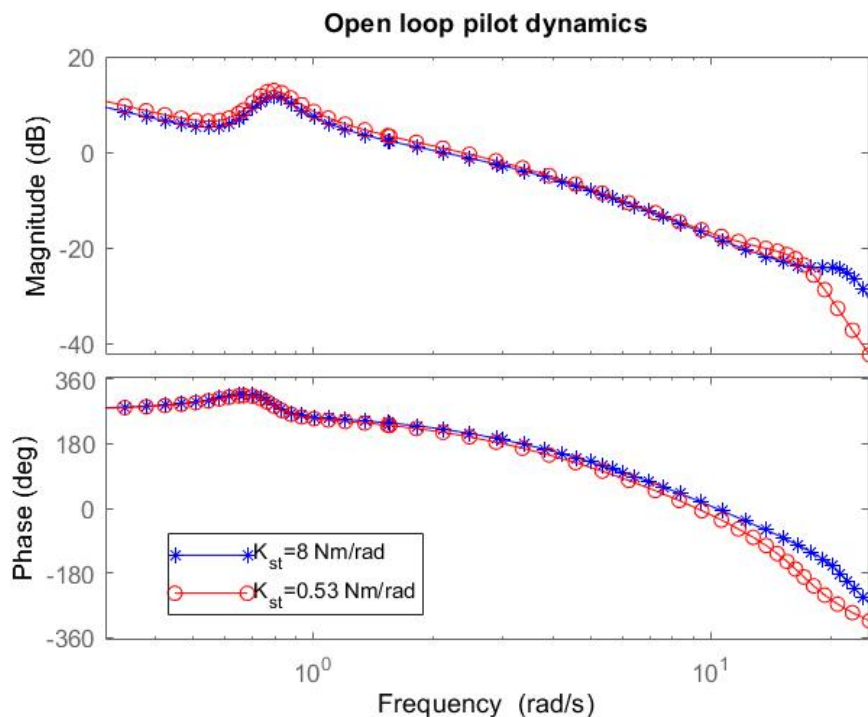


Figure 7.9: Open loop pilot dynamics from e to ϕ with very light and very heavy side stick dynamics

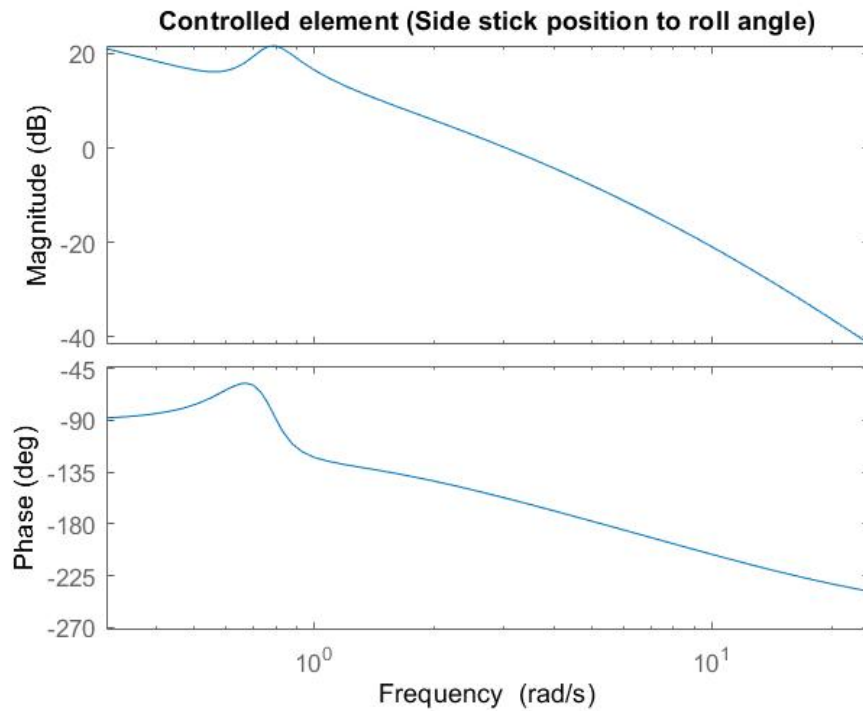


Figure 7.10: Controlled element dynamics defined in Chapter 4

the cognitive response parameters in combination with the task settings initially lead to an unstable control task with $\sigma_e \gg 1$, the algorithm is able to 'escape' this infeasible combination of parameters.

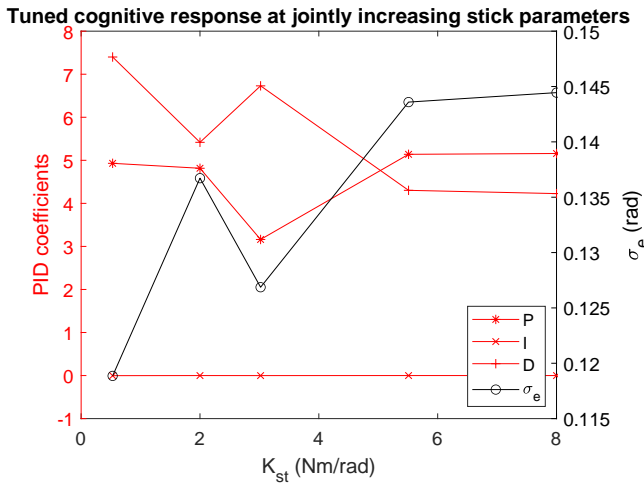
7.4.2. Proprioceptive Feedback

The proprioceptive feedback gains K_p , K_v and K_f are assumed to be task specific in the sense that they differ between the position task, force task and relax task [3]. This leads to the concept that they may as well be dependent on other task parameters such as K_{st} or forcing function bandwidth. Changing these task parameters does not change the fact that we are dealing with a position task, but could have an effect on the exact values of parameters in the model of the pilot. This leads to a set of hypotheses defined in Table 7.4

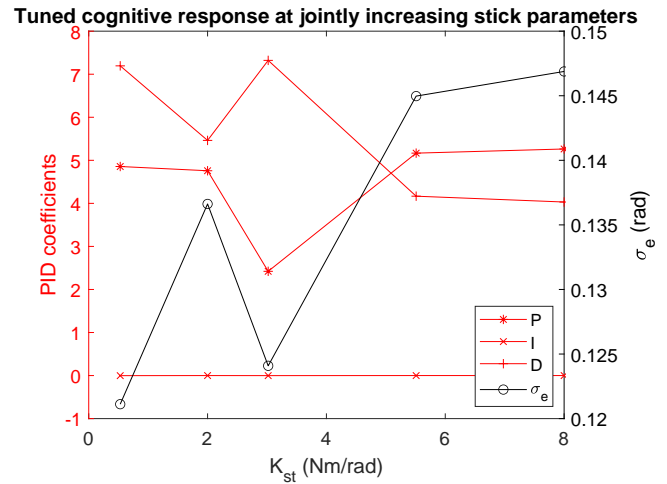
7.4.3. Parameter Dependency

In order to test the stated hypotheses, a search algorithm is used to find the set of parameters P_e , I_e , D_e , K_p , K_v and K_f that minimize σ_{ep} . It would be interesting to see the tracking performance's sensitivity to changes in any of these parameters. Hypothetically, this could be achieved with heatmaps or contour plots similar to those made for stability conditions discussed in Chapter 6. However for several reasons this is not efficient for examining tracking performance. The first reason is that there are now six parameters instead of three to consider making a graphical presentation with heatmaps impractical. Also, the scalar σ_{ep} cannot be visualized in a three dimensional plot as was possible for degrees of stability in Figure 6.3. This could possibly be solved by categorizing tracking performance with a small number of ranges for the value of σ_{ep} . The most important drawback however is that evaluating the tracking performance requires simulation of the tracking task. This much more computationally expensive than only determining the stability which was needed for the results in Chapter 6.

For those reasons, a search algorithm is the more efficient and preferred method to assess the relation between the pilot model parameters (P_e , I_e , D_e , K_p , K_v and K_f) and the tracking performance. The algorithm has tolerances of 0.001 rad for σ_{ep} and 0.5 for the pilot model parameters. This ensures that the search algorithm stops when in the last step, both the improvement of σ_{ep} was smaller than 0.001 rad and changes in any of the pilot model parameters (P_e , I_e , D_e , K_p , K_v and K_f) were smaller than 0.5. These boundaries are set because any narrower search is likely to overfit separately to

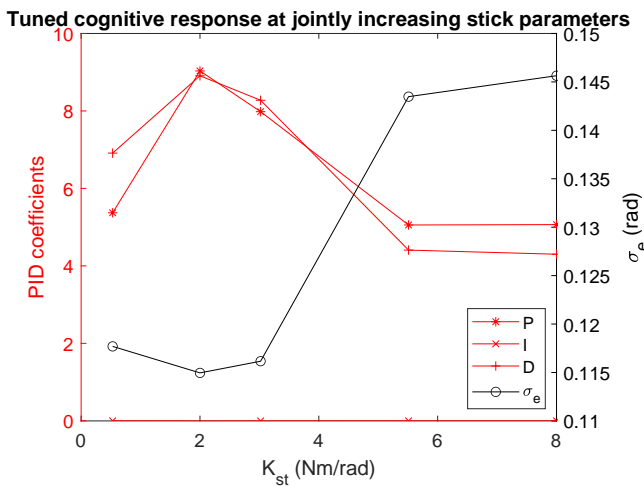


(a) Varying K_{st}

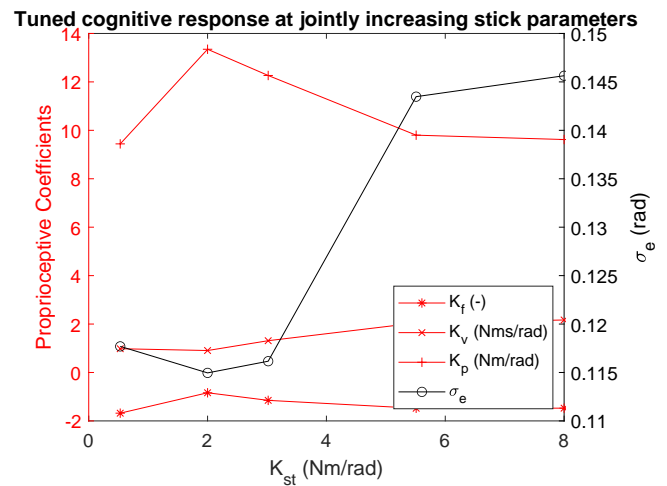


(b) Jointly varying K_{st} , B_{st} and I_{st}

Figure 7.11: Optimized cognitive dynamics (P_e , I_e and D_e) with changing stick dynamics



(a) Cognitive response PID parameters



(b) Proprioceptive feedback parameters

Figure 7.12: Tuned pilot model parameters (P_e , I_e , D_e , K_p , K_v and K_f) with changing stick dynamics at BW2 forcing functions

each of the 50 different noise realizations (on m_{refl}) and the exact forcing functions used. With a free search algorithm, the possibility of variable attaining unreasonable values should be avoided. Hence the results can lead to unreasonable outcomes. When this occurs they should be treated with care.

This algorithm is executed at the three bandwidth conditions defined earlier and at varying stick parameters as defined earlier in this section. The outcome of this algorithm is vector of seven values (the tracking performance followed by the six model parameters). When changes between different bandwidth conditions or stick parameters lead to significant changes of any pilot model parameter (σ_{ep} , $\sigma_{u_{GTO}}$, $\sigma_{u_{MS}}$, P_e , I_e , D_e , K_p , K_v or K_f), the null hypothesis of this parameter can be rejected in favor of one of the three alternative hypotheses. Only when the null hypothesis of a particular pilot model parameter is rejected, will any search for a quantitative definition of its dependency be meaningful. For now, only simulated data are used, meaning that performing statistical analysis to see the statistical significance of any observed differences is not yet needed. When the experiments are performed, statistical analysis of the results will be needed to interpret the results properly.

Figure 7.12 shows the results of the algorithm when the stick dynamics are varied. It is clear that, similar to what was suggested before when pilot model parameters were not tuned, σ_{ep} increases with stick stiffness. This recurring conclusion is contrary to the conclusion reported in previous work [7].

Using the described search algorithm above does assume that the pilot would be able to adapt

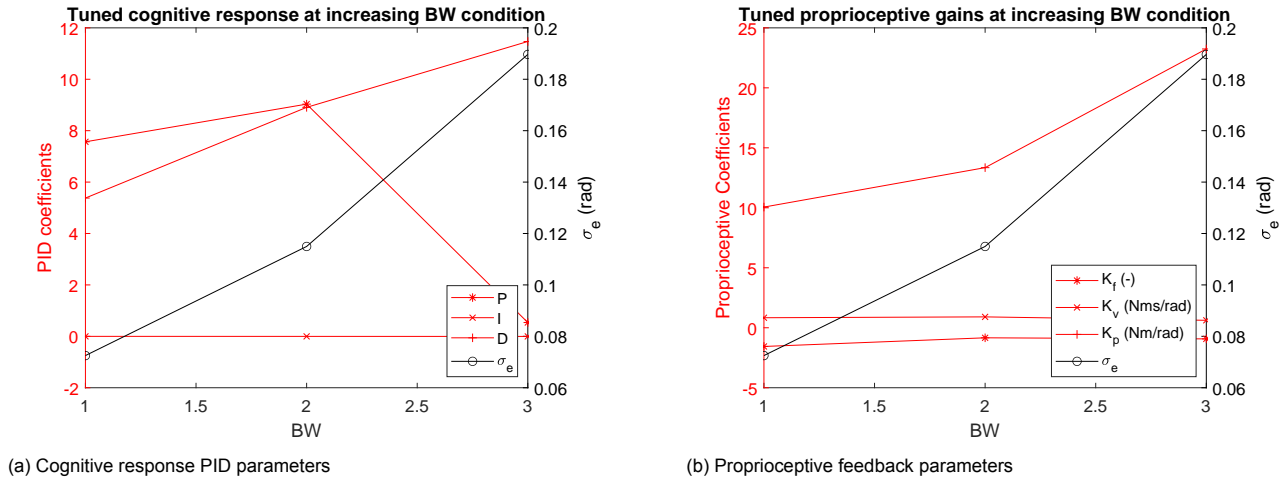


Figure 7.13: Tuned pilot model parameters (P_e , I_e , D_e , K_p , K_v and K_f) with different forcing functions

Table 7.3: Tuned pilot model parameters at $K_{st} = 0$, $B_{st} = 0.053 \text{ N m rad}^{-1}$ and $I_{st} = 0.00265 \text{ N m rad}^{-1}$

Symbol	Value
σ_{ep}	0.118 rad
P_e	5
I_e	0
D_e	7
K_p	9 N m rad^{-1}
K_v	$0.9 \text{ N m s rad}^{-1}$
K_f	-1.8

optimally to the imposed task settings. In reality, this is limited by the boundaries on the pilot model parameters. It could well be that the actual pilot is not able to select the perfect combination of the six model parameters as well as the search algorithm can. It should thus be noted that in a real experiment, the same outcome is not guaranteed.

Figure 7.12 shows how tracking performance behaves when the stick parameters K_{st} , I_{st} and B_{st} are jointly varied. Here, the tracking performance becomes worse with increased stick stiffness. In this plot the condition of $K_{st} = 0$ is not included because the corresponding $I_{st} = 0$ would be infeasible. Still the condition of $K_{st} = 0$ is of interest because this would require the pilot to perform the control task whilst only knowing the center position of the stick with position sensing. The pilot would not have any force due to K_{st} to help determining what position of the stick corresponds to no deflection. The search algorithm is executed separately with $K_{st} = 0$, and I_{st} and B_{st} according to the joint variation at $K_{st} = 0.53 \text{ N m rad}^{-1}$. This leads to the results in Table 7.3. This shows that tracking performance with zero stick stiffness is worse than performance with $K_{st} = 0.53 \text{ N m rad}^{-1}$ to $3.02 \text{ N m rad}^{-1}$. This is according to expectations since with $K_{st} = 0$ the pilot has to rely much more on the muscle spindles than on the Golgi tendon organs and MS have been shown to have worse accuracy in Chapter 3. When $K_{st} = 5.51 \text{ N m rad}^{-1}$ to 8 N m rad^{-1} , tracking performance does become worse than for $K_{st} = 0$.

The performed simulations lead to the results in Figures 7.12 and 7.13 and the selection of the hypotheses indicated in blue in Table 7.4. In Figure 7.13, the algorithm found values for D_e , K_p , K_v and K_f that became unreasonably large in magnitude for BW3. It was indicated earlier that such a free search algorithm always has this risk. Therefore the simulated results for BW3 should not be seen as meaningful. Results of tuning the model parameters at BW1 and BW3 may be found in Figures F.1 and F.2.

Table 7.4 implies that I_e , K_v and K_f are assumed to be independent on the varied conditions from this point forward. This conclusion is coherent with previous work [8]. Here K_p was shown to be more dependent on varying stick settings than K_v and K_f . The values of the three parameters identified as independent on the conditions will remain set to their original values defined by previous research. Consequently, using Table 7.4, the pilot model parameters of interest can be reduced to the parameters

Table 7.4: Pilot model signal/parameter dependency hypotheses

Parameter \ Dependent on:	Neither K_{st} nor BW	Only K_{st}	Only BW	Both K_{st} and BW
σ_e (rad)	\mathcal{H}_0^e	\mathcal{H}_K^e	\mathcal{H}_{BW}^e	\mathcal{H}_{KBW}^e
$\sigma_{u_{GTO}}$ (rad)	\mathcal{H}_0^{GTO}	\mathcal{H}_K^{GTO}	\mathcal{H}_{BW}^{GTO}	\mathcal{H}_{KBW}^{GTO}
$\sigma_{u_{MS}}$ (rad)	\mathcal{H}_0^{MS}	\mathcal{H}_K^{MS}	\mathcal{H}_{BW}^{MS}	\mathcal{H}_{KBW}^{MS}
P_e (-)	\mathcal{H}_0^p	\mathcal{H}_K^p	\mathcal{H}_{BW}^p	\mathcal{H}_{KBW}^p
I_e (-)	\mathcal{H}_0^l	\mathcal{H}_K^l	\mathcal{H}_{BW}^l	\mathcal{H}_{KBW}^l
D_e (-)	\mathcal{H}_0^d	\mathcal{H}_K^d	\mathcal{H}_{BW}^d	\mathcal{H}_{KBW}^d
K_p (Nm rad ⁻¹)	\mathcal{H}_0^p	\mathcal{H}_K^p	\mathcal{H}_{BW}^p	\mathcal{H}_{KBW}^p
K_v (Nm s rad ⁻¹)	\mathcal{H}_0^v	\mathcal{H}_K^v	\mathcal{H}_{BW}^v	\mathcal{H}_{KBW}^v
K_f (-)	\mathcal{H}_0^f	\mathcal{H}_K^f	\mathcal{H}_{BW}^f	\mathcal{H}_{KBW}^f

Trends of:	Depending on control task parameter change:	Increasing K_{st}	Increasing BW
K_p (Nm rad ⁻¹)		Increases	Increases
P_e		Decreases	Decreases
D_e		Decreases	Increases

Table 7.5: Expected trends of pilot model parameters of interest with changing task parameters based on fitted parameters (Figures F.1, F.2, 7.12, 7.13 and H.1)

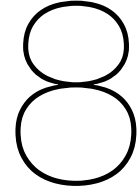
that were identified to have some degree of dependency on either the bandwidth condition, the stick stiffness or both. Those are P_e , D_e and K_p . The ultimate goal of the performed simulations and the to be performed experiment is to prove that when either the bandwidth condition or stick stiffness is changed, these parameters of interest change in a predictable way.

The previously described search algorithm can now be implemented again to only optimize the selected parameters of interest (P_e , D_e and K_p). The results in Figure G.1 illustrate that when tuning P_e , D_e and K_p with a limited number of different noise realizations added to m_{refl} , varying behavior of P_e , D_e can be observed, but K_p remains constant. This suggests that the suggested dependency of P_e and D_e on the control task settings is not as certain as the dependency of K_p . More importantly, and similar to what was already found based on Figure 5.2, Figure G.1 shows that only using five different noise realizations is insufficient, also for the purpose of optimizing the pilot model parameters.

Hence, final fitting of the parameters of interest P_e , D_e and K_p with varied stick settings and bandwidth conditions is performed with 50 different noise realizations, equal to how all other results from simulations in this report were generated. The results are illustrated in Figure H.1. These results can be used to formulate the expectations about the trends of these parameters of interest with changing task parameters that are summarized in Table 7.5. Results from previous fitting of all six pilot model parameters (Figures F.1, F.2, 7.12 and 7.13) were also considered when formulating these expectations. These trends are not exceedingly clear from the simulated results. Hence, observing different behavior in future human-in-the-loop experiments is also conceivable.

In future stages of this thesis, it will be investigated if pilot adaptation to BW condition and stick settings is accurately covered by the variation of P_e , D_e and K_p . In theory, these parameters should be able to describe how a pilot changes his control actions when the control task parameters are changed. Still, experimental results could show a trend which would possibly require pilot adaptation to be modelled differently.

The goal of the to be performed experiments discussed in Chapter 8 is to see which control task parameters allow the pilot to exploit the observed better accuracy of force measurement compared to position measurement of the human arm. Afterwards, a comparison can be made between observed trends from the simulations and from human-in-the-loop experiments.



Experiment Design

The expectations based on literature and simulated experiments discussed until this point need to be validated. The proposed experiments will attempt this by measuring the accuracy difference between human force and position measurement (Section 8.1). Subsequently, using similar conditions, a suitable manual control task will be performed as discussed in Section 8.2. This should allow the effects in a manual control task of the measured difference in human proprioceptive accuracy to be revealed.

8.1. Experiment 1: JND Measurement

In Chapter 2, previous research that found that human force measurement is more accurate than position measurement was discussed. In order to further explore this outcome, the experiment is planned to be reproduced for a range of different conditions in addition to those that were already performed as reported in Table 2.1. This will be done by selecting $K_{St} = 2 \text{ N m rad}^{-1}$, 3.5 N m rad^{-1} and 5 N m rad^{-1} , whilst keeping the reference displacement the same at $\delta_r = 0.37 \text{ rad}$ and appropriately changing the reference torque according to $T_r = \delta_r K_r$. In this way, it can be determined if Weber's law [11] holds for this experiment with the visual display of target torque or position. Weber's law says that in human perception, the JND is a constant fraction of the reference stimulus. According to this, when the experiment is repeated at the suggested values for K_r , a constant Weber fraction of approximately 8% is expected for the force JND and 15% is expected for the position JND. In order to see if Weber's law also holds for different magnitudes of the side stick deflection (δ_r) will be varied as well. The reference displacement will be set to two values. The original value of 0.37 rad is kept and a second condition will have a 50% lower reference deflection of 0.25 rad . The experiment to determine the force JND and position JND will follow the staircase procedure reported earlier [13]. In summary, with this procedure, the subject is asked to report if the stick with the reference stiffness (K_r) or the stick with the controlled stiffness ($K_r = K_c + \delta K$, $\delta K > 0$) felt stiffer. If the correct answer is given, the difference between K_r and K_c (δK) is reduced. If the incorrect stick is selected δK is increased. This converges to the just noticeable difference (JND) as a percentage defined by Eq. (8.1). Here, W_K is the Weber fraction which is constant according to Weber's law. As stated earlier, this fraction is expected to be dependent on the way the participant discriminates the stiffness.

$$W_K = \frac{\delta K_{JND}}{K_r} \quad (8.1)$$

This leads to the proposed experiment matrix reported in Table 8.1 with a total of six different conditions.

Table 8.1: Experiment matrix for JND experiment

δ_r (rad)	K_r (N m rad ⁻¹)	2	3.5	5
0.25		δlKl	δlKm	δlKh
0.37		δhKl	δhKm	δhKh

After the experiments are performed at these conditions, six sets of Weber fractions for force JND and position JND will be deduced from the data. These Weber fractions can then be used to conclude if any difference between position sensing accuracy compared to force sensing accuracy exists and for which conditions.

8.1.1. Hypothesis

W_K is expected to be lower when stiffness discrimination is based on force than when it is based on position. This means that in general, the measured force JND is expected to be lower than the position JND. This expectation is based on previous research documented in Chapter 2. This research also reported constant Weber fractions at different reference stiffnesses. This is also to be expected for the JND experiment performed for this thesis. It is more likely that changes in the reference deflection will have an effect on the measured Weber fractions. When a the participant is instructed to move the stick to a smaller deflection, one can expect this to cause worse performance in discriminating the stick stiffness setting.

8.2. Experiment 2: Control Task

With the expectations from Section 8.1, one can make several predictions on the effect this may have on a manual control task. This experiment intends to show how varying conditions affect the activity of the Golgi tendon organ and muscle spindles. For now this control task is assumed to be a compensatory tracking task with a side stick, because this tracking experiment has been shown to be possible to approximate with simple dynamics. For preview tracking, these simple models do not hold [24].

With the independent variables outlined below, the experiment matrix is as defined by Table 8.2. It may be worthwhile to consider scaling the forcing functions to obtain equal σ_{f_t} and σ_{f_d} between BW1, BW2 and BW3. This was explored earlier with simulations reported in Table 7.2.

Independent variables:

- K_{st}
- I_{st}, B_{st} (with K_{st})
- f_t and f_d spectrum
- Deteriorate known δ_0
 - 1 with low frequency component in f_d
 - 2 by slowly moving the physical position of δ_0 (to which the stick moves back under no applied force) with an unknown forcing function.

The stick stiffness settings of the first experiment in Table 8.1 are repeated here. B_{st} and I_{st} are jointly varied with K_{st} as was done before in simulation introduced in Section 7.2.2. For $K_{st} = 0$ (BW1K0, BW2K0 and BW3K0), equal settings as those for simulated results in Table 7.3 are used, i.e., $B_{st} = 0.053 \text{ N m rad}^{-1}$ and $I_{st} = 0.00265 \text{ N m rad}^{-1}$. The variation of K_{st} is selected to allow direct comparison at equal stick conditions. It can then be shown of a possibly different measured JND for force or position at a given K_r , leads to measurable effects in a control task.

A possible expansion to the forcing function bandwidths can be added. This thesis is primarily concerned with showing the effect of inferior human haptic perception of position compared to force. A possible new set of forcing functions can be generated to see the consequence of this performance

Table 8.2: Experiment matrix for control task experiment

Forcing function bandwidth	$K_{st}(\text{N m rad}^{-1})$	0	2	3.5	5
	BW1		BW1K0	BW1Kl	BW1Km
BW2		BW2K0	BW2Kl	BW2Km	BW2Kh
BW3		BW3K0	BW3Kl	BW3Km	BW3Kh

difference in a tracking task. Ideally, this set of forcing functions would have the effect of deteriorating the participants knowledge of the center position of the side stick (δ_0). Figure 7.8 shows that the three sets of forcing functions have approximately equal intensity at the lowest forcing frequency $\sim 0.4 \text{ rad s}^{-1}$. It may be worthwhile to explore the possibility of achieving this deteriorated pilot knowledge of δ_0 by adding a low frequency component to the disturbance signal. This does not actually change δ_0 but would require the pilot to exert a constant force to compensate for this low frequency component. This new set of forcing functions called BW2x would then be a variation on BW2 where a new component is added to the disturbance signal with a lower frequency than the original lowest of 0.4 rad s^{-1} . This is possible with the passive side stick that is dealt with for this thesis. However, if an active stick were used, one could actually move δ_0 causing the stick to move to a position different from the center when the pilot exerts no force on it.

Dependent variables:

- σ_{ep}
- fitted P_e , D_e and K_p
- simulated $\sigma_{u_{GTO}}$ and $\sigma_{u_{MS}}$ with fitted parameters above

It would be desirable to use experiment data to draw conclusions with respect to the proprioceptive feedback signals u_{GTO} and u_{MS} as well as the tracking performance. However, it is impractical to measure the internal feedback signals directly. Nevertheless, they can be simulated after the experiment is performed and pilot model parameters are fitted. One can then make observations on the effects on these feedback signals and with which control task parameters (independent variables) GTO is more or less important than MS. This can be done by demonstrating that the magnitude of the Golgi tendon organ feedback signal (u_{GTO}) becomes relatively bigger in magnitude compared to that of the muscle spindle (u_{MS}). If the results would clearly show that tracking performance improves when GTO is dominant, this could be an indication of the effect in a control task of GTO's better accuracy.

The tracking performance can obviously be measured directly in the experiment and it will be curious to see if the unexpected result from simulations will also occur in the experiments. Simulations showed a worse performance with a stiffer stick, contradicting what was found in literature about past experiments.

8.2.1. Parameter Estimation

After the experiment is performed, the parameters that define the discussed model from Chapter 4 will be fitted to match the time-domain experiment data. In this thesis, this will be restricted to K_p , P_e and D_e . This means these three variables need to be fitted to make the simulated data match the measured data as best possible. In Chapter 7, some expected changes of K_p , P_e and D_e due to changes in stick settings and forcing functions were formulated in Table 7.5. With experiment data, it will be possible to discover if these changes also appear in reality.

FRF Estimation The two steps of attempting to match the recorded time-domain data with the simulated pilot model by adjusting its parameters can also be done in reverse order. The time-domain data can be used to estimate the pilot model dynamics at the forcing frequencies. The parameters of interest (P_e , D_e and K_p) can then be adjusted to best fit this frequency-domain model.

With the new estimated values for parameters P_e , D_e and K_p , it will be possible to simulate the tracking task again and in particular extract signals u_{MS} and u_{GTO} . These can then be used to draw conclusions about the activity of the muscle spindles and Golgi tendon organs respectively.

8.2.2. Hypothesis

In Chapter 7, simulations were used to show that a stiffer stick (increased K_{st}) or entirely heavier stick (jointly increased K_{st} , B_{st} and I_{st}) causes an increase in the signal magnitude of the Golgi tendon organ feedback. This implies that the pilots controlling actions are more based on the accuracy of the GTO (force JND) than that of the muscle spindles (position JND). However, in the simulation, this did not result in any improvement in the tracking performance. On the contrary, a small performance deterioration (σ_e : $\uparrow \sim 20\%$) was observed when increasing K_{st} between 2 Nm rad^{-1} and 8 Nm rad^{-1} (Figure 7.12). The effects of the same stick stiffness increases did show an improved robustness of the

pilot model in Section 7.2.3 in terms of stability. A stiffer or entirely heavier stick substantially increased the variations in the task dependent pilot model variables K_p , K_v and K_f that still result in a stable closed loop and stable open loop pilot.

Nevertheless, a performance improvement is expected for higher stick stiffness settings. This hypothesis relies on the trend that was shown in literature describing other experiments with varied side stick dynamics.

The performed simulations show consistent results with actual performed experiments from literature with respect to changing forcing function bandwidths. Both, simulations and real experiments showed that forcing functions with higher magnitude of high frequency components cause a higher σ_{ep} , i.e., worse performance. Therefore BW1 is expected to have the best performance and BW3 is predicted to cause the worst performance.

Expectations with respect to signals u_{MS} and u_{GTO} are directly related to the expected changes of K_p . Based on the results from simulations shown in Figures F.1, F.2 and 7.12, K_p is expected to increase both when increasing the stick stiffness and when increasing the forcing function bandwidth condition. Hence, for these conditions, a relative increase in activity of the Golgi tendon organs compared to the muscle spindles is expected. This means that the fraction $\frac{u_{GTO}}{u_{MS}}$ is predicted to increase both for higher BW condition and for heavier stick settings.

9

Conclusion

This preliminary report aimed to explore the differences between a human pilots ability to perceive position and force when using a passive side stick control device. Also an experimental method that can be used to explore the effects this can have in a suitable manual control task was proposed. Literature showed a basis to expect that, at least for limited conditions, humans perceive position with worse accuracy than they perceive force. This difference of uncertainty was reported to be almost a factor two. Other literature showed a more detailed description of the activation of MS and GTO. This lead to the conclusion that they would most efficiently be modelled with a response to muscle length, stretch velocity and force.

A model of the pilot dynamics was used in a computational experiment to explore if any effects on a tracking task can be expected based on this knowledge. One of the conclusions this lead to is that an increased side stick stiffness will cause a pilot to perform a tracking task more based on force perception. This was clear when a stiffer stick caused an increase in magnitude of feedback signal of force perception.

Based on this same pilot model, expectations were made about the dependency of pilot model parameters on task constraints. Simulations suggest that some parts of the pilot model are dependent on the stick settings and forcing functions. More specifically, some components of the proprioceptive feedback loops of the pilot model, as well as part of the cognitive processes of the pilot during the tracking task, are likely affected when the mentioned tracking task parameters are changed.

Finally, a draft experiment plan was formulated which can be used to work out the definitive experiment plan. The first part of this experiment plan is aimed to find any clear difference between performance of human force and position measurement. It also intends to show any clear boundaries for which any possible claims hold. The second part proposes a way to show what effects the results from the first experiment may have on a tracking task. This is specifically concerned with the activity of the Golgi tendon organ and muscle spindles in manual control behavior. The tracking task and its various conditions are defined such that it will be possible to draw conclusions that pertain to the accuracy human of force and position measurement.

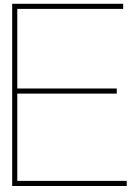
Bibliography

- [1] D. Abbink. *Neuromuscular analysis of haptic gas pedal feedback during car following*. 2006.
- [2] S. Allin, Y. Matsuoka, and R. Klatzky. Measuring just noticeable differences for haptic force feedback: implications for rehabilitation. In *Proceedings 10th Symposium on Haptic Interfaces for Virtual Environment and Teleoperator Systems. HAPTICS 2002*. IEEE Comput. Soc.
- [3] A.K. Bhoelai. Properties of the neuromuscular system identification of intrinsic and proprioceptive components of human, arm dynamics during natural motion control tasks, preliminary master of science thesis.
- [4] M. D. Binder, J. S. Kroin, G. P. Moore, and D. G. Stuart. The response of golgi tendon organs to single motor unit contractions. *The Journal of Physiology*, 271(2):337–349, October 1977.
- [5] D. Burke, K. E. Hagbarth, and L. Löfstedt. Muscle spindle activity in man during shortening and lengthening contractions. *The Journal of Physiology*, 277(1):131–142, April 1978.
- [6] D. Burke, K. E. Hagbarth, L. Löfstedt, and B. G. Wallin. The responses of human muscle spindle endings to vibration of non-contracting muscles. *The Journal of Physiology*, 261(3):673–693, October 1976.
- [7] H. Damveld, D. Abbink, M. Mulder, M. Mulder, M. M. Van Paassen, F. Van der Helm, and R.J. Hosman. Identification of the feedback components of the neuromuscular system in a pitch control task. In *AIAA Modeling and Simulation Technologies Conference*. American Institute of Aeronautics and Astronautics, August 2010.
- [8] E. de Vlugt, A. C. Schouten, and F. C. T. van der Helm. Adaptation of reflexive feedback during arm posture to different environments. *Biological Cybernetics*, 87(1):10–26, July 2002.
- [9] B. B. Edin and A. B. Vallbo. Stretch sensitization of human muscle spindles. *The Journal of Physiology*, 400(1):101–111, June 1988.
- [10] B. B. Edin and A. B. Vallbo. Muscle afferent responses to isometric contractions and relaxations in humans. *Journal of Neurophysiology*, 63(6):1307–1313, June 1990.
- [11] G. Ekman. Weber's law and related functions. *The Journal of Psychology*, 47(2):343–352, April 1959.
- [12] J. B. Fallon and V. G. Macefield. Vibration sensitivity of human muscle spindles and golgi tendon organs. *Muscle & Nerve*, 36(1):21–29, 2007.
- [13] W. Fu. *Evidence-based development and evaluation of haptic interfaces for manual control*. PhD thesis, 2019.
- [14] J. E. Gregory and U. Proske. The responses of golgi tendon organs to stimulation of different combinations of motor units. *The Journal of Physiology*, 295(1):251–262, October 1979.
- [15] G. Heinzl, A. Rüdiger, and R Schilling. Spectrum and spectral density estimation by the discrete fourier transform (dft), including a comprehensive list of window functions and some new flat-top windows. *Max Plank Inst*, 12, 01 2002.
- [16] R. A. Hess. Modeling human pilot adaptation to flight control anomalies and changing task demands. *Journal of Guidance, Control, and Dynamics*, 39(3):655–666, March 2016.
- [17] R. Hosman and J. Vaart. Active and passive side stick controllers: Tracking task performance and pilot control behavior. 09 1987.

- [18] J. Houk and W. Simon. Responses of golgi tendon organs to forces applied to muscle tendon. *Journal of Neurophysiology*, 30(6):1466–1481, November 1967.
- [19] H.R. Jex, J.D. McDonnell, and A.V. Phatak. A "critical" tracking task for manual control research. *IEEE Transactions on Human Factors in Electronics*, HFE-7(4):138–145, December 1966.
- [20] P. A. Kirkwood. The frequency response of frog muscle spindles under various conditions. *The Journal of Physiology*, 222(1):135–160, April 1972.
- [21] D. A. Kistemaker, A. J. Knoek Van Soest, J. D. Wong, I. Kurtzer, and P. L. Gribble. Control of position and movement is simplified by combined muscle spindle and golgi tendon organ feedback. *Journal of Neurophysiology*, 109(4):1126–1139, February 2013.
- [22] Y. Laufer, S. Hocherman, and R. Dickstein. Accuracy of reproducing hand position when using active compared with passive movement. *Physiotherapy Research International*, 6(2):65–75, June 2001.
- [23] P. B. C. Matthews and R. B. Stein. The sensitivity of muscle spindle afferents to small sinusoidal changes of length. *The Journal of Physiology*, 200(3):723–743, February 1969.
- [24] D.T. McRuer and H.R. Jex. A review of quasi-linear pilot models. *IEEE Transactions on Human Factors in Electronics*, HFE-8(3):231–249, September 1967.
- [25] P. M. Meshram and R. G. Kanojiya. Tuning of pid controller using ziegler-nichols method for speed control of dc motor. In *IEEE-International Conference On Advances In Engineering, Science And Management (ICAESM -2012)*, pages 117–122, 2012.
- [26] M. Mulder, D. M. Pool, D. A. Abbink, E. R. Boer, P. M. T. Zaal, F. M. Drop, K. van der El, and M. M. van Paassen. Manual control cybernetics: State-of-the-art and current trends. *IEEE Transactions on Human-Machine Systems*, 48(5):468–485, 2018.
- [27] M. Olivari, F. M. Nieuwenhuizen, H. H. Bülthoff, and L. Pollini. Pilot adaptation to different classes of haptic aids in tracking tasks. *Journal of Guidance, Control, and Dynamics*, 37(6):1741–1753, November 2014.
- [28] S. Pareek, M. Kishnani, and R. Gupta. Optimal tuning of PID controller using meta heuristic algorithms. In *2014 International Conference on Advances in Engineering & Technology Research (ICAETR - 2014)*. IEEE, August 2014.
- [29] M. B. Priestley. *Spectral analysis and time series*. Academic Press, London New York, 1981.
- [30] S. Raychaudhuri. Introduction to monte carlo simulation. In *2008 Winter Simulation Conference*, pages 91–100, 2008.
- [31] H. Z. Tan, N. I. Durlach, G. L. Beauregard, and M. A. Srinivasan. Manual discrimination of compliance using active pinch grasp: The roles of force and work cues. *Perception & Psychophysics*, 57(4):495–510, June 1995.
- [32] R. J. van Beers, A. C. Sittig, and J. J. Denier van der Gon. The precision of proprioceptive position sense. *Experimental Brain Research*, 122(4):367–377, October 1998.
- [33] M. M. van Paasen, J. C. van der Vaart, and J. A. Mulder. Model of the neuromuscular dynamics of the human pilot's arm. *Journal of Aircraft*, 41(6):1482–1490, November 2004.
- [34] M.M. Van Paassen. *Biophysics in aircraft control*. PhD thesis, TU Delft, 1994.
- [35] J. Venrooij, D. A. Abbink, M. Mulder, M. M. van Paassen, M. Mulder, F. C. T. van der Helm, and H. H. Bülthoff. A biodynamic feedthrough model based on neuromuscular principles. *IEEE Transactions on Cybernetics*, 44(7):1141–1154, July 2014.
- [36] G. Warren and Rogers E. Saith. Flight investigation of fighter side-stick force-deflection characteristics. Technical report, CALSPAN CORPORATION, 1975.

IV

Preliminary Research Appendices



Root locus of varying K_p , K_v and K_f

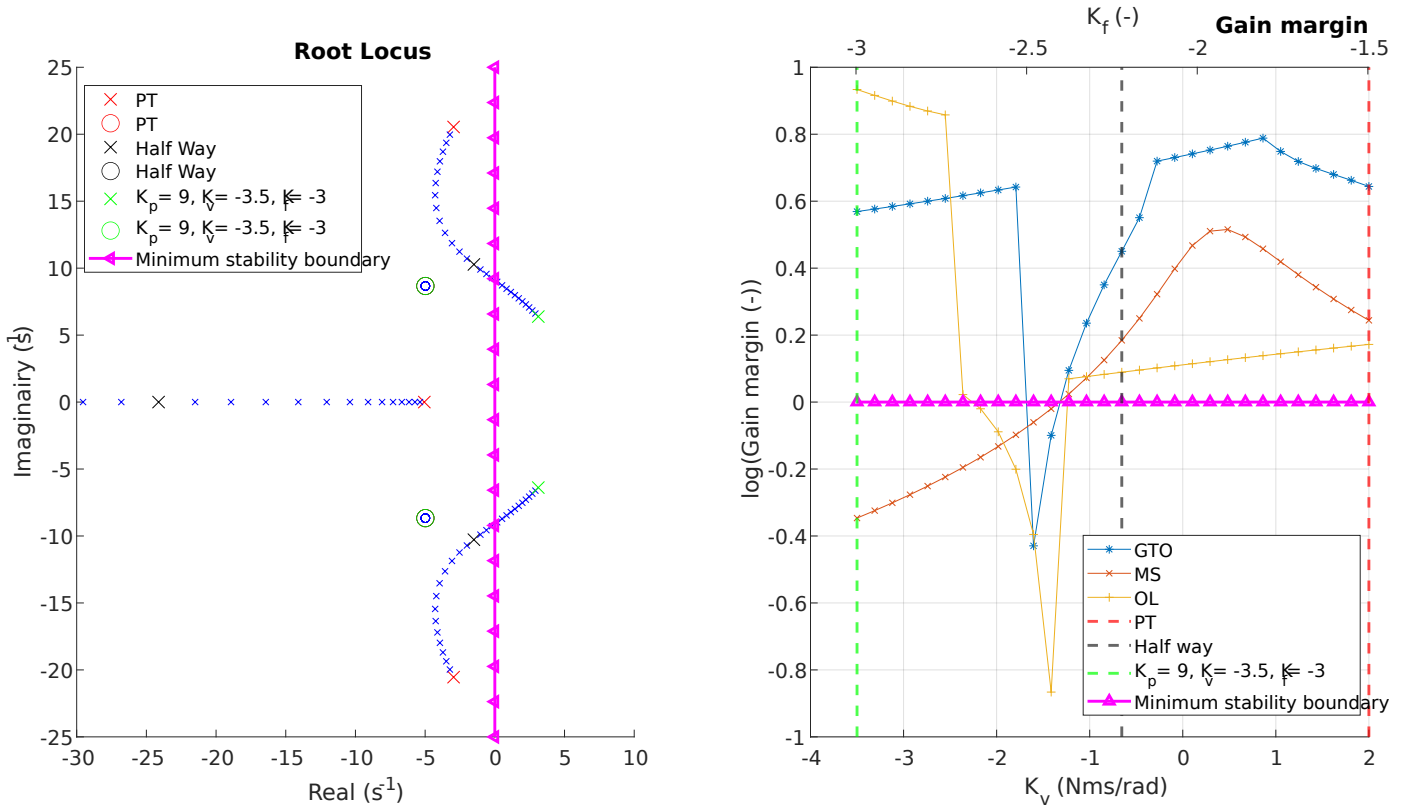


Figure E.1: Root locus of $H_{u_{sup}, m_{mus}}$ at stability boundary due to too small K_f . From PT to A

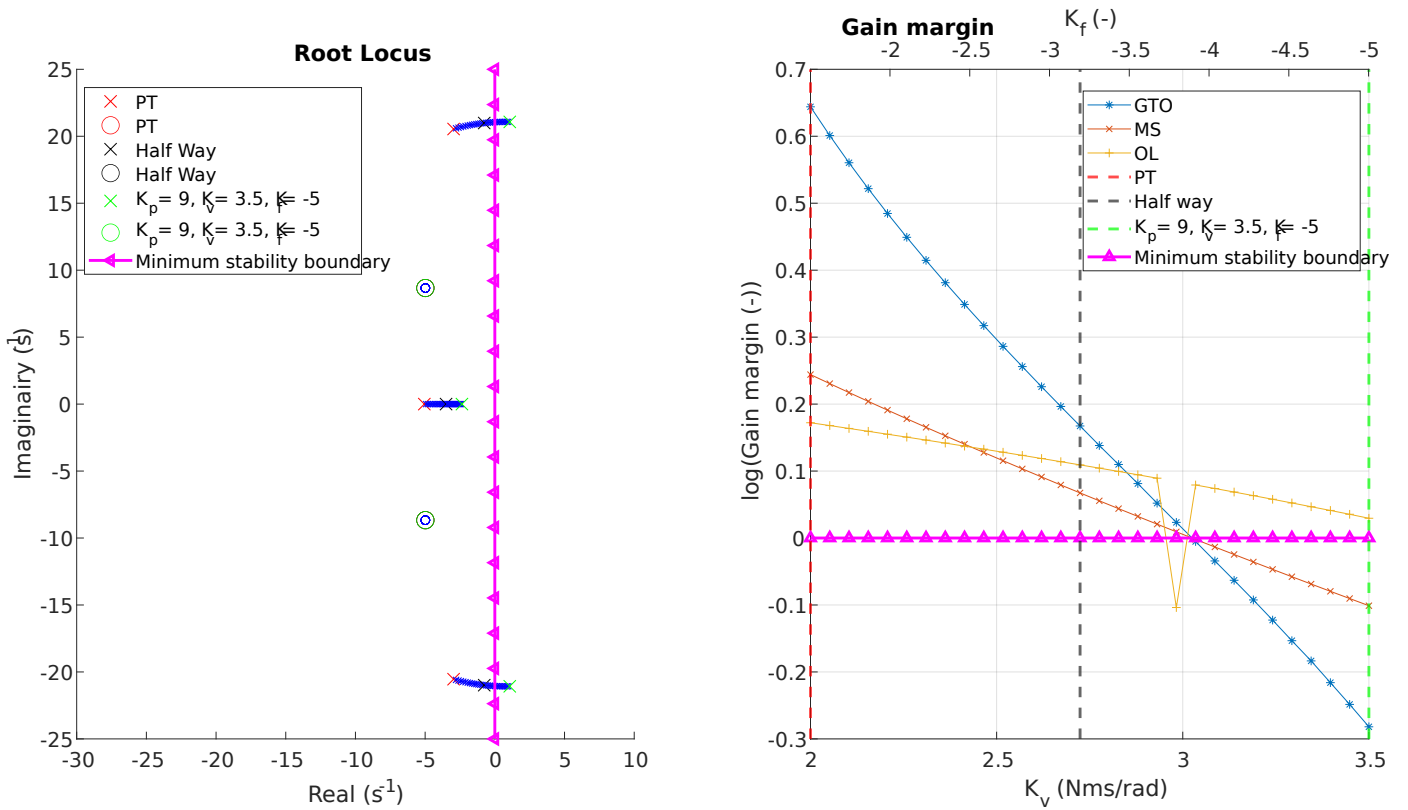


Figure E.2: Root locus of $H_{u_{sup}, m_{mus}}$ at stability boundary due to too large K_f . From PT to B

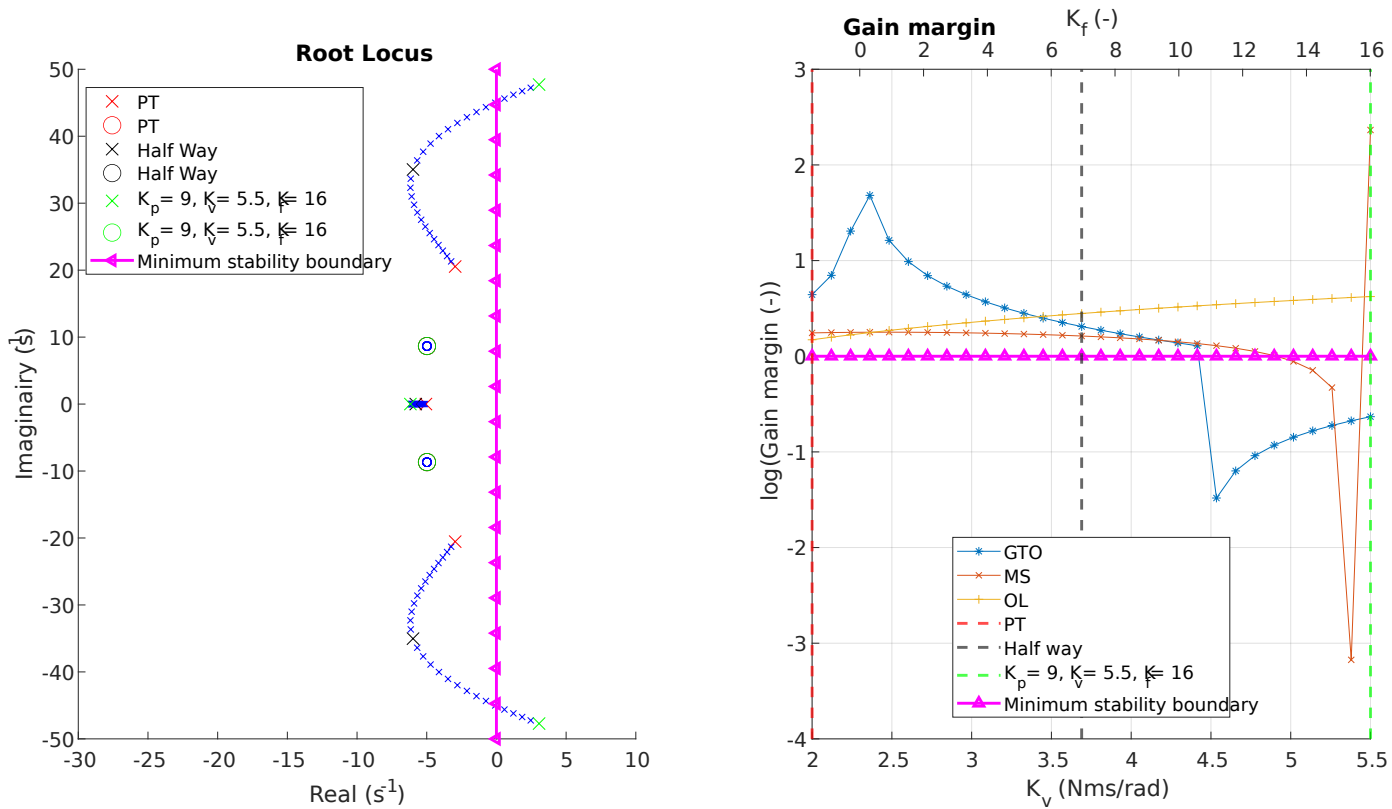


Figure E.3: Root locus of $H_{u,sup,m_{mus}}$ at stability boundary due to too large K_f and large K_v . From PT to C

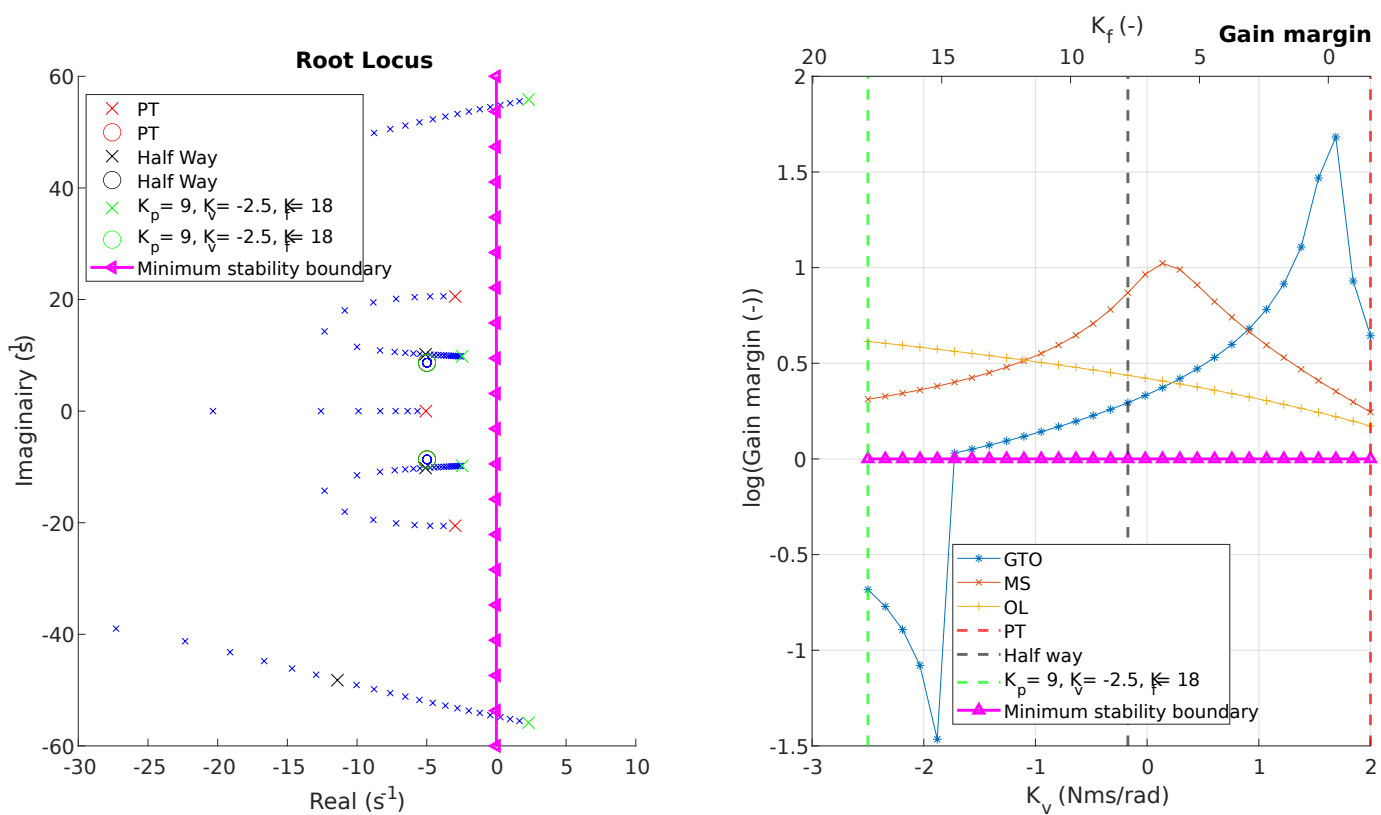


Figure E.4: Root locus of $H_{u,sup,m_{mus}}$ at stability boundary due to too large K_v . From PT to D

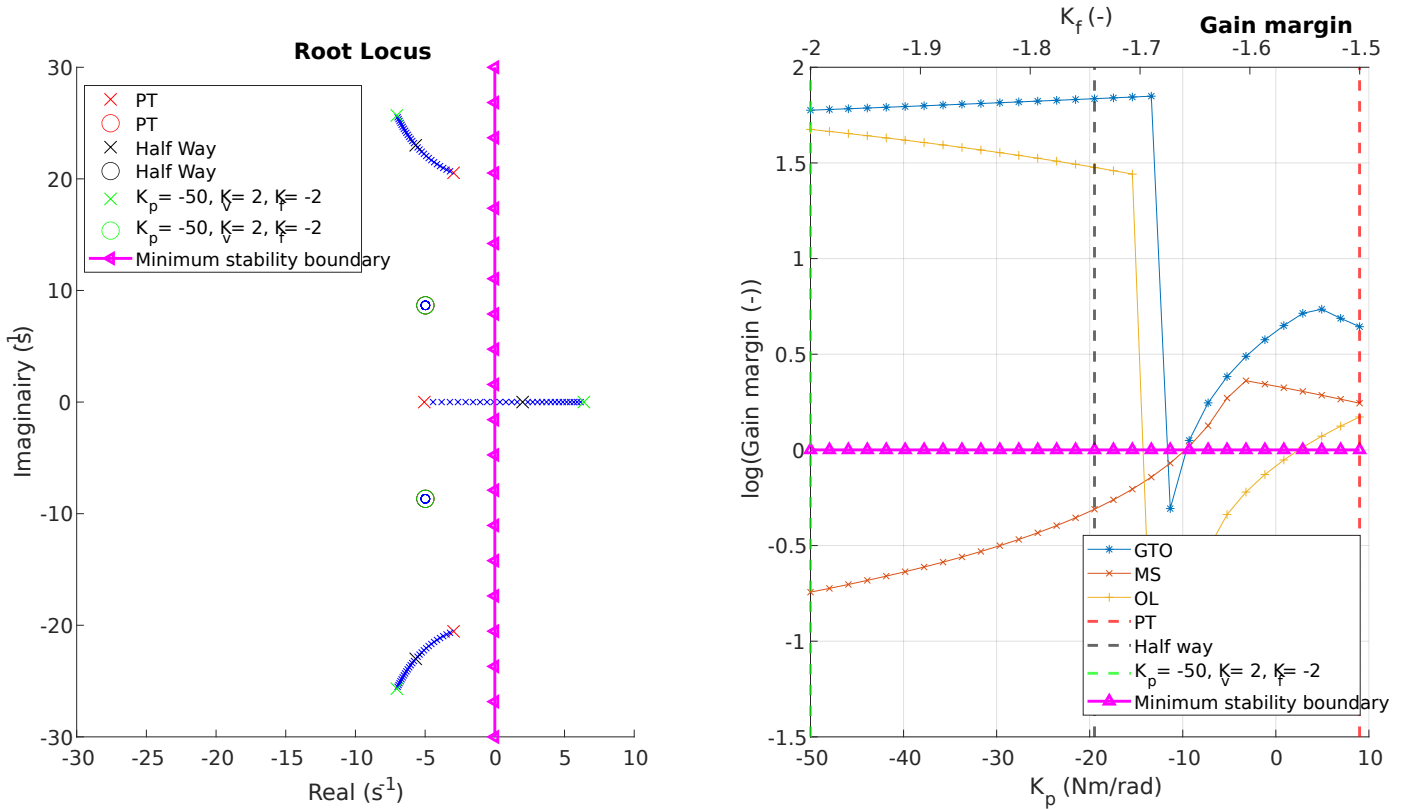


Figure E.5: Root locus of $H_{u,sup,m,mus}$ at stability boundary due to too small K_p . From PT to E

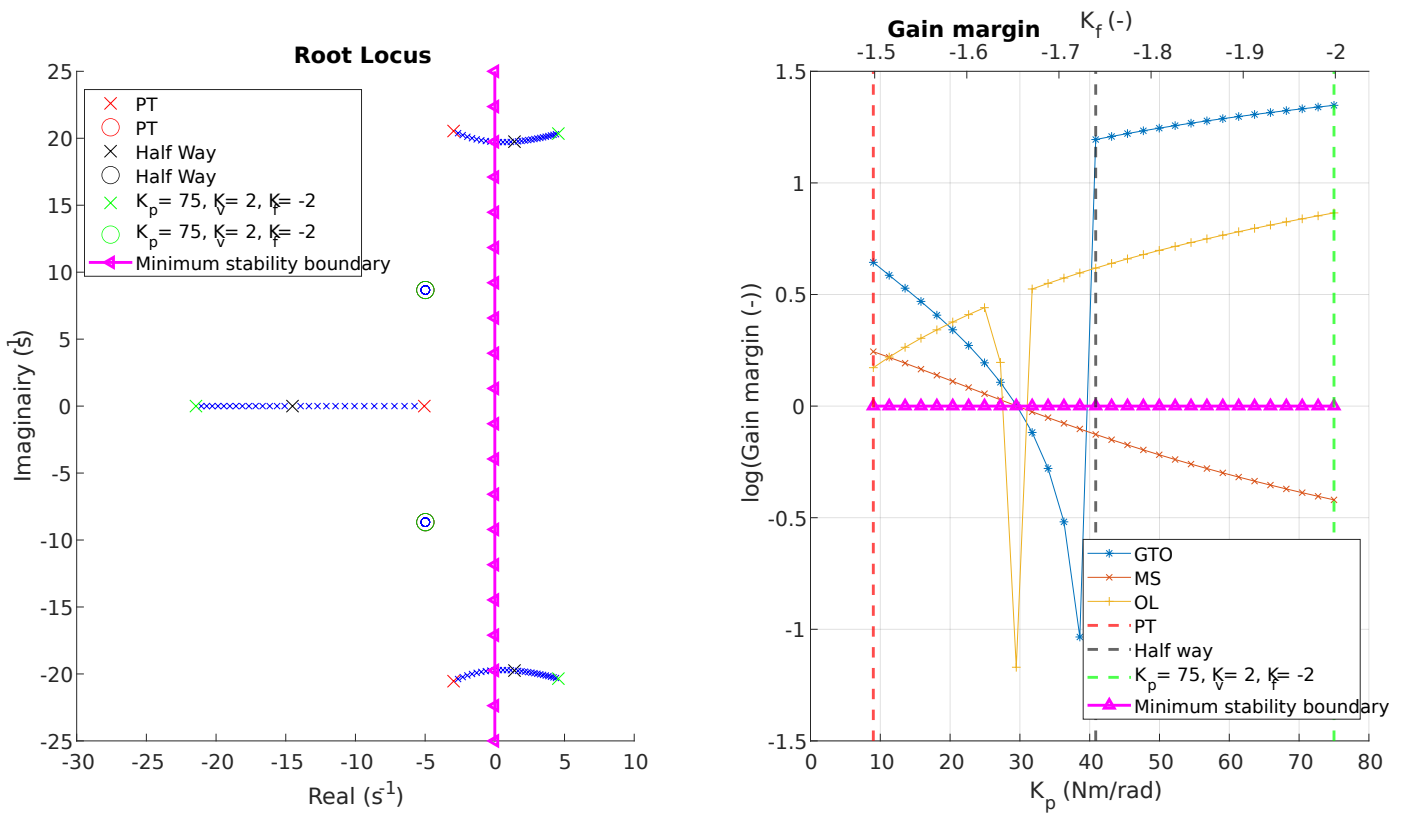


Figure E.6: Root locus of $H_{u,sup,m,mus}$ at stability boundary due to too large K_p . From PT to F

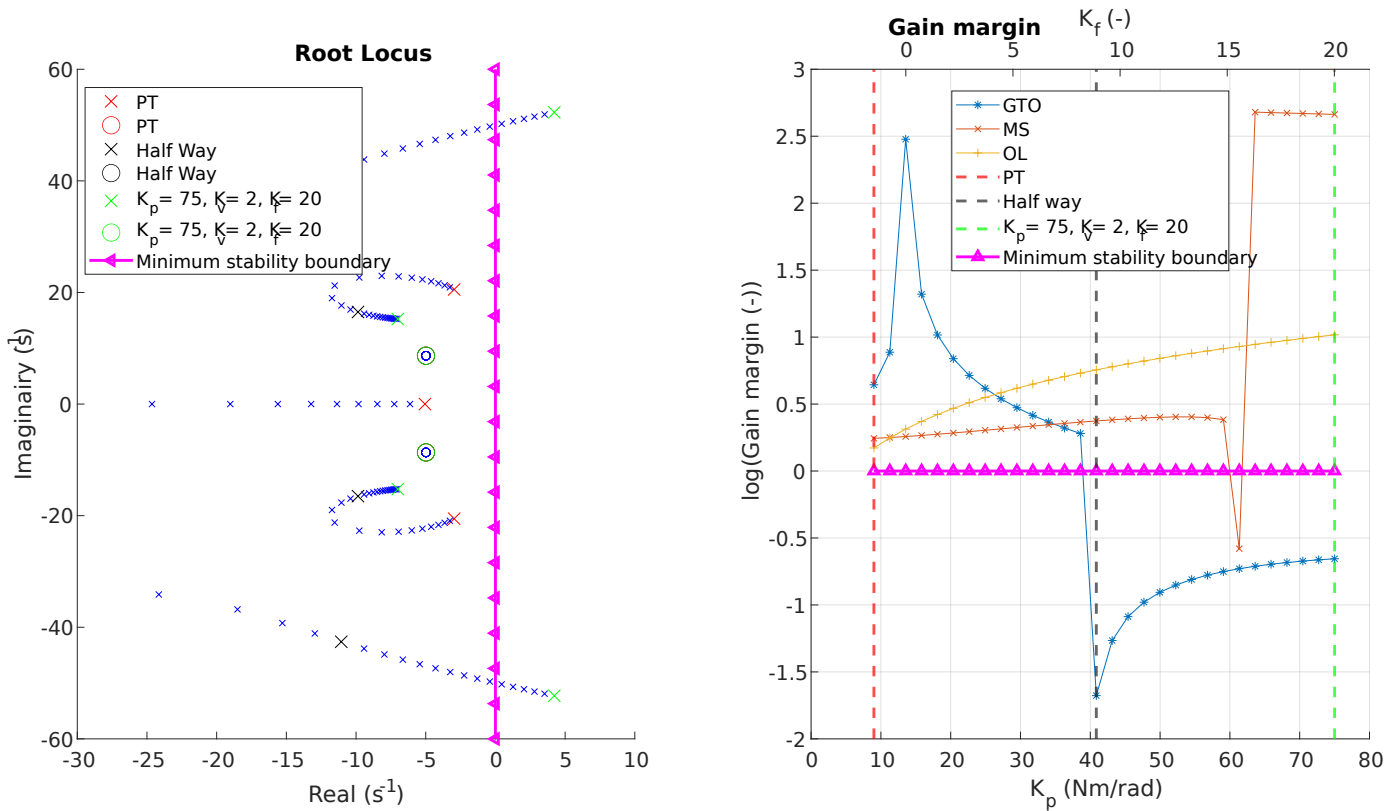


Figure E.7: Root locus of $H_{u,sup,m_{mus}}$ at stability boundary due to too large K_f . From PT to G

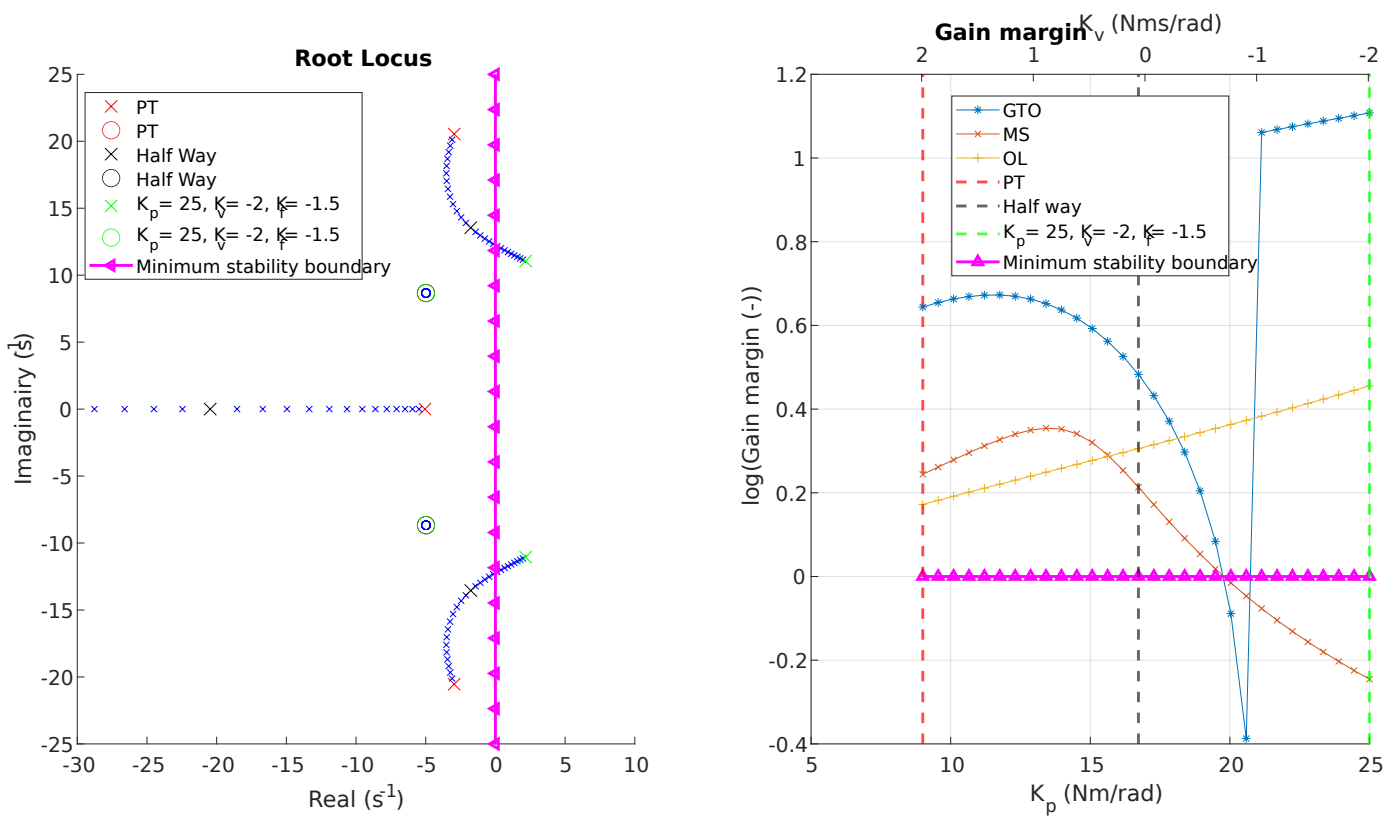


Figure E.8: Root locus of $H_{u,sup,m_{mus}}$ at stability boundary due to too small K_v . From PT to H

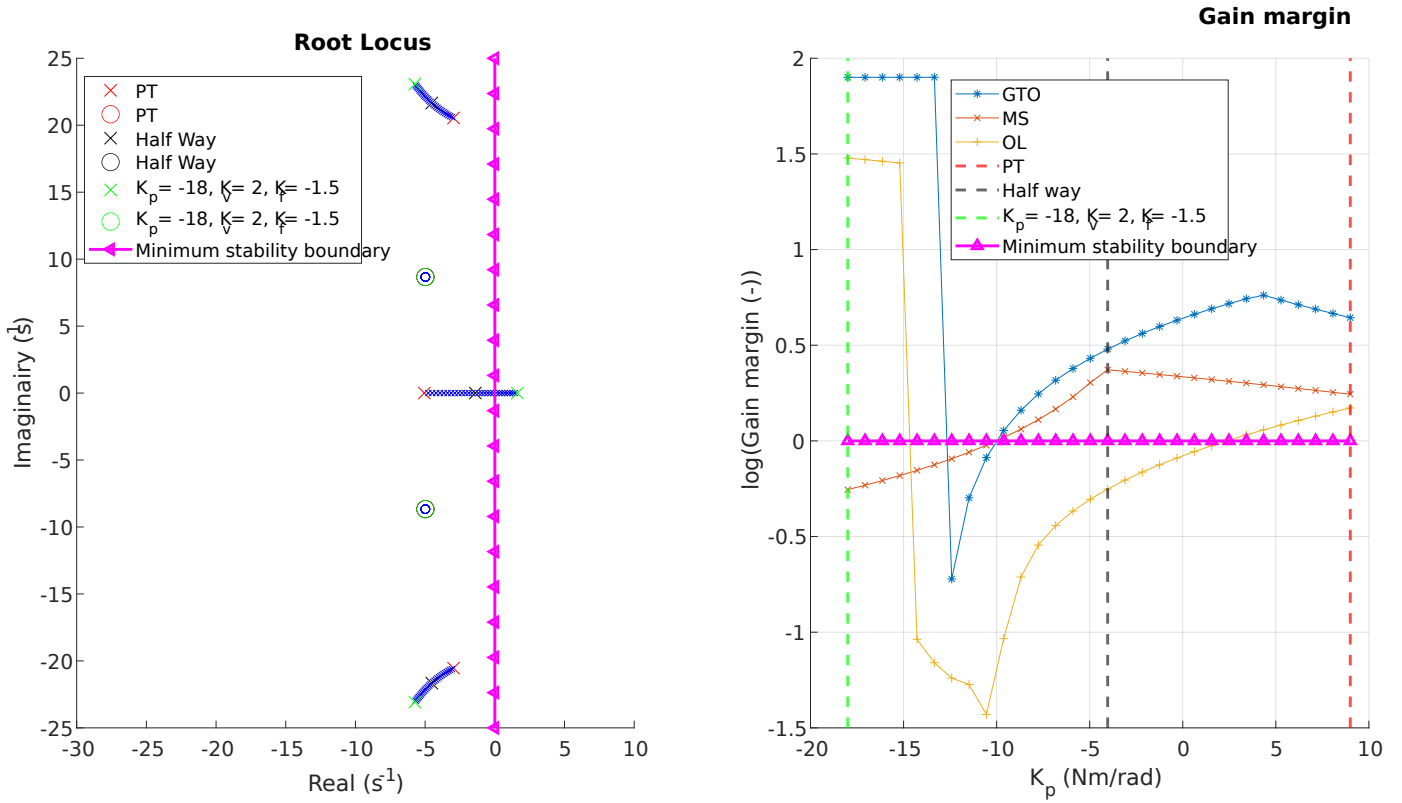


Figure E.9: Root locus of $H_{u,sup,m,mus}$ at stability boundary due to too small K_p . From PT to I

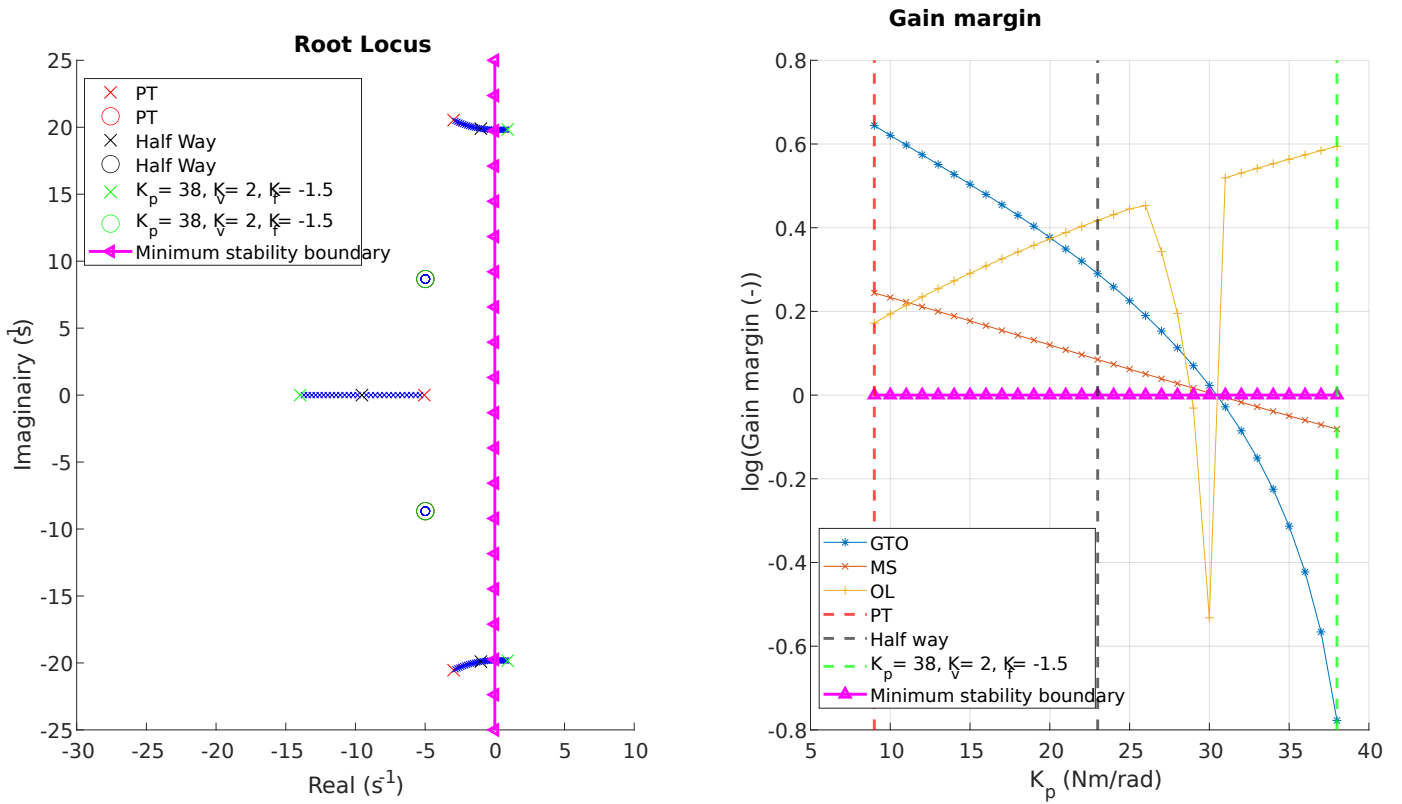


Figure E.10: Root locus of $H_{u,sup,m,mus}$ at stability boundary due to too large K_p . From PT to J

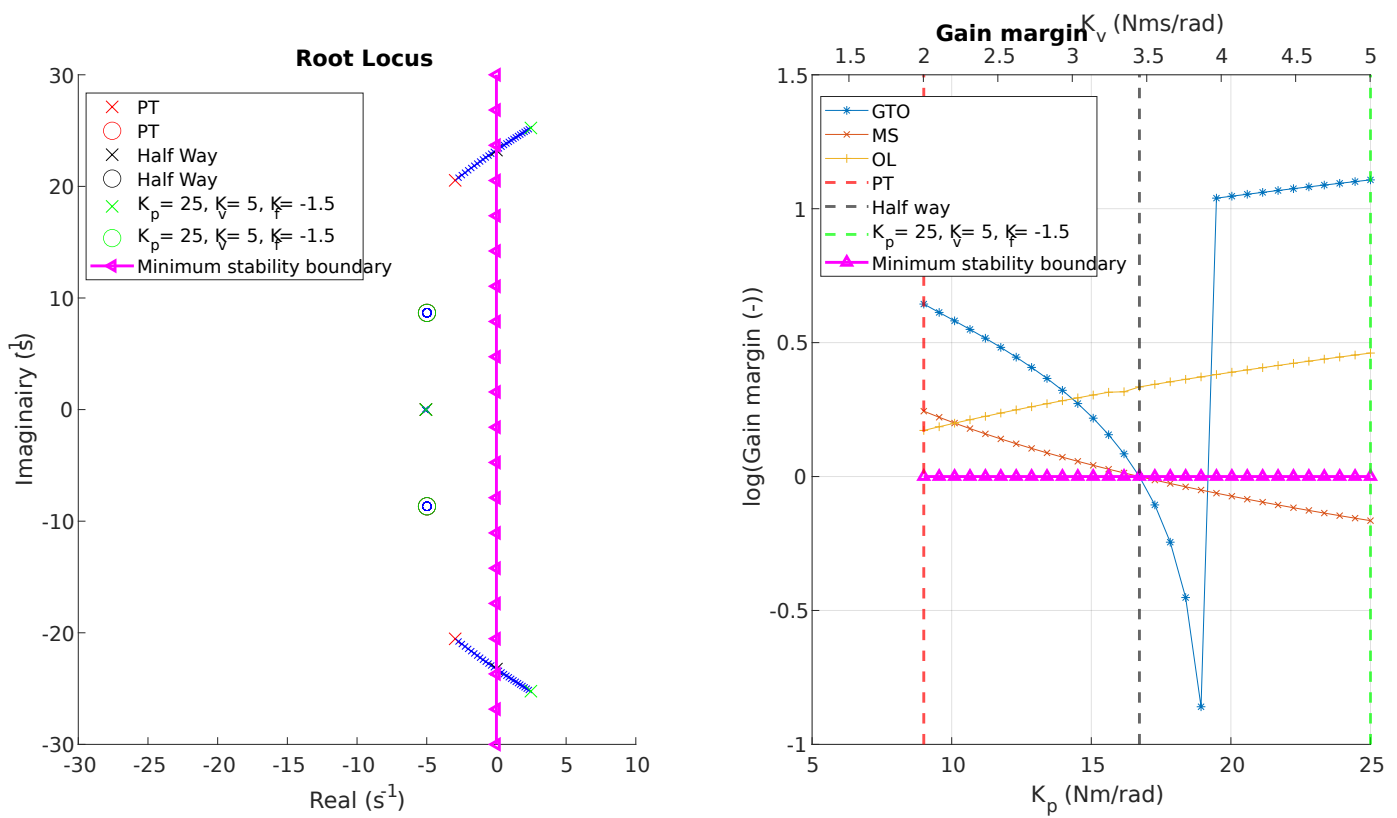
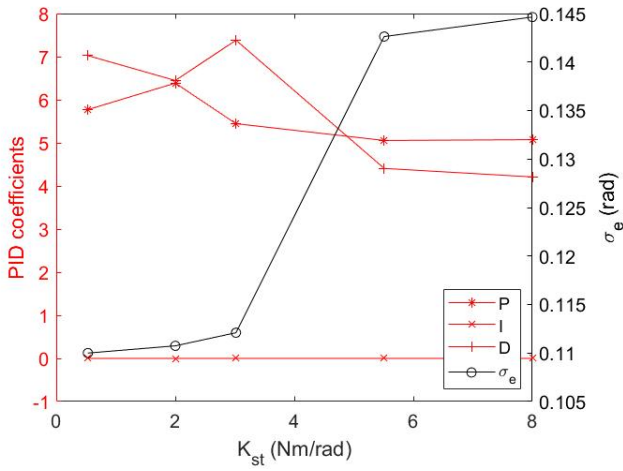


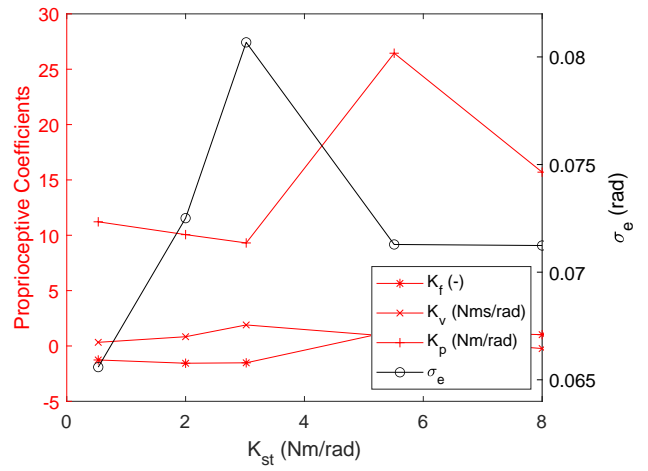
Figure E.11: Root locus of $H_{u_{sup}, m_{mus}}$ at stability boundary due to too large K_v . From PT to K

F

Tuned Pilot Model Parameters at BW1 and BW3

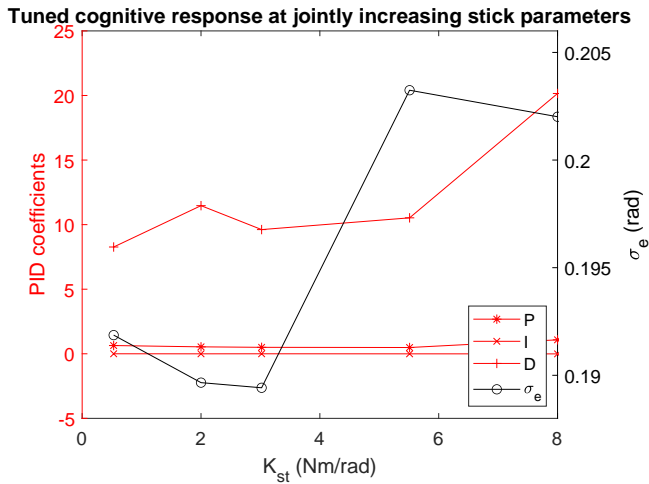


(a) Cognitive response PID parameters

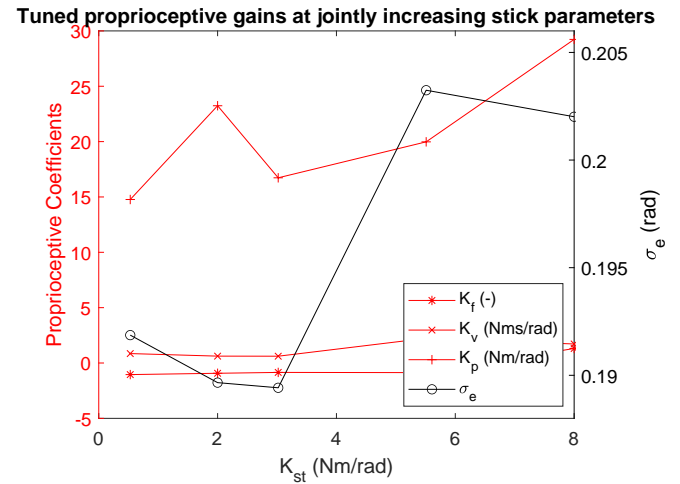


(b) Proprioceptive feedback parameters

Figure F.1: Tuned Pilot Model Parameters (P_e , I_e , D_e , K_p , K_v and K_f) with Changing Stick Dynamics at BW1 Forcing Functions



(a) Cognitive response PID parameters

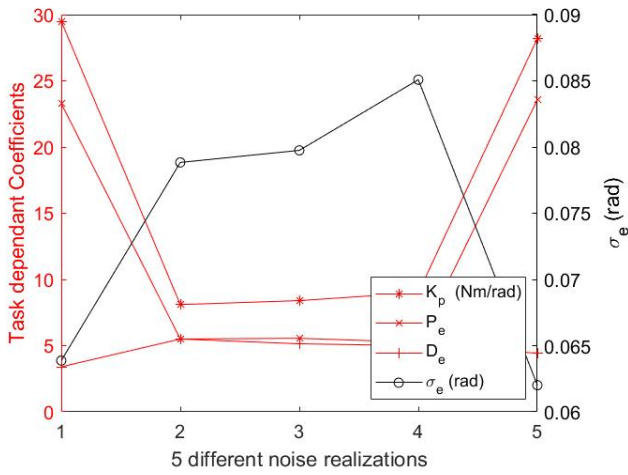


(b) Proprioceptive feedback parameters

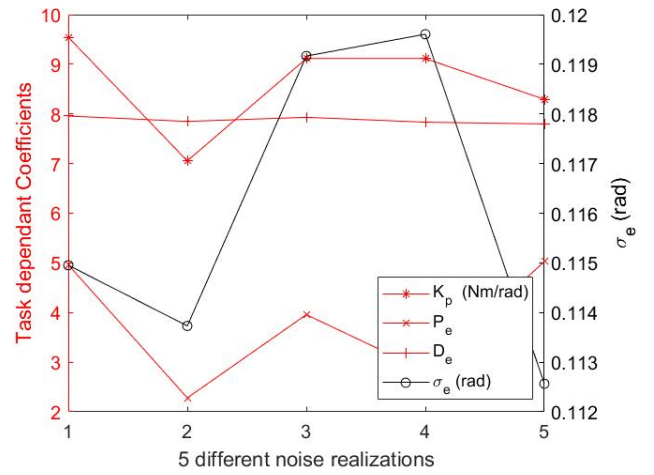
Figure F.2: Tuned pilot model parameters (P_e , I_e , D_e , K_p , K_v and K_f) with changing stick dynamics at BW3 forcing functions



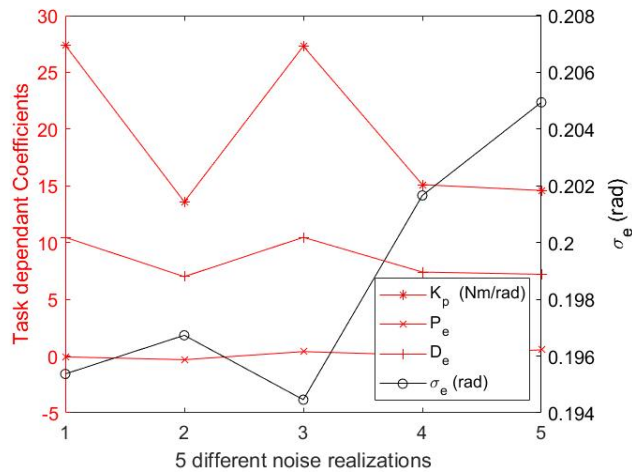
Tuning selected model parameters with limited noise realizations



(a) Tuned parameters at BW1

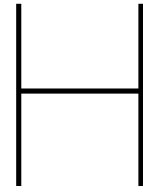


(b) Tuned parameters at BW2

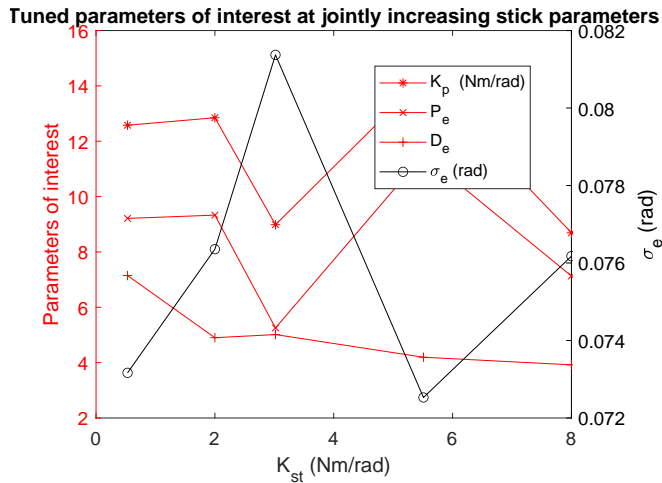


(c) Tuned parameters at BW3

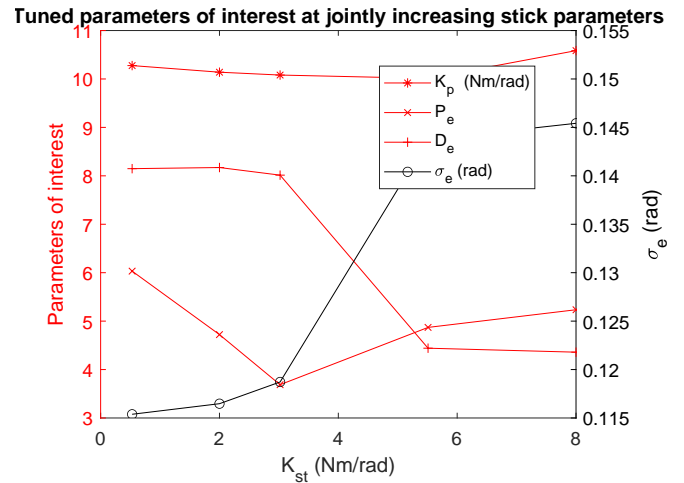
Figure G.1: Tuned selection of pilot model parameters (K_p , P_e and D_e) with only five different noise realizations shown per bandwidth condition



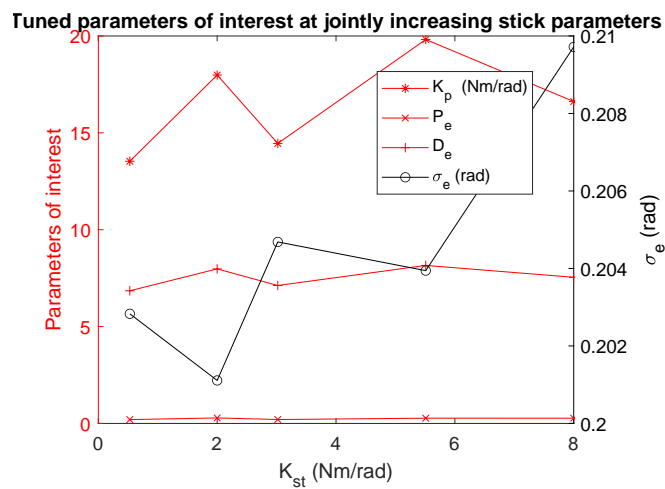
Final tuning of selected model parameters with 50 noise realizations



(a) Tuned parameters of interest (K_p , P_e and D_e) with changing stick dynamics at BW1 forcing functions



(b) Tuned parameters of interest (K_p , P_e and D_e) with changing stick dynamics at BW2 forcing functions



(c) Tuned parameters of interest (K_p , P_e and D_e) with changing stick dynamics at BW3 forcing functions

Figure H.1: Tuned parameters of interest (K_p , P_e and D_e) shown per bandwidth condition